MEGATIDAL CONTROLS ON COASTAL GROUNDWATER AND SALTWATER INTRUSION DYNAMICS ALONG AGRICULTURAL DYKELANDS

by

Nicole K. LeRoux

Submitted in partial fulfilment of the requirements
for the degree of Master of Applied Science

at

Dalhousie University
Halifax, Nova Scotia
December 2022

TABLE OF CONTENTS

LIST OF TABLES

LIST OF FIGURES

Appendix Figures

ABSTRACT

Climate change is projected to substantially increase the global mean sea level, which will likely have adverse impacts on coastal communities worldwide. Atlantic Canada is particularly vulnerable to the effects of climate change due to its low-lying elevation and high rates of past and projected sea-level rise. Nova Scotia, Canada has over 240 kilometers of dykes that protect coastal areas from seawater inundation. Much of the dyked coast is impacted by mega-tidal conditions, which can have significant impacts on saltwater intrusion and groundwater flow dynamics along the coast. While the effects of surface flooding receive the most attention, coastal aquifers in dykelands are also vulnerable to salinization from higher maximum surface water elevations arising from sea-level rise, intensifying storms, or the highest tides.

The goal of this study was to use both field methods and numerical modeling techniques to investigate saltwater intrusion dynamics in a mega-tidal dykeland setting to assess how the groundwater system responds to present forcing and to investigate how future climate change may drive further saltwater intrusion. This was accomplished by initiating a field campaign near the town of Wolfville, Nova Scotia. A climate station, wave buoy, and tidal station were deployed; shallow piezometers were drilled and instrumented; deep existing town wells were instrumented; and geophysics surveys were conducted. The field data highlight the strong connectivity between the Bay of Fundy and the adjacent aquifer given the observed pronounced tidal variations in groundwater levels and ground resistivity. These data were used to establish an environmental baseline to calibrate a present-day coupled numerical model of variable-density groundwater flow and salt transport. This model was then forced with climate scenarios including projections for sea-level rise and storm-induced dyke overtopping.

Numerical model results indicate that storm surges pose the largest threat to the aquifer and shallow agricultural soils, particularly when the dyke is removed, and overtopping occurs. SLR results also decreased the freshwater volume in the aquifer by 32% for the worst-case scenario. These results suggest that dykeland management decision frameworks should include coastal groundwater to ensure a sustainable future for drinking water and irrigation resources.

LIST OF ABBREVIATIONS AND SYMBOLS USED

A_R	Amplitude ratio [dimensionless]
b	Aquifer thickness [m]
C_o	Solute concentration in water on the surface domain [kg m^{-3}]
D	Hydraulic diffusivity [m^2 hr^{-1}]
d_o	Depth of flow [m]
$\boldsymbol{D_o}$	Hydrodynamic dispersion tensor of the surface flow domain [m^2 s^{-1}]
ET_G	Evapotranspiration from the subsurface flow system [m^3 s^{-1}]
ET_S	Evapotranspiration from the surface flow system [m^3 s^{-1}]
$h(x,t)$	Hydraulic head at a point in space and time [m]
h_f	Freshwater head in the aquifer above sea level [m]
H_o	Amplitude of the tidal signal [m]
h_o	Water surface elevation [m]
h_s	Depth to saltwater-freshwater interface below sea level [m]
I	Interception [m]
K	Hydraulic conductivity [m s^{-1}]
k_r, k_{dr}	Relative permeabilities of underlying porous and dual media [dimensionless]
K_{zz}, K_{dzz}	Vertical saturated hydraulic conductivities of porous and dual media [m s^{-1}]
L_{exch}	Coupling length [m]
M	Slope of the line representing the relation [dimensionless]
ϕ_o	Surface flow domain porosity [dimensionless]
P	Precipitation [m]
par	Parent species for the case of a decay chain
PET	Potential evapotranspiration [mm day^{-1}]
$\boldsymbol{q}$	Fluid flux vector [m s^{-1}]
Q	Volumetric fluid flux per unit volume [m^3 m^{-3} s^{-1}]
Q_{G1}, Q_{G2}	Subsurface water inflow and outflow [m^3 s^{-1}]

Q_{GS}	Surface/subsurface water interactive flow [m^3 s^{-1}]
Q_o	Volumetric flow rate per unit area representing external sources and sinks [m s^{-1}]
Q_{s1}, Q_{s2}	Surface water inflow and outflow [m^3 s^{-1}]
R_n	Net radiation [cal cm^{-2} day^{-1}]
R_o	Resistivity of material when all pores are filled with saltwater [Ω m]
R_o	Retardation factor [dimensionless]
R_w	Resistivity of saltwater [Ω m]
S_{fx}, S_{fy}	Friction slopes in the x- and y-directions [dimensionless]
ΔS_G	Subsurface water storage over time step Δt [s^{-1}]
SGD	Submarine groundwater discharge
SLR	Sea-level rise
S_{ox}, S_{oy}	Bed slopes in the x- and y-directions [m s^{-1}]
S_s	Specific storage [m^{-1}]
ΔS_s	Surface water storage over time step Δt [s^{-1}]
S_w	Degree of water saturation [dimensionless]
SWI	Saltwater intrusion
S_y	Specific yield [dimensionless]
t	Time [s]
w_d	Dual continuum volumetric fraction of total porosity [dimensionless]
w_m	Porous media volume fraction of total porosity [dimensionless]
x	Distance between the well and ocean [m]
z_o	Bed (land surface) elevation [m]
α	Albedo or canopy reflection coefficient [dimensionless]
γ	Latent heat of vaporization [MJ kg^{-1}]
Δ	Slope of the saturation vapor pressure curve at air temperature T [kPa °C^{-1}]
Θ	Porosity fraction of material [dimensionless]
θ_s	Saturated water content (porosity) [dimensionless]
λ	Solute first-order decay constant [m^{-1}]

$\bar{v}_{xo}, \bar{v}_{yo}$	Vertically averaged flow velocities in the x- and y-directions [m s^{-1}]
δ	Density ratio [dimensionless]
ρ_f	Freshwater fluid density [kg m^{-3}]
ρ_s	Saltwater fluid density [kg m^{-3}]
ω	Angular wave frequency [rad hr^{-1}]
τ	Tidal period [hr]
Q_S^W	Overland water withdrawal [m^3 s^{-1}]
Q_G^W	Subsurface water withdrawal [m^3 s^{-1}]
Γ_{ex}	Volumetric fluid exchange rate between domains [m^3 m^{-3} s^{-1}]
Γ_o	Dual continuum volumetric fluid exchange rate between domains [m^3 m^{-3} s^{-1}]

ACKNOWLEDGMENTS

CHAPTER 1: INTRODUCTION

1.1 Coastal forcing and coastal groundwater resources

Coastal regions are dynamic transition zones between land and sea. In 2012, it was estimated that approximately 50% of the global population occupies land within 150 km of the coastline (Lemmen et al., 2016). Along with the aesthetic appeal and economic opportunities that attract humans to coastal zones, there are many co-existing physical processes and phenomena taking place, including waves, tides, coastal storms, and anthropogenic forcing (Ramkumar et al., 2019). The coastal zone is considered the battleground for converging forces, including terrestrial, atmospheric, and anthropogenic stresses (Beatley et al., 2002), and the coastal zone is constantly adapting to reach an equilibrium between these competing forces (Jiao & Post, 2019).

Canada has the world's longest coastline with more than 240,000 km and approximately 7 million people living along these dynamic zones (Lemmen et al., 2016). As such, the effects of coastal threats will continue to be greatly felt by Canadians. As one recent example, Hurricane Fiona devastated Atlantic Canada in September 2022 with sustained winds of 150 kph and the lowest recorded pressure (931 mbar) of any hurricane making landfall in Canada (Lopez-Martinez, 2022). In the longer term, atmospheric and marine climate change, and anthropogenic pressures such as coastal development are all important for a country with extensive coastlines (Manson et al., 2019). Due to its past glacial history and associated isostatic rebound, the east coast of Canada has high rates of recent and projected sea-level rise (SLR), and this region is also densely populated with coastal communities

(Figure 1). Canadian coasts are also expected to be subjected to intensifying wave action due to sea-ice melt (Lemmen et al., 2016).

Many previous studies worldwide have assessed the impacts of climate change on coastal communities, and these have generally emphasized the importance of proper coastline management techniques to ensure accessibility to resources (*e.g.*, groundwater, agricultural crops) and protection of infrastructure for future decades (Boateng, 2012; Michael et al., 2017). Freshwater management is critical to ensure sustainable resource usage under current and future climate projections and increasing coastal populations (Yang et al., 2015).

Groundwater is commonly used along coastal/rural communities for agriculture, domestic, and industrial purposes due to the limited spatial distribution and quality of surface water sources (Sawyer et al., 2016). However, coastal groundwater resources are highly vulnerable to climate change due to the looming threats from SLR and increased demand from population growth (Ketabchi et al., 2016; Manson et al., 2019; Yang et al., 2015). Many coastlines are currently undergoing coastal groundwater squeeze, a term referring to the combined top-down (anthropogenic contamination) and bottom-up (salinization) threats posed to coastal groundwater resources as a result of poor coastal zone management in the context of climate change (Llopis-albert & Pulido-velazquez, 2014; Michael et al., 2017). In addition to being vulnerable to atmospheric climate change, coastal areas are lower in elevation and more proximal to the changing marine environment, and thus even more susceptible to climate change impacts compared to inland environments. Dense human population distributions along the coast also impose further challenges to resource management, such as changing groundwater flow patterns and degrading freshwater quality

and quantity through overuse and pollution (Michael et al., 2017; Yang et al., 2015). There is an urgent need to stop the over-exploitation of these resources that have resulted from socio-economic pressures in coastal zones in conjunction with climate change (IPCC, 2019).
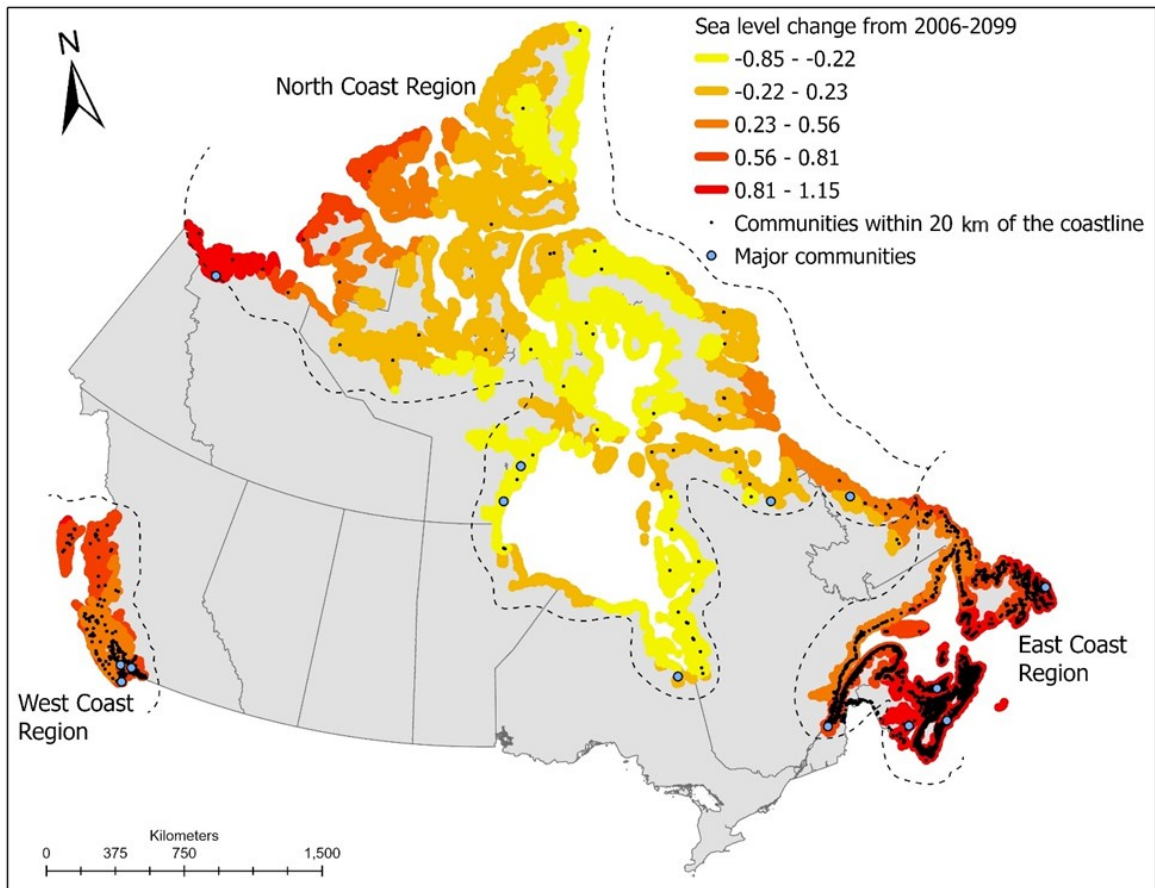
Figure 1. Sea-level rise (SLR) projections for Canada based on changes in the volume of water and vertical motion of land. Data are replotted from tabulated data from Manson et al. (2019) and are based on a high-emission representative concentration pathway (RCP) 8.5 with a refined model of vertical land motion generated by the Canadian Geodetic Survey.

1.2 Sea-level rise and impacts to groundwater levels

Sea-level rise (SLR) is a result of both land subsidence and oceanic thermal expansion due to climate change. The Intergovernmental Panel on Climate Change (IPCC) multi-model global climate projections indicate that the global mean sea level may rise between 0.26 and 0.82 m by the year 2100 (IPCC, 2019). The response of aquifers to sea-level rise may increase the hazards presented to these water resources and dependent ecosystems and communities, and result in substantial displacement of coastal inhabitants over the next century (Befus et al., 2020). As outlined by Ketabchi et al. (2016), many studies have considered sea-level rise impacts on saltwater intrusion studies using analytical techniques (*e.g.*, Werner & Simmons, 2009). While analytical solution approaches work well for capturing the essence of the system, they inevitably invoke many unrealistic simplifications, and therefore, numerical model simulations are now more commonly being employed (Chang et al., 2011; Feseker, 2007; Watson et al., 2010). Most numerical modeling studies focused on coastal groundwater over the last decade have pointed to the potential for sea-level rise to induce saltwater intrusion (Bobba, 2002; Greenberg et al., 2012).

The rate of sea-level rise along the Atlantic coast of Canada is expected to greatly exceed the global average (Lemmen et al., 2016; Manson et al., 2019). Since the Wisconsin glaciation, the height of the relative sea level to the land has been steadily rising by almost 40 centimeters every century as a result of both rising sea level and land subsidence (Greenberg et al., 2012; Percy, 1996). As such, sea-level rise is a primary driver for coastal change. In Nova Scotia, approximately 70% of the population occupies land within 20 km of the coastline, with many of these communities relying on groundwater for drinking water

supply and irrigation (Lemmen et al., 2016). Changes to mean sea levels, storm intensities, and/or frequencies that are projected by climate models will mean more frequent and more devastating flooding for these coastal communities (Forbes et al., 2009), as well as the less-studied impacts to coastal aquifers.

Low-lying coastal areas are vulnerable to water table rise because of their connectivity to the ocean. Rising seas force the inland water table to rise simultaneously, eventually leading to saturated and inundated land if adaptation techniques are not implemented (Bjerklie et al., 2012; Schieder et al., 2018). Many agricultural fields are located within kilometers of the coastline, and thus are highly vulnerable to a loss of arable conditions and poor drainage (Badaruddin et al., 2015; Bayabil et al., 2020; Gedan & Fernández-Pascual, 2019; Guimond & Michael, 2020). Water table rise also threatens subsurface infrastructure, including the performance of onsite wastewater treatment systems (Threndyle et al., 2022).

1.3 Coastal groundwater controls and dynamics

Groundwater dynamics in coastal regions are largely determined by geologic properties and atmospheric and oceanic forcing (Hiscock & Bense, 2014; Jiao & Post, 2019). Thus, characterizing coastal aquifers is essential for the protection and sustainable development of groundwater resources (Freeze & Cherry, 1979; Rivard et al., 2012). Groundwater density plays a key role along the coastline as salt concentration and fluid density vary across the mixing zone between fresh and saline water in coastal aquifers due to mechanical dispersion and molecular diffusion, and marine forcing (Werner et al., 2013). There are methods that consider this mixing zone as being either a sharp interface or a gradual transition zone. The sharp-interface method is usually combined with the Ghyben-Herzberg

principle (Figure 2), which is a classic approach for estimating the depth to a sharp saltwater-freshwater interface given the groundwater table elevation (Ghyben, 1988; Herzberg, 1901). This approach is widely used but limited by the following assumptions: (1) simple hydrostatic conditions exist, (2) the aquifer is homogeneous, and (3) the coastal aquifer is unconfined (Hiscock & Bense, 2014). This method is fundamentally based on understanding that for a sharp freshwater-saltwater interface, the porewater pressures at the freshwater and saltwater sides of the interface are equal (Freeze & Cherry, 1979). This equality can be expressed and rearranged to give the following:

$$h_s = \frac{\rho_f}{\rho_s - \rho_f} h_f \quad \text{or} \quad h_s = \delta h_f \qquad [1]$$

where h_s is the depth to the saltwater-freshwater interface below sea level (m), ρ_f is the freshwater density (kg m^{-3}), ρ_s is the saltwater density (kg m^{-3}), and h_f is the freshwater head in the aquifer above sea level (m) (Figure 2). The dimensionless density ratio δ can be found by comparing the two forms in Eq. [1].

Equation [1] suggests that the density difference and head of freshwater (*e.g.*, water table elevation) control the depth to saltwater. If we assume common fluid densities of $\rho_f = 1000$ kg m^{-3} and $\rho_s = 1025$ kg m^{-3}, Eq. [1] suggests that the depth below sea level to the saltwater interface is approximately 40 times the depth of the freshwater head above sea level.
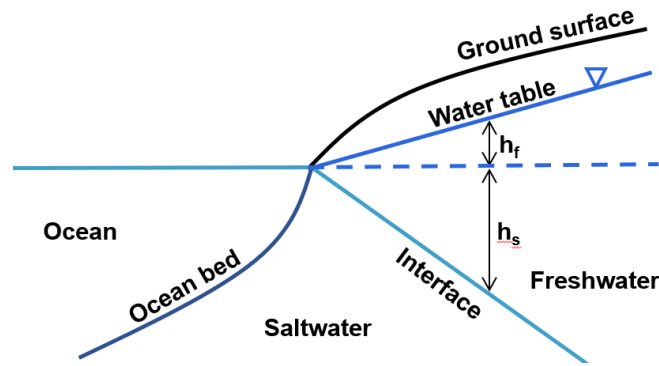
Figure 2. Ghyben-Herzberg relationship (modified from Hiscock & Bense, 2014) showing the depth to the freshwater-saltwater interface (see Eq. 1). Not to scale.

The sharp-interface methods are less realistic than approaches that accommodate a transition zone, yet they are useful for providing insight into the physics of these systems (Llopis-albert & Pulido-velazquez, 2014). The transition zone methods are based on the realization that the saltwater-freshwater mixing zone is controlled by the dispersive characteristics of the geologic strata (Freeze & Cherry, 1979). Henry (1960) was the first to develop an analytical solution for transition zone methods, but there are now various other solutions that include considerations of dispersion (e.g., Cooper, 1964). Such 'transition zone' analytical solutions are often limiting as they invoke many unrealistic assumptions such as homogeneous properties and steady-state conditions, and thus coupled numerical models of variable-density groundwater flow and solute (salt) transport are more commonly employed to study transition zone dynamics.

Submarine groundwater discharge (SGD) refers to groundwater (*e.g.*, fresh or recirculated seawater) that flows from the seabed into the ocean (LeRoux et al., 2021; Threndyle et al., 2022). In coastal areas, recharge and associated higher hydraulic heads in aquifers cause groundwater to generally flow from inland areas towards the sea (Jiao & Post, 2019). Studies have shown that in many locations, SGD from the aquifer to the ocean represents

a significant water flux that can provide a vector for terrestrial contaminants and constituents (Gonneea et al., 2013; Robinson et al., 2018). Figure 3 shows the complexity of coastal zone processes, with a particular focus on coastal groundwater dynamics.
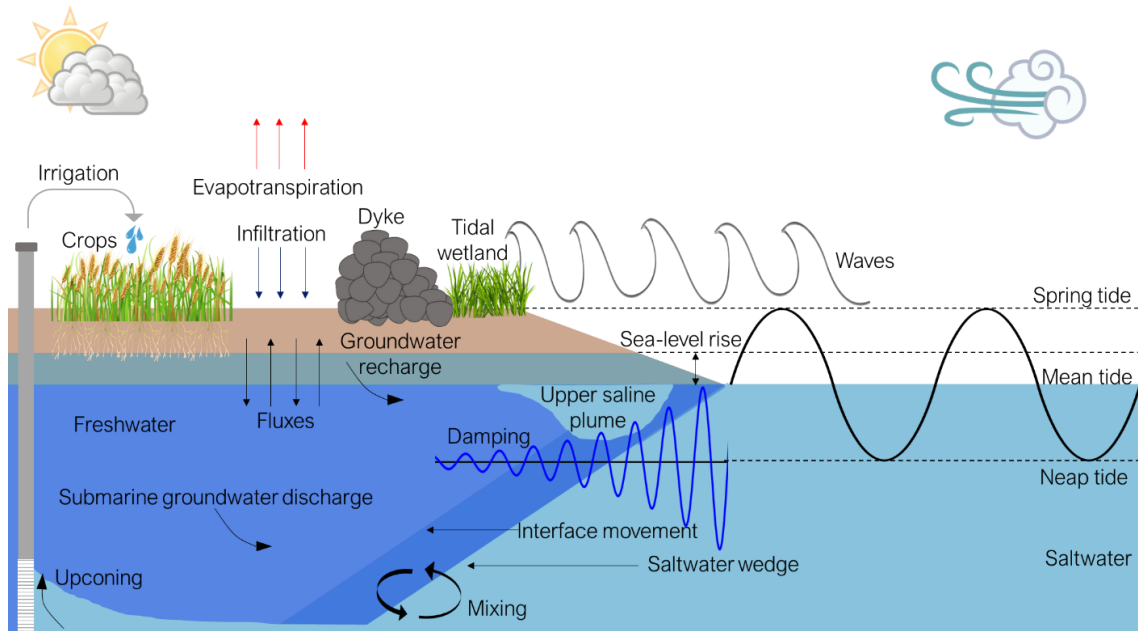
Figure 3. Coastal groundwater processes and conditions influenced by anthropogenic, atmospheric, terrestrial, and marine forces.

Groundwater dynamics in coastal zones are briefly described here at a high level, with more detailed explanations in later sections within this chapter. Starting from the marine side (right) of Figure 3, the mean ocean water level fluctuates due to different tidal constituents including diurnal, semi-diurnal, and spring-neap constituents (Kamphuis, 2010). This pressure oscillation propagates into the aquifer, but the periodic signal gets damped and lagged with distance landward (*e.g.*, Jacob, 1950; Rotzoll & Fletcher, 2013) (described further in section 1.5.1). The upper saline plume (Figure 3) is generated due to the fluctuation in sea level induced by tides and wave runup (Fang et al., 2021). The tides also smooth out or 'smear' the subsurface interface between fresh and saline groundwater

(Figure 3). In addition to this regular tidal forcing, there are also irregular wave and surge dynamics that can occur during any stage of the tide but are of most concern during spring-high tides (Figure 3), as this superposition of forcing can temporarily increase the water level far above the mean water level and overtop or damage coastal barriers (McLaughlin et al., 2022). Sea-level rise will also exacerbate the potential for flooding and force the saltwater-freshwater interface to migrate landward and upward (Ketabchi et al., 2016).

On the terrestrial side, coastal wells may begin to draw up saltwater due to over pumping, a process known as upconing (Reilly & Goodman, 1987; Schmork & Mercado, 1969; Werner et al., 2013). Also, reductions in groundwater recharge (Kurylyk & MacQuarrie, 2013) due to changes in atmospheric climate conditions or land cover will lower the water table and draw saltwater landward (Green & MacQuarrie, 2014). Around the location of the saltwater-freshwater interface or transition zone (Figure 3), there is constant mixing driven by marine forcing and the density differences in the saline and fresh water, and this density difference also maintains the salt wedge (Figure 3) (Abd-Elhamid & Javadi, 2011; Werner et al., 2012). Additionally, water more efficiently enters aquifers during high tide than it can exit during low tide, thus creating tidal overheight, a condition that results in the mean groundwater elevation at the coast being elevated compared to mean sea level (Nielsen, 1990).

1.4 Saltwater intrusion

In the context of hydrogeology, saltwater intrusion refers to the landward migration of saline water into formerly freshwater zones (Hiscock & Bense, 2014; Post & Houben, 2017;

Reilly & Goodman, 1987; Werner et al., 2013; Werner & Simmons, 2009), which poses significant threats to coastal ecosystem services (Figure 4). Saltwater intrusion can occur on time scales ranging from minutes to millennia given the range of processes that can trigger it (Werner et al., 2013). In general, groundwater recharge, pumping rates, and sea-level fluctuations mediate the location of the freshwater-saltwater interface, and thus interface movement (or saltwater intrusion) can be strongly influenced by anthropogenic activity and climate changes manifested in either the ocean or the atmosphere (Heiss & Michael, 2014). Other factors that influence saltwater intrusion include dispersive mixing, tidal effects, density effects, paleo-hydrogeological conditions (*e.g.*, past sea levels), and geological characteristics (Werner et al., 2013); thus, the causes of saltwater intrusion can be both natural and anthropogenic (Jiao & Post, 2019). The Ghyben-Herzberg equation [Eq. 1] highlights the influence of sea-level rise if the groundwater table elevation remains fixed, such as would occur in a scenario in which the water table were already at the land surface. In this scenario, the sea-level rise results in a 40 times amplification in the rise of the interface depth, making the interface a filtered but amplified reflection of the water table topography (Pavlovskii et al., 2022).

Technically, the presence of a *stable* saltwater wedge (Figure 3) is not saltwater intrusion, since such a situation is natural and there is no gradual or episodic salinization of the freshwater zone. However, saltwater intrusion occurs when the transition zone between the fresh and saltwater moves landward and/or upward (Jiao & Post, 2019) (Figure 4a), or when flooded seawater at the surface infiltrates downward into the aquifer (Cantelon et al., 2022) (Figure 4b). When salinization occurs by active flow from the ocean into the aquifer, it is known as 'active saltwater intrusion' (Figure 4). In contrast, 'passive saltwater intrusion'

occurs when the direction of groundwater flow is still seaward, but the interface is moving landwards, such as might occur following a gradual lowering of the water table due to reducing recharge. Active saltwater intrusion is often triggered by over pumping (Figure 4a).
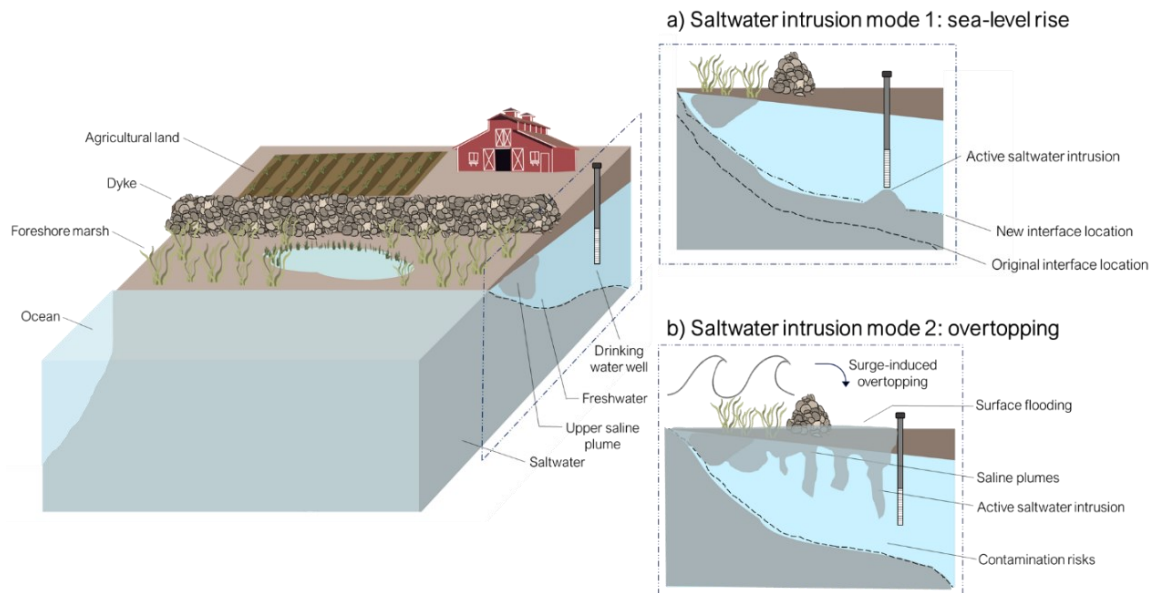
Figure 4. Saltwater intrusion via a) sea-level rise and b) surge-induced overtopping.

1.4.1 Saltwater intrusion from coastal flooding

During extreme storm surges, higher water levels can threaten coastal defence systems (*e.g.*, dyke in Figure 4 and 5) (Elsayed et al., 2018; Stockdon et al., 2006). Overtopping due to storm surges can result in breaching and erosion of these barriers from coastal flooding and wave action (Elsayed & Oumeraci, 2018a). Flooded seawater can inundate and infiltrate a fresh groundwater system, leading to potential drinking water contamination risks (Figure 4b). When this happens, salt fingers (Figure 4b) can develop due to density differences between the infiltrating seawater and underlying freshwater, and these promote downward transport and mixing of intruded seawater (Post & Houben, 2017). An aquifer

system that can quickly return to its original state (post-perturbation) is less problematic than a system that requires a longer time to 'flush' out the saltwater (Cantelon et al., 2022). The response time is determined by the nature of the seawater flooding, precipitation rates, and the aquifer's hydraulic conductivity and storage properties (Hiscock & Bense, 2014; Post & Houben, 2017). In general, studies have shown that the most important long-term effect of coastal floods is often saltwater intrusion into coastal aquifers induced by the vertical infiltration of saltwater (e.g., Elsayed & Oumeraci, 2018a).

1.4.2 Agricultural impacts of saltwater intrusion

Saltwater intrusion can have devastating impacts on agriculture productivity and sustainability. Saline water changes the soil chemistry, thereby imposing negative consequences for crops or natural vegetation that cannot withstand high salt loading (Briggs et al., 2021; Butcher et al., 2018; Fagherazzi et al., 2019; Guimond & Michael, 2020). Also, temporary flooding or chronic water table rise due to sea-level rise can elevate the soil saturation above desired levels for crops. In some coastal settings, saltwater intrusion has led to field abandonment (Gedan & Fernández-Pascual, 2019) as the crops of interest can no longer grow due to the species' intolerance of salinity or saturation (Figure 5). Recent studies have shown that coastal agricultural croplands account for the largest proportion of locations susceptible to saline inundation due to surge disasters (Kang et al., 2016).

1.5 Tidal dynamics

Tides shape much of the world's coastline and are one of the most predictable scientific phenomena (Morrison & Owen, 1966). The gravitational forces that create tidal oscillations are derived from gravitational forces between the earth, sun, and moon, which give rise to different tidal constituents geographically (Jiao & Post, 2019). Tidal constituents create diurnal (*i.e.*, one high and one low tide per day), semi-diurnal (*i.e.*, ~ two high and two low tides per day), and/or mixed (*i.e.*, when the heights of successive semi-diurnal high or low tides are different during a solar day) tidal conditions that are superimposed on spring-neap signals (from the phases of the moon) and lower frequency constituents (Kamphuis, 2010). The difference in the high- and low-tide values is known as the tidal range, and globally tide ranges vary from micro- (*i.e.*, less than 3 m) to mega-tidal (*i.e.*, greater than 8 m) conditions. Tides are more predictable perturbations than episodic events like storm surges; however, their magnitudes vary substantially from site to site and even with time depending on the amplitude of the spring-neap constituent (Kamphuis, 2010; Werner et al., 2013). These large oceanic forces play important roles in the coastal zone, particularly when considering groundwater flow dynamics.

1.5.1 Tidal effects on groundwater flow

Groundwater flow in coastal environments is highly complex as tides are constantly altering the magnitude and potentially the direction of the hydraulic gradient and consequent groundwater flow. Many studies have considered tidal groundwater dynamics (Cartwright et al., 2004; Robinson & Li, 2004; Vandenbohede & Lebbe, 2007) and the influence on coastal groundwater flow and water quality in unconfined aquifers (Kuan et

al., 2012; Levanon et al., 2017; Robinson et al., 2018). Others have pointed to the importance of tidal overheight using analytical solutions (Cartwright et al., 2004; Nielsen, 1990). Another major focus in the literature has been using analytical solutions to investigate how tides influence groundwater level fluctuations (Li & Jiao, 2001; Nielsen, 1990; Teo et al., 2003) and thus how tidal dynamics can be used to infer aquifer properties. Regardless of the application, past coastal groundwater studies have typically only considered smaller tidal ranges (*i.e.*, micro- to macro-tidal) (*e.g.*, Heiss & Michael, 2014), with a few rare considerations of mega-tidal conditions, usually with a sole focus on beach aquifer dynamics (e.g., Stark & Hay, 2014). This is likely in part at least due to the limited number of locations worldwide that experience mega-tidal conditions.

Studies have shown that the transition zone between freshwater and saltwater is wider when tidal influences are considered (Ataie-Ashtiani et al., 1999; Inouchi et al., 1990; Pool et al., 2014). Water exchange across the interface is significantly affected by tides and mixing of tide-induced recycled water with fresh groundwater (Robinson & Li, 2004). For coastal aquifers, varying physical forcing conditions (*i.e.*, tides) drive changes in the upper saline plume of the saltwater-freshwater interface (Figure 3), forcing the conditions to change from stable to unstable (Fang et al., 2021). Also, the tidally dynamic location where saltwater and freshwater meet in the subsurface can influence the near-shore and large-scale submarine groundwater discharge patterns and impact contaminant loading levels across the aquifer-ocean interface (Chang et al., 2011). In general, tidal dynamics can have extensive impacts on coastal freshwater resources, and thus there is a great need to assess the vulnerability of coastal areas to these tidal dynamics (Huizer et al., 2017; Neubauer, 2013; Park & Aral, 2008).

1.5.2 Tidal effects on saltwater intrusion

Despite the strong evidence that tides exert a dominant control on coastal groundwater levels and dynamics, there has not been substantial work done that incorporates tidal fluctuations in conjunction with saltwater intrusion dynamics (*e.g.*, flushing rates). Ataie-Ashtiani et al. (1999) investigated the effects of micro-tidal influences on saltwater intrusion in unconfined coastal aquifers. They found that the seaward freshwater flux in the aquifer had a considerable influence on both the shape and the location of the freshwater-saltwater interface, and that less freshwater discharging to the sea not only caused the seawater to intrude further inland but also made the interface more dispersed as a result of the tidal boundary (Ataie-Ashtiani et al., 1999). Additionally, Werner & Lockington (2006) showed that the inclusion of tides in active saltwater intrusion simulations produced highly modified predictions of water table salinization but had only minor impacts on the predictions of the saltwater intrusion extent. Other studies have shown through analytical techniques that the saltwater-freshwater interface moves seaward with the inclusion of tidal influences, and the toe of the interface remains stationary (*e.g.*, Zhang, 2000). Larger macro-tidal amplitudes have been shown to increase the groundwater salinity (and thus transition zone) near the base of the aquifer, thereby reducing the amount of freshwater present (Vandenbohede & Lebbe, 2007). Others have shown that the salt distribution and wedge location in unconfined coastal aquifers is highly impacted by tidal pumping (Kuan et al., 2012). A few studies have also demonstrated the role that tides play in the mixing dynamics near the saltwater-freshwater interface, and the influence on solute transport (Pool et al., 2014; Santos et al., 2012) and submarine groundwater discharge (Heiss & Michael, 2014; LeRoux et al., 2021; Robinson et al., 2007; Sawyer et al., 2016).

1.6 Dykelands

Dykelands are predominantly agricultural lands developed from pre-existing rich salt marshes through removing tidal influences in the surface and subsurface (Sherren et al., 2021). The pre-existing salt marsh plants worked to trap nutrient-rich sediments from the tidal waters, making this highly productive for crops (van Proosdij et al., 2010) in the absence of salinity. To this day, many dykelands worldwide still play an important role in agriculture production that supports local to global economies and food security (Chen et al., 2020; Sawyer et al., 2016; Tully et al., 2019). In addition to fostering and augmenting agricultural food production, dykes also protect coastal communities and offer many ecosystem services (Sherren et al., 2021; van Proosdij et al., 2014). Under current and future coastal change projections, many dykes in Atlantic Canada are inadequate and need to be altered to remain effective coastal barriers (Sherren et al., 2019). Current dykes in many other places worldwide are at risk of breaching and overtopping which can result in salinization of the agricultural land and devastate crop yields (Elsayed et al., 2018; Sherren et al., 2016).

1.6.1 Coastal change adaptation in dykelands

Dykes are of strategic importance for coastal adaptation to climate change and thus require proper management to ensure they can remain efficient barriers in the decades to come. Current dyke restoration techniques include topping up, retreating, or breaching (Figure 5) (van Proosdij & Page, 2015). Raising the dykes involves topping up their minimum critical elevations with sea-level rise and coastal storm projections in mind (Figure 5b) (van Proosdij & Page, 2015). However, this practice widens the dyke footings and requires more

land to maintain the proper slopes, and thus exacerbates coastal squeeze. In Nova Scotia, Canada, full responsibility for dyke upkeep falls under the Nova Scotia Department of Agriculture, which cannot afford to bring all dyke infrastructure in the province to 2050 sea-level and storm surge projections (Sherren et al., 2016). Managed realignment studies have shown that retreating the dykes provides opportunities to restore tidal wetlands which are self-adapting, act as buffers, and are cost effective (Figure 5c) (Singh et al., 2007). However, this approach reduces the extent of arable cropland, as moving dykes landward results in a loss of agricultural land and crop yield (Bhattachan et al., 2018). Lastly, breaching dykes results in complete abandonment of the agricultural land and full restoration of the pre-existing tidal wetlands (foreshore marsh) (Figure 5d) (Boone et al., 2017; Bowron et al., 2012). Restoration can occur passively (*i.e.*, with little human interference) or actively (*i.e.*, through planned removal and hydrology restoration) (Byers & Chmura, 2007; Luisetti et al., 2011; Proosdij et al., 2010).
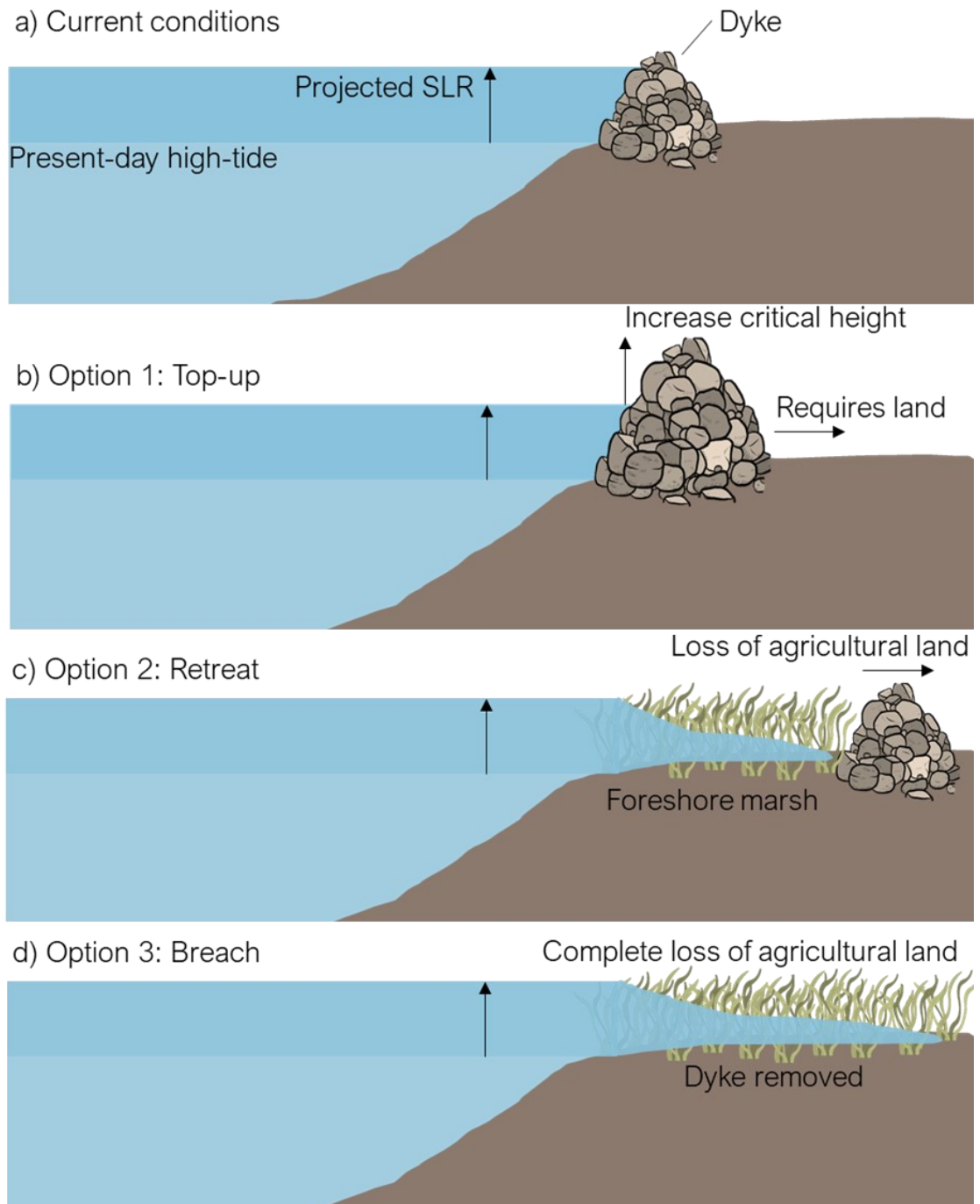
Figure 5. Dyke management techniques. a) Present-day dykes vulnerable to climate change, b) topping up dykes to prevent overtopping, c) retreating dykes back to restore some foreshore marsh, and d) breaching the dyke to completely restore the foreshore marsh.

1.6.2 Adaptation mechanism benefits and trade-offs for salt marshes vs. dykelands

When dykes are retreated or breached (Figure 5c, d), there are opportunities for regrowing coastal wetlands (salt marshes). Green infrastructure, such as wetlands, have proven to be an effective coastal defense mechanism due to their ability to dissipate wave energy through enhanced drag forces from the vegetation, thereby attenuating surge energy and flooding (Erwin, 2009; Sherren et al., 2021; Stark et al., 2015). Mature coastal wetlands can potentially offer more effective protection compared to hard sea barriers against marine climate change (Byers & Chmura, 2014; Temmerman et al., 2013). Studies have also shown that dyke removal substantially increases the amount of fresh groundwater discharging to the ocean, thus potentially reducing the extent of saltwater intrusion (White & Kaplan, 2017; Yang et al., 2010). However, there is a lack of studies that quantitatively investigate how the removal of coastal barriers influences the availability and quality of coastal fresh groundwater resources.

1.6.3 Saltwater intrusion in dykelands

Past dykeland studies do not typically consider the effects of saltwater intrusion into coastal aquifers in their climate change adaptation plans. In the rare cases for which saltwater intrusion is considered (*e.g.*, in the Netherlands, Kabat et al., 2005), it is a secondary concern that is not fully investigated. Ineffective governance structures have led to a lack of groundwater sustainability (Sherren et al., 2016), therefore placing fresh resources at risk of saltwater contamination.

Some thought has been put into surface manifestations of saltwater intrusion for landscapes with other forms of coastal defences (Carrión-Mero et al., 2021; Chang et al., 2011; Chang & Clement, 2012; Elsayed & Oumeraci, 2018b; Werner et al., 2013). One of the most relevant studies was conducted by Elsayed & Oumeraci (2018a) where the authors demonstrated how short-term threats like storm surges pose significant long-term risks such as saltwater intrusion that threaten the overall sustainability of coastal zones.

When considering saltwater intrusion in dykelands undergoing climate change, tidal dynamics play a large role in ocean forcing and therefore must be considered in conjunction with episodic coastal storms to truly understand the fate of these systems. Despite the evidence that tides play a large role in coastal aquifer interactions and groundwater dynamics, saltwater intrusion in mega-tidal dykelands and the impacts on ecosystem services remains understudied. In summary, there are virtually no studies that consider both short- and long-term drivers (*e.g.*, surges vs. sea-level rise or tidal dynamics) of saltwater intrusion in aquifers underlying dykelands. In addition to the lack or limited number of dykeland studies considering some form of saltwater intrusion, there are no dykeland groundwater studies that consider mega-tidal conditions, although tidal dynamics may play an important role in a coastal aquifer's response to overtopping and saltwater intrusion.

1.7 Ecosystem services and saltwater intrusion

Ecosystem services provide a stream of goods and services essential for society's well-being including categories such as provisioning (goods provided by ecosystems, *e.g.*, food production), regulating (benefits obtained from control of natural processes by ecosystems,

e.g., water filtration), cultural (non-material benefits obtained from ecosystems, *e.g.*, recreation), and supporting (essential for the production of all other services) (Mercer et al., 2014; Sherren et al., 2021). Despite numerous reports relating to deterioration of coastal environments, the value of ecosystem services continues to be poorly understood and largely unrecognized, which can result in direct economic and social repercussions that impact our well-being (Bennett et al., 2009; Mercer et al., 2014). Human activity has caused major declines in biodiversity and significant ecosystem degradation (Bennett et al., 2021; Preston & Raudsepp-Hearne, 2017). Without knowledge about relationships among ecosystem services, we are at risk of incurring unwanted trade-offs (Bennett et al., 2009). Furthermore, physical and biological changes associated with climate change have implications for the sustainability of ecosystem services, and ultimately for the well-being of coastal communities (Mercer et al., 2014). Understanding ecosystem service dynamics is critical to informing site-based management decisions to decide how to best protect our coastlines and coastal communities, as any decision involves trade-offs in services and disservices that often differ by beneficiary (Cimon-Morin et al., 2021; Sherren et al., 2021).

Coastal wetlands perform a unique set of physical, chemical, and biological functions, which provide billions of dollars of ecosystem services annually (Gómez-Baggethun et al., 2019; White & Kaplan, 2017). Wetlands face many environmental and anthropogenic pressures (*e.g.*, climate change, pumping) that threaten their function and limit their capacity to provide these services (Epanchin-Niell et al., 2018; White & Kaplan, 2017). Dykes are hard coastal barriers that are built to remove tidal influences from wetlands, thereby transforming formerly saline zones to highly productive freshwater agricultural land. Dykelands can be maintained and/or raised, allowing for the provision of a suite of

ecosystem services not limited to agriculture (Figure 5) (Sherren et al., 2021). Mature coastal wetland restoration due to dyke realignment/retreat may provide more effective protection than hard infrastructure (*e.g.*, dykes) against sea-level rise and storm surges and create more resilient coastal communities (Guimond & Michael, 2020; Sherren et al., 2021), but ultimately this coastal zone adaptation approach involves many ecosystem service trade-offs.

1.8 Knowledge gaps

There is evidently an urgent need to decide how to best restore or adapt dykelands with future climate change impacts such as sea-level rise and extreme storms in mind. Such decision making should consider coastal groundwater dynamics and agriculture productivity threatened by saltwater intrusion. Such considerations are critical for coastal communities, not just within the Canadian Maritimes, but worldwide. Additionally, no saltwater intrusion studies have considered mega-tidal conditions and the influence these large, cyclical perturbations can have on saltwater intrusion dynamics.

Given the knowledge gaps within the literature relating to saltwater intrusion in mega-tidal dykelands, this study will address the following research questions at a site-specific level, with hopes of future studies using these findings across large scales.

1. How do mega tides impact coastal-aquifer interactions and groundwater flow dynamics?

2. How does sea-level rise influence the location of the freshwater-saltwater interface and the upper saline plume in mega-tidal, dyked areas?

3. What influences do overtopping events have on the dyke systems and freshwater aquifer based on future climate projections and what impact would dyke removal have?

This study will use a combination of field and numerical modeling techniques to address these research questions in a holistic manner.

CHAPTER 2: STUDY SITE

2.1 Bay of Fundy, Nova Scotia

The Bay of Fundy, located within the Canadian Maritimes and northeastern USA, is known for having the highest tides in the world. The Minas Basin, connected to the Bay of Fundy, experiences current speeds that reach up to about 15 kph and transports nearly three billion cubic meters of water in and out of the basin with each tidal cycle (Wilson, 2016). The Bay of Fundy mudflats are consistently remolded by these large tidal perturbations and create a home for many marine algae as well as several species of resilient land plants (Percy, 1996). The mudflats consist of abundant nutrients that are essential to the ecosystems that thrive is these areas (Percy, 1996), but are increasingly vulnerable due to climate change.

French colonists (now known as Acadians) settled along the Bay of Fundy shores dating back to the 1600's and quickly recognized the agricultural potential of the large salt marsh bodies. The first dykes built were around 1.5 meters high and were veneered on both sides, with one-way drains (aboiteaux) extending through the base of the dykes (Percy, 1996). These drains were designed to allow water to drain seaward at low tide and prevent saltwater intrusion at high tide. Nova Scotia currently has 241 km of dykes that have primarily been used for protecting agricultural land from coastal threats (*e.g.*, Figure 6) (Sherren et al., 2016). At present, most dykes along the Bay of Fundy are below the critical elevation required to stop a 1:10 year storm (van Proosdij & Page, 2015), and pronounced sea-level rise projections for this region (Manson et al., 2019) further emphasize that present dyke locations and conditions must be rethought in order for them to remain effective coastal barriers (Sherren et al., 2019). Figure 7d shows the distribution of

dykelands within the province of Nova Scotia, Canada, which are all located along the Bay of Fundy or in tidal rivers that flow to the bay.

Figure 6. Aerial photograph of the dyke system near Wolfville, NS. Collected on October 14th, 2021, using the DJI Mavic Air 2.

2.2 Annapolis Valley, Nova Scotia

The Annapolis Valley is a rural area (Figure 7a), with towns and villages predominantly concentrated along rivers, containing one third of all the farmland in Nova Scotia (Rivard et al., 2012). The valley is composed of four counties, three of which border the Bay of Fundy, and contain the most productive agricultural area in the province (Trescott, 1968, 1969a). These counties are major economic regions due to the important agricultural areas that date back over 300 years. The tidal estuaries of the larger streams and rivers draining

the Annapolis-Cornwallis Valleys have been dyked to form rich pastureland, consisting of clay, silt, and sand deposited under the influence of both stream and tidal currents (Trescott, 1968). Dykes protect infrastructure and foster recreation, tourism, and a sense of place and identity (Sherren et al., 2016), therefore providing and promoting ecosystem services that people depend upon. Mixed farming characterizes much of the valley's land use, including the highest production of hay, tree fruits, vegetables, cattle, hogs, and chickens in the province (Davis & Browne, 1997). Adaption to sea-level rise is challenging in these landscapes used for food and goods production, and because of this, agricultural production in the Bay of Fundy has decreased (Sherren et al., 2016).
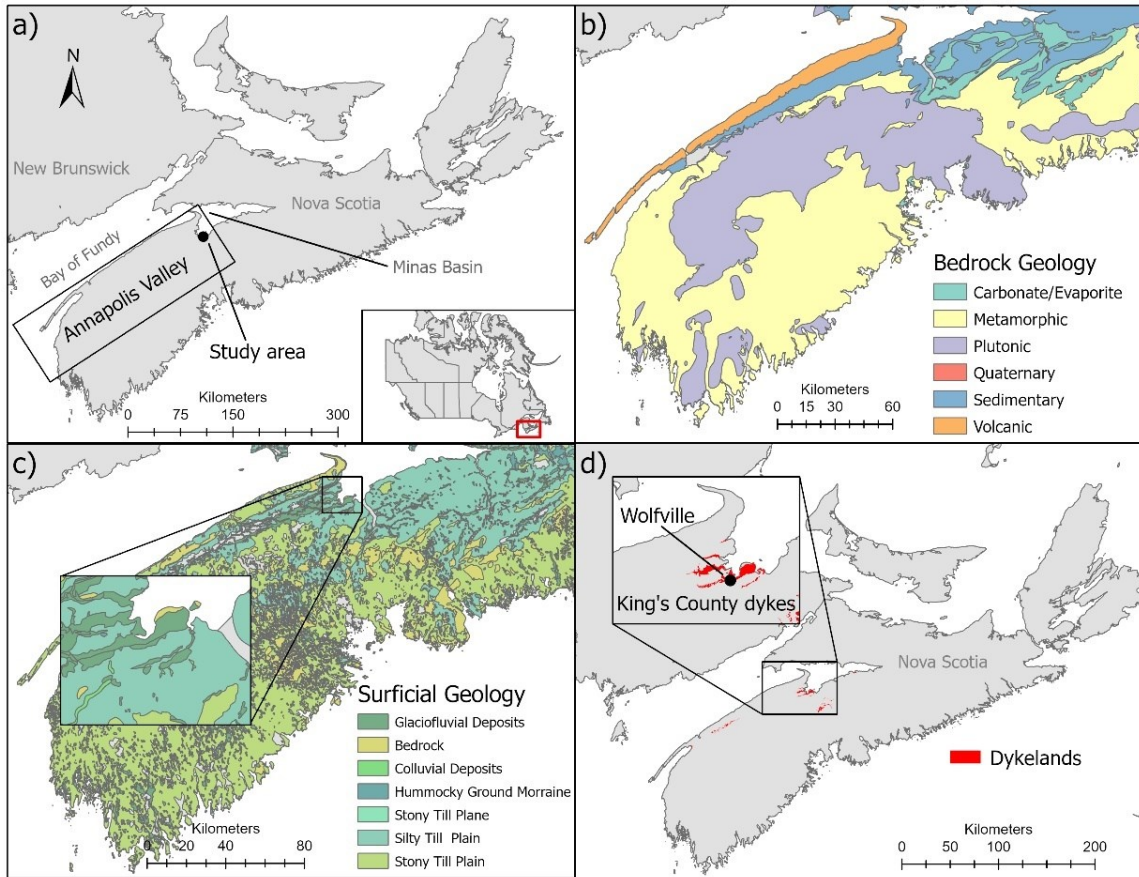
Figure 7. a) Map showing Nova Scotia (with inset showing location relative to Canada), the study area of interest for this project within the Annapolis Valley, and the relevant water bodies of interest; b) A simplified bedrock geology map for Nova Scotia (data from Kennedy & Drage., 2008); c) A surficial geology map for Nova Scotia (data from Stea et al., 1992*); d) Nova Scotia dykelands with the inset focusing on the key study area within King's County (data from* NRCAN, 2017).

Population growth, changes in land use, and droughts have put pressure on water resources in the Annapolis Valley (CBCL & WATER, 2009; Rivard. et al., 2006). Groundwater has therefore become an increasingly appealing water source due to the limited quantity and poor quality of surface water (Rivard. et al., 2006), and most valley residents now rely on groundwater for domestic purposes (Rivard et al., 2012). Salty groundwater is a problem in a few areas where wells have been constructed in flat low-lying dykelands (*i.e.*, where the freshwater-saltwater interface is relatively shallow) (Trescott, 1969a).

The town of Wolfville is located within Kings County in the Annapolis Valley, Nova Scotia (Figure 7a and d) and is bordered by several kilometers of dykes that protect agricultural practices that have been in place since the 1700's. In addition, these dykes protect the town's residential and industrial properties including the sewage treatment plant located approximately 100 m from the coastline's high tide mark. The municipality has expressed their concerns regarding climate change and the impacts it could have on their fresh groundwater supply and their agricultural crop production. The main process of concern is saltwater intrusion, which may already be occurring during summer months in the lower bedrock aquifer (Beebe, 2011). Chemical analyses have also suggested that the main water supply aquifer may be vulnerable to upconing of higher salinity water from the underlying Wolfville formation layer (Beebe, 2011). Hydraulic properties exert key controls on the water resources and vulnerability, and thus it is important to understand the underlying materials through which the water is supplied to understand the potential or occurrence of saltwater intrusion.

2.3 Annapolis Valley Geology

Identifying the underlying geological strata is important for improving the understanding of the hydrogeologic conditions within the Annapolis Valley. Bedrock geology is critical for determining the availability of water in deeper groundwater systems, whereas surficial geology is critical for understanding shallow groundwater resources and for salinized soil dynamics (Hiscock & Bense, 2014). Both bedrock and surficial geology units are addressed to assess potential groundwater quality and quantity from present formations in the Annapolis Valley. Geology also exerts key control on saltwater intrusion dynamics (Yang

et al., 2018). For example, geological properties can be used to identify flushing times (*i.e.*, how long it takes for an aquifer to desalinize) after flooding events occur (Paldor & Michael, 2021; Yang et al., 2015).

2.3.1 Bedrock geology

The bedrock geology along the Bay of Fundy (Figure 7b) consists of three main groups: the Wolfville (sedimentary) formation, the Blomidon (sedimentary) formation, and the North Mountain (volcanic) formation (Rivard. et al., 2006; Trescott, 1969b). The Wolfville formation is considered one of the most important aquifers in the Western Annapolis Valley and is composed of reddish, thickly bedded medium to coarse grained arenitic to subarkosic sandstone, with subordinate pebbly and conglomeratic beds (Rivard. et al., 2006). The water-bearing sandstone and conglomerate beds of this formation are usually confined by overlying beds of shale and/or siltstone, and wells drilled in this formation typically encounter water-bearing units (Hennigar, 1972). These sandstones are generally weakly cemented and loosely consolidated which allows the movement of water through its pore spaces (Hennigar, 1972). In certain areas, the Blomidon formation overlies the Wolfville Formation and comprises the same lithologic types as the Wolfville formation, but with finer grained beds (Rivard. et al., 2006). In other areas, the North Mountain Formation overlies the Wolfville or Blomidon formations and consists of a series of massive and amygdaloidal basalt flow (Rivard. et al., 2006). The coastal areas near the town of Wolfville are underlain primarily by the Wolfville formation.

2.3.2 Surficial geology

The surficial geology within the Annapolis Valley (inset, Figure 7c) is characterized by heterogeneity associated with the major depositional systems of glacial settings within the Bay of Fundy region (Rivard. et al., 2006). Deposits of surficial sediments are thinner in the upland areas, but are often thicker in the valley region, reaching up to 10 m (Rivard. et al., 2006). Sand and gravel deposits form very good aquifers in the eastern part of the valley (Rivard. et al., 2006). The town of Wolfville uses these surficial sediments as part of their water supply, and this material extends while gradually decreasing in the vertical dimension as it approaches the coastline (Rivard. et al., 2006). This aquifer is overlain by a fine-grained silty glaciomarine clay that is nutrient rich from the sediments that were deposited from the Bay of Fundy. Other surficial deposits are predominately fine-grained and poor aquifers, and the majority of domestic water supplies are obtained from dug wells constructed in glacial till (Trescott, 1969b).

2.4 Bay of Fundy hydrogeology

The geologic framework in coastal aquifer settings controls the main hydrogeological processes and dynamics. The main bedrock aquifers occur in the Wolfville and Blomidon formations, and to a lesser extent, in the North Mountain basalts (Rivard. et al., 2006). Preferential groundwater recharge occurs over the Wolfville formation due to the flat topography and coarse-grained material (Rivard. et al., 2006). Glaciofluvial deposits are more permeable and store more water per unit volume than any other hydrostratigraphic unit in the area (Trescott, 1969a). Groundwater can be exploited in relatively high quantities in the study area, especially within the Wolfville formation or glaciofluvial sand/gravel

deposits, which can be found within the town where most of the population is located (Rivard et al., 2012). The Wolfville area consists of three primary layers: a glaciofluvial clay confining layer (aquitard), a sand/gravel surficial aquifer layer (aquifer), and a sandstone water-bearing and fractured bedrock layer (aquifer) (Hennigar & Kennedy, 2006). The town of Wolfville relies on the sand aquifer as their primary source of water.

CHAPTER 3: FIELD AND NUMERICAL METHODS

3.1 Introduction to fieldwork and instrument locations

Numerous field techniques were employed to characterise the hydrogeology and evaluate the present and future vulnerability to saltwater intrusion for the town of Wolfville, Nova Scotia. Much of the data collected for this study were used to calibrate a numerical model as described in subsequent sections; however, some data described in this section (particularly for the salt marsh) are part of the field study that relates to the overarching goals of characterising groundwater-basin interactions and were not necessarily used for numerical model development. Figure 8 shows the locations for the instruments, which are further described in this chapter. A wave buoy and tidal station were installed in the Minas Basin (connected to the Bay of Fundy), a deep drilled well in the Wolfville formation was instrumented and monitored, four shallow piezometers were installed in the glaciomarine layer of the salt marsh, and geophysical surveys were conducted at seven different locations using time-domain resistivity data. All instruments were surveyed using a differential global positioning system (DGPS) to later convert readings to be with respect to mean sea level (msl). The modeling transect used in HydroGeoSphere (HGS) and the sewage treatment plant (STP) are shown for reference (Figure 8). Figure 9 shows examples and photos of the field techniques and instruments deployed.
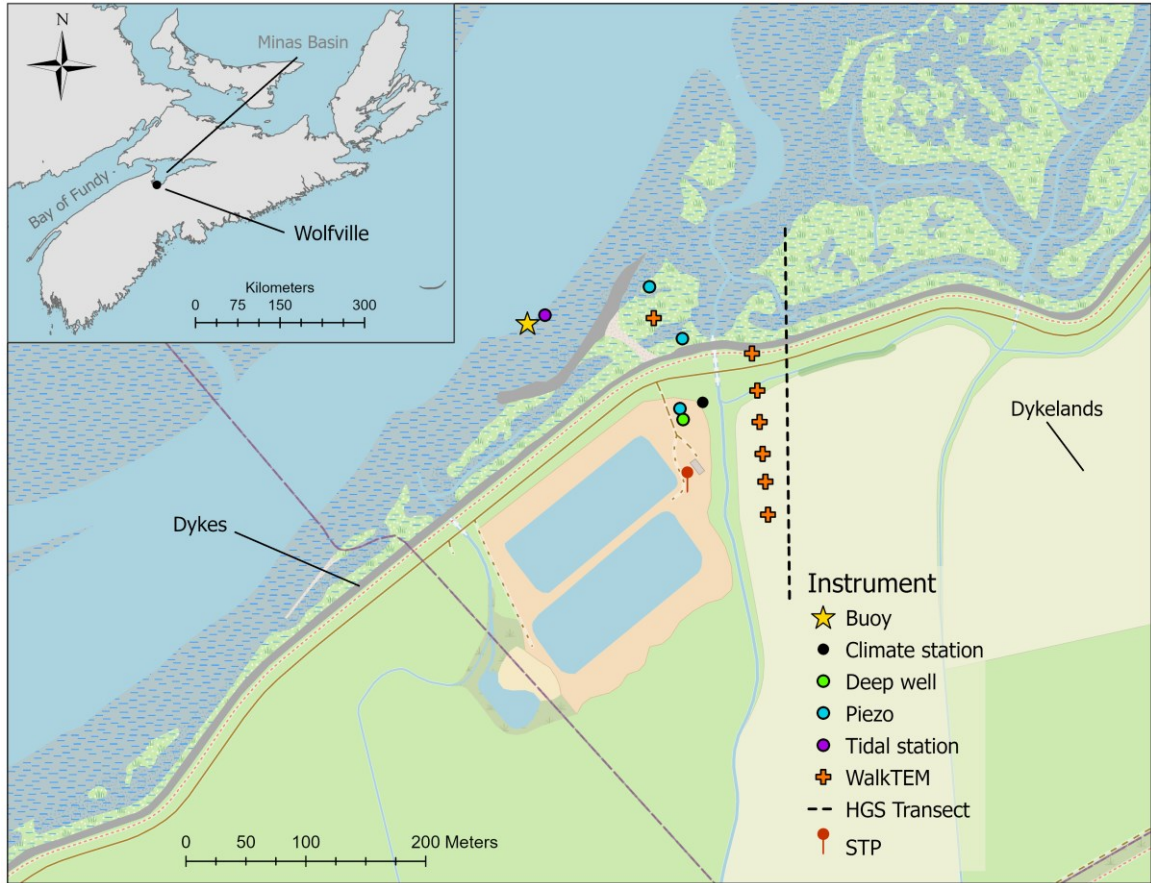
Figure 8. Locations of instruments deployed for the 2020 and/or 2021 field seasons. Instruments deployed include a SoFar Spotter wave buoy, tidal station (Hobo water level logger), and five Solinst LTC loggers in piezometers and wells. The locations where resistivity points were collected using the time-domain (WalkTEM) electromagnetic geophysical instrument are also shown. The transect used to model in HydroGeoSphere (HGS) and the Wolfville sewage treatment plant (STP) are shown for reference. Base map source: ESRI©.
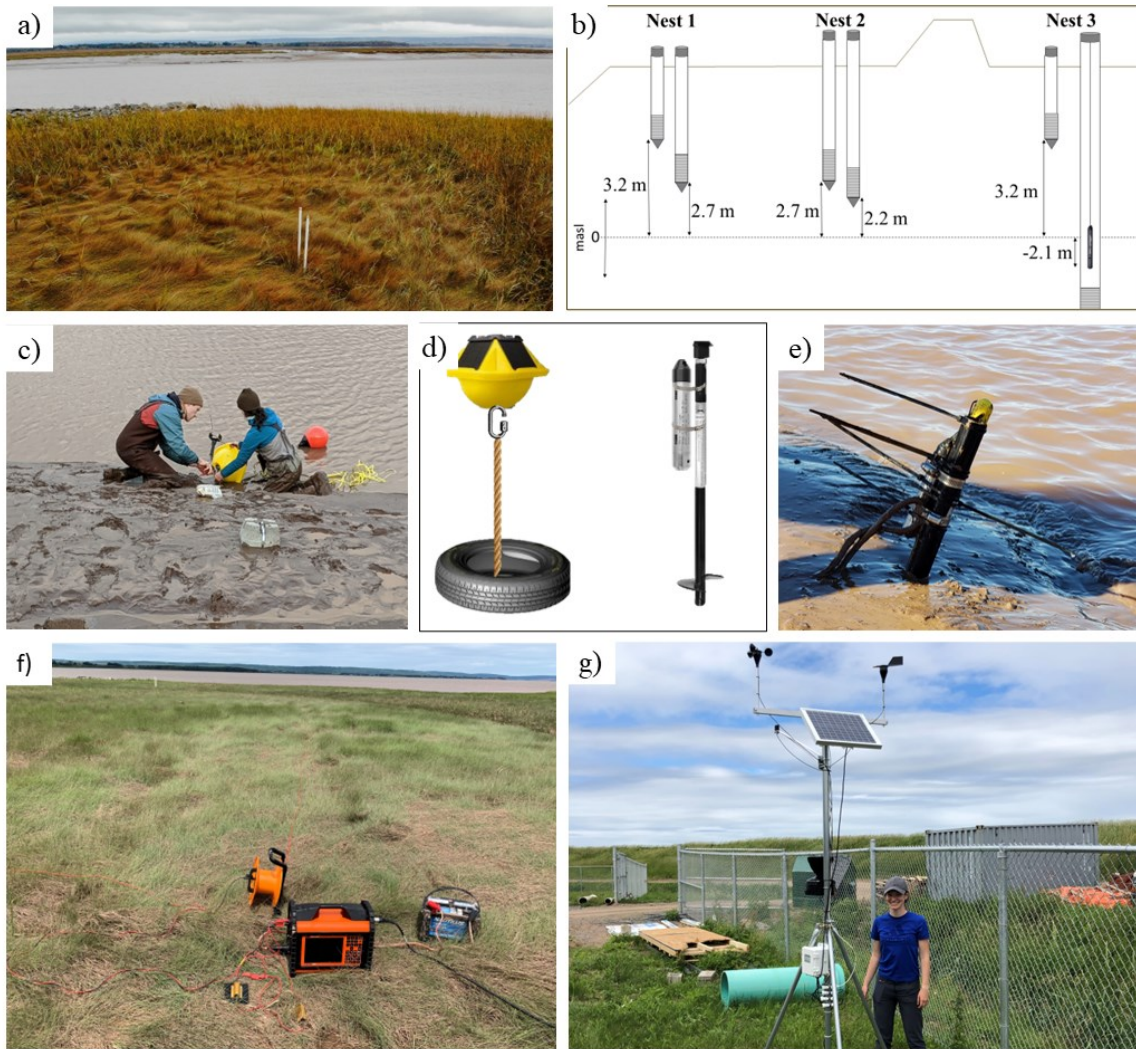
Figure 9. Instruments deployed for the field study in Wolfville, NS with all locations shown in Figure 8. a) Drilled piezometers that are part of nest 1 (photo taken October 14, 2021), b) piezometer elevations with respect to mean sea level (the hump indicates the dyke), c) wave buoy deployment in the Minas Basin (photo taken November 17th, 2020), d) wave buoy (left) and tidal logger (right) deployment techniques, e) tidal logger deployment in the Minas Basin at spring low tide (photo taken September 21st, 2020), f) WalkTEM geophysical survey point in an agricultural field (photo taken June 25th, 2021), and g) climate station deployment (photo taken June 25th, 2021).

3.2 Fieldwork methodology

3.2.1 Climate monitoring

A HOBO RX3000 remote monitoring station data logger (ONSET, 2021) was installed to monitor wind speed and direction, air pressure, air temperature, relative humidity, dew point, precipitation, and solar radiation (Figure 8 and Figure 9g). Current, local climate data

are important for developing representative model boundary conditions for present-day simulations and to understand the relationship between atmospheric forcing and coastal groundwater response. The nearest climate station that is operated by Environment and Climate Change Canada is in the town of Kentville, Nova Scotia, which is approximately 15 km away, and the climate between two areas that are this far apart can be markedly different. Climate data were used to calculate potential evapotranspiration, which could then be used in concert with precipitation data to estimate annual recharge rate to compare with other recharge estimates (*e.g.*, Hennigar & Kennedy, 2006). Recharge is used to form the atmospheric boundary condition in the model later described in section 4.1.1. The rate of potential evapotranspiration (*PET*) was calculated (Eq. 2) using the Priestly-Taylor method (Xu & Singh, 2002), which is a simplification of the Penman method (Penman, 1948):

$$PET = \alpha \frac{\Delta}{\Delta + \gamma} \frac{R_n}{\lambda} \qquad [2]$$

where *PET* is the potential evapotranspiration [mm day^{-1}], α is the albedo or canopy reflection coefficient [dimensionless], Δ is the slope of the saturation vapor pressure curve at air temperature T [kPa °C^{-1}], R_n is the net radiation [cal cm^{-2} day^{-1}], and γ is the latent heat of vaporization [MJ kg^{-1}].

3.2.2 Shallow piezometers

A series of coastal piezometers were installed in front of the dyke to investigate groundwater dynamics in the salt marsh and indirectly obtain hydraulic properties of the

overburden (*i.e.*, clay) layer. The piezometers were drilled into the overburden (Figure 9a) with depths shown in Figure 9b (*i.e.*, nest's 1 and 2) and were built using 0.0254 m (1-inch) PVC casing with 0.2 m long slotted sections and pointed tips on the bottom, a compression plug at the top, and a drilled hole at the top to vent the piezometer to the atmosphere. Holes for these piezometers were drilled using a Shaw backpack drill (Shaw, 2011) with a 5.08 cm (2-inch) diameter bit size. Solinst level-temperature-conductivity (LTC, Solinst, 2020) loggers (M20 model, +/- 1 cm accuracy, 0.0006% resolution) were installed in all 4 piezometers to monitor the level, temperature, and electrical conductivity (salinity) of the groundwater over tidal cycles between September 11th, 2020, and August 24th, 2021. Figure 8 shows the locations of the piezometers installed along the coastline near the town of Wolfville, Nova Scotia. Figure 8a and b show an example of what the installed piezometers look like from the surface, and the relative elevations of the piezometers with respect to mean sea level. The deeper piezometer in nest 2 was eventually moved to become the shallow piezometer in nest 3. The deep monitoring well that is part of nest 3 is described in the next section.

These piezometers were installed to: (1) to identify dominant tidal constituents in the groundwater system and to obtain the associated amplitudes/relative phases and (2) obtain vertical and horizontal hydraulic gradients and water levels. It is important to note that these piezometers were installed in the salt marsh, which was not explicitly considered as a different zone in the numerical model described later. Thus, the piezometer data was not explicitly considered in the numerical model development, but it did yield additional insight into groundwater-basin interactions.

The groundwater tidal constituents can also be analysed with analytical solutions in conjunction with the piezometer locations to obtain aquifer hydraulic properties (Jacob, 1950; Li & Jiao, 2001; Nielsen, 1990; van der Kamp, 1972). The governing equation [3] developed by Jacob (1950) and boundary conditions [4, 5] are shown below:

$$\frac{\partial h}{\partial t} = D \frac{\partial^2}{\partial x^2} \qquad [3]$$

$$h(x = 0, t) = H_o \sin(\omega t) \qquad [4]$$

$$h(x = \infty, t) = 0 \qquad [5]$$

where D is the hydraulic diffusivity [$m^2\,hr^{-1}$], x is the distance between the well and the ocean or basin [m], t is the time [hr], H_o is the amplitude of the tidal signal [m], and ω is the angular wave frequency [rad/hr].

The associated analytical solution is (Jacob, 1950):

$$h(x,t) = H_o e^{\left(-x\sqrt{\frac{\omega}{2D}}\right)} \sin\left(\omega t - x\sqrt{\frac{\omega}{2D}}\right) \qquad [6]$$

where $h(x,t)$ is the hydraulic head at a point in space and time within the aquifer [m]. Importantly, this equation demonstrates that signals are exponentially damped and linearly lagged with distance inland. This equation can be rearranged to estimate hydraulic diffusivity based on a phase shift or damping of a groundwater tidal signal compared to the ocean tidal signal.

Many more complex analytical approaches exist to study tidal groundwater dynamics and infer aquifer properties (Zhang et al., 2021). However, the simple form is presented herein to demonstrate the possibility of aquifer property estimation based on the amplitude of tidal groundwater signals. In this study, the analytical solution was not used to estimate the aquifer properties given the assumptions invoked in the solution (*e.g.*, linear, homogeneous system). Rather, the numerical model properties were adjusted to match numerical model output with observations of groundwater tidal signals as described later.

In addition to using multi-level piezometers for the purpose of monitoring groundwater levels, the piezometers were also installed to obtain vertical and horizontal hydraulic gradients. Vertical hydraulic gradients can tell us whether there are upwelling or downwelling conditions. Here and throughout, a negative vertical gradient refers to positive downwelling conditions.

3.2.3 Deep drilled well monitoring

A deep drilled well owned by the town of Wolfville was instrumented and monitored to investigate the groundwater level and electrical conductivity dynamics and obtain hydraulic parameters for the deeper confined groundwater flow system. This well was monitored with the same type of Solinst LTC logger (Solinst, 2020) that was used in the shallow piezometers. The location of this well and the dimensions are shown in Figure 8 and Figure 9b (nest 3), respectively. This well is 70 m deep and therefore penetrates the Wolfville formation where it is screened (*i.e.*, bedrock layer). Similar to the shallow piezometer analysis approach, analysis of the tidal constituents (particularly the amplitude) obtained

from this deep groundwater well was used in conjunction with numerical model output to estimate the hydraulic diffusivity (and thus the hydraulic conductivity) for the bedrock formation and update the model parameterization.

3.2.4 Wave monitoring

To investigate the likelihood of present and future waves overtopping the dykes, a wave buoy (SOFAR Spotter, San Francisco) was installed to capture significant wave heights (average amplitude of the highest 1/3 of the waves), peak wave periods, mean wave directions, and mean (estimated from waves) wind directions and speeds (Figure 9c). The wave buoy measures 3D surface motions at 2.5 Hz and then translates that to wave motions at a frequency of 1 Hz (Raghukumar et al., 2019). The buoy was installed in the Minas Basin, Nova Scotia (Figure 8), using the deployment schematic shown in Figure 9d. The buoy was attached to a concrete-filled tire (weighing approximately 200 lbs) using polypropylene rope (3/8" diameter, 140 lb safe workload) and zinc-platted quick link bolts (Figure 9d).

3.2.5 Tide monitoring

To form the main seaward tidal boundary condition in the model domain, a HOBO water level logger (20 m depth rating) was installed in the Minas Basin, Nova Scotia to capture the tidal levels (Figure 9d and e). The Minas Basin primarily experiences a semi-diurnal tidal period with spring and neap tidal constituents. Frequency domain analysis (Carr, 1971; Frigo & Johnson, 1998; Pawlowicz et al., 2002) was used to analyse this time series to obtain dominant tidal amplitudes and frequencies to estimate aquifer hydraulic properties

(Nielsen, 1990) within the numerical model. Frequency domain analyses for the groundwater levels and tidal levels were conducted in Matlab using the Fast Fourier Transform (FFT) function (Frigo & Johnson, 1998).

3.2.6 Geophysical surveys

To compare model outputs of the saltwater-freshwater interface with field measurements, time-domain electromagnetic geophysical surveys were conducted using the ABEM WalkTEM (Guideline Geo, Figure 9f). This instrument can be used to obtain ground resistivity values down to depths on the order of 100 m (using the 20 × 20 m loop setup). These points can then be post-processed to generate a 1D or 2D ground resistivity distribution which can be used to infer porewater salinity and stratigraphy changes (Singha et al., 2022). The WalkTEM measures bulk resistivity changes, and thus Archie's (1942) law (Eq. 7) must be used to convert bulk resistivity to porewater resistivity (and thus salinity):

$$R_o = \theta^{-m} R_w \qquad\qquad [7]$$

where R_o is the resistivity of the material when all pores are filled with saltwater [Ω m], θ is the porosity fraction of material [dimensionless], m is the slope of the line representing the relation [dimensionless], and R_w is the resistivity of the saltwater [Ω m].

Archie's law is useful for differentiating between stratigraphy and water salinity changes which is crucial in areas where the geology is complex and variable, and where the ocean-aquifer interactions are highly dynamic (Archie, 1942). With manually obtained resistivity

readings of the saltwater (R_w) and freshwater, the bulk resistivity of the saltwater and porous media can be obtained and directly compared to the resistivity output from the WalkTEM to delineate zones of fresh, brackish, and saline groundwater. However, this delineation can be complicated by geological heterogeneity, which introduces bulk resistivity changes even without any changes to porewater resistivity.

3.3 Numerical modeling methodology

In this study, a numerical surface-subsurface model was used to assess the present and future states of groundwater flow and saltwater intrusion dynamics for the Bay of Fundy dykelands. The results were used to provide dykeland management recommendations based on current and future risks to fresh groundwater resources.

3.3.1 Numerical model

HydroGeoSphere (HGS) is a three-dimensional, fully integrated, control-volume finite element or finite difference simulator developed by Aquanty (Therrien & Sudicky, 1996). This model was designed to consider all key components of the hydrologic cycle. For each time step, the model simultaneously solves surface and subsurface flow and mass transport equations using the finite element or finite difference approach (Aquanty, 2015b). This model was selected for this study as it is a rigorous, fully coupled model that can resolve coupled surface and subsurface processes, thus eliminating the need to combine inputs and results from separate surface and subsurface models when considering coastal aquifer dynamics (Elsayed & Oumeraci, 2018a; Storlazzi et al., 2018). HGS is also a highly

optimized numerical simulator capable of solving highly non-linear equations through its adaptive time stepping techniques.

The surface water budget can be written as:

$$P = (Q_{S2} - Q_{S1}) - Q_{GS} + ET_S + Q_S^W + \Delta S_S / \Delta t \qquad [8]$$

and the subsurface water budget as:

$$I = (Q_{G2} - Q_{G1}) + Q_{GS} + ET_G + Q_G^W + \Delta S_G / \Delta t \qquad [9]$$

where P is the precipitation [m], I is the infiltration [m], Q_{S1} and Q_{S2} are respectively the surface water inflow and outflow [m^3 s^{-1}], Q_{G1} and Q_{G2} are respectively the subsurface water inflow and outflow [m^3 s^{-1}], Q_{GS} is the surface/subsurface water interactive flow [m^3 s^{-1}], ET_S is the evapotranspiration from the surface flow system [m^3 s^{-1}], ET_G is the evapotranspiration from the subsurface flow system [m^3 s^{-1}], Q_S^W is the overland water withdrawal [m^3 s^{-1}], Q_G^W is the subsurface water withdrawal [m^3 s^{-1}], ΔS_s is the surface water storage over time step Δt [s^{-1}], and ΔS_G is the subsurface water storage over time step Δt [s^{-1}].

HGS uses the two-dimensional depth-integrated diffusion-wave approximation of the Saint Venant equations along with the Manning equation, both for surface water flow, coupled with the Richards' equation for three-dimensional, variably saturated subsurface flow (Aquanty, 2015b). The advection-dispersion equation is used for problems that involve solute transport.

The two-dimensional Saint Venant equations used to describe the surface domain flow are shown by Eqs. [10] (mass balance), [11] (momentum for the x-direction), and [12] (momentum for the y-direction):

$$\frac{\partial \phi_o h_o}{\partial_t} + \frac{\partial (\bar{v}_{xo} d_o)}{\partial_x} + \frac{\partial (\bar{v}_{yo} d_o)}{\partial_y} + d_o \Gamma_o \pm Q_o = 0 \qquad [10]$$

$$\frac{\partial}{\partial_t}(\bar{v}_{xo} d_o) + \frac{\partial}{\partial_x}(\bar{v}^2{}_{xo} d_o) + \frac{\partial}{\partial_y}(\bar{v}_{xo} \bar{v}_{yo} d_o) + g d_o \frac{\partial d_o}{\partial_x} = g d_o (S_{ox} - S_{fx}) \qquad [11]$$

$$\frac{\partial}{\partial_t}(\bar{v}_{yo} d_o) + \frac{\partial}{\partial_y}(\bar{v}^2{}_{yo} d_o) + \frac{\partial}{\partial_x}(\bar{v}_{xo} \bar{v}_{yo} d_o) + g d_o \frac{\partial d_o}{\partial_y} = g d_o (S_{oy} - S_{fy}) \qquad [12]$$

where d_o is the depth of flow [m], z_o is the bed (land surface) elevation [m], h_o is the water surface elevation [m], $\bar{v}_{xo}$ and $\bar{v}_{yo}$ are the vertically averaged flow velocities in the x- and y-directions [m s^{-1}], Q_o is the volumetric flow rate per unit area representing external sources and sinks [m s^{-1}], ϕ_o is the surface flow domain porosity [dimensionless], S_{ox} and S_{oy} are the bed slopes in the x- and y-directions [dimensionless], and S_{fx} and S_{fy} are the friction slopes in the x- and y-directions [dimensionless]. HGS uses the modified form of Richards' equation to simulate three-dimensional groundwater flow in a variably saturated porous matrix (Therrien & Sudicky, 1996):

$$-\nabla \cdot (\omega_m \boldsymbol{q}) + \sum \Gamma_{ex} \pm Q = \omega_m \frac{\partial}{\partial t}(\theta_s S_w) \qquad [13]$$

where w_m is the porous media volume fraction of total porosity [dimensionless], $\boldsymbol{q}$ is the fluid flux vector [m s^{-1}], Γ_{ex} is the volumetric fluid exchange rate between the subsurface domain and other domains [m^3 m^{-3} s^{-1}], Q is the volumetric fluid flux per unit volume

representing a source (+) or sink (-) to the porous media system [m³ m⁻³ s⁻¹], θ_s is the saturated water content (porosity) [dimensionless], and S_w is the degree of water saturation [dimensionless]. For this flow equation, HGS assumes that the fluid is essentially incompressible, the porous medium and fractures, if present, are non-deformable, the system is under isothermal conditions, and the air phase is infinitely mobile (Aquanty, 2015a).

Additionally, HGS uses a dual node approach (Eq. 14) which is chosen to represent simultaneous flow in the subsurface and surface domain where the exchange term is given by (Aquanty, 2015b):

$$d_o \Gamma_o = w_m \frac{k_r K_{zz}}{l_{exch}} (h - h_o) + w_d \frac{k_{dr} K_{dzz}}{l_{exch}} (h_d - h_o) \qquad [14]$$

where d_o is the surface (overland) flow water depth [m], Γ_o is the dual continuum volumetric fluid exchange rate from the subsurface to surface system [m³ m⁻³ s⁻¹], h_o is the surface water head [m], h and h_d are respectively the subsurface porous medium and dual medium heads [m], w_d is the dual continuum volumetric fraction of total porosity [dimensionless], k_r and k_{dr} are respectively the relative permeabilities of underlying porous media and dual media [dimensionless], K_{zz} and K_{dzz} are respectively the vertical saturated hydraulic conductivities of underlying porous/dual media [m s⁻¹], and L_{exch} is the coupling length [m].

Two-dimensional solute transport along the surface domain is represented as [Eq. 15]:

$$-\bar{\bar{\nabla}}(q_o C_o - \boldsymbol{D_o} \emptyset_o h_o \bar{\nabla} C_o) + [\emptyset_o h_o R_o \lambda C_o]_{par} - d_o \Omega_o = \frac{\partial}{\partial t}(\emptyset_o h_o R_o C_o) + \emptyset_o h_o R_o \lambda C_o \quad [15]$$

where C_o is the solute concentration in the surface domain [kg m^{-3}], $\boldsymbol{D_o}$ is the hydrodynamic dispersion tensor of the surface flow domain [m^2 s^{-1}], R_o is the retardation factor [dimensionless], λ is the solute first-order decay constant, and *par* is the parent species for the case of a decay chain.

The three-dimensional subsurface transport of solutes [Eq. 16] is calculated using the control volume finite element method (Aquanty, 2015b):

$$-\nabla \cdot w_m(\boldsymbol{q}C - \theta_s S_w \boldsymbol{D} \nabla C) + [w_m \theta_s S_w R\lambda C]_{par} + \sum \Omega_{ex} \pm Q_c = w_m \left[\frac{\partial}{\partial t}(\theta_s S_w RC) + \theta_s S_w R\lambda C \right] \quad [16]$$

where Q_c is the solute exchange with the outside as a source (+) or sink (-) to the porous media system [kg m^{-3} s^{-1}], and Ω_{ex} is the mass exchange rate of solutes per unit volume [kg m^{-3} s^{-1}].

For non-linear equations, HGS uses the Newton-Raphson linearization method for solving the equations for variably saturated subsurface flow, surface flow, and solute transport, including density-dependant flow and transport (Aquanty, 2015b).

3.3.2 Conceptual model

A conceptual model is a qualitative representation of a groundwater system that conforms to hydrogeological principles and is based on geological, geophysical, hydrological, and hydrogeochemical data or understanding as well as other ancillary information (Anderson et al., 2015). A 2-D transect extending between the Minas Basin and the town of Wolfville was selected for this study (Figure 8). This transect captures both surface and subsurface features of interest but does not directly overlie all the locations of the wells or geophysical

45

surveys as a perfectly perpendicular (~ north) transect was used. However, these locations are close (within 10s of metres, Figure 8) to the transect and can be assumed to be representative of conditions along the transect at the same cross-shore distance. Two-dimensional models are useful for conducting high-level analyses and comparing larger-scale changes over time where there is symmetry about an axis, without the added complexities associated with the third dimension (Reilly & Harbaugh, 2004).

Figure 10 shows the conceptual model and boundary conditions used to drive the model. In the surface domain, a simplified version of the land surface elevation (digital elevation model obtained from LiDAR) defines the top boundary. A nodal rain flux is used to force recharge along the top of the domain (Figure 10, top blue), and the recharge rate of 100 mm/yr was obtained from a previous Wolfville groundwater modeling study (Hennigar & Kennedy, 2006). The seaside boundary condition (Figure 10, red) includes a second-type (Neumann) time-varying derivative of head with a first-type (Dirichlet) specified salt concentration, both applied in the surface domain. In the subsurface domain, the groundwater dynamics are influenced by the stratigraphy which includes a clay confining layer, a sand/gravel aquifer, and a fractured bedrock layer (Figure 10) that extends to the bottom of the domain. To impose the mega-tidal conditions of the Bay of Fundy, the landside boundary condition (Figure 10, blue left side) includes a first-type (Dirichlet), specified head boundary (nodal value) representing the average groundwater level. The boundary condition at the bottom and right sides of the domain (Figure 10) include a second-type (Neumann) no-flow and no-solute transport boundary (elemental value). This conceptual model generally agrees with a former modeling report that was conducted near the present model location (e.g., Hennigar & Kennedy, 2006), although this former study

did not include solute transport, variable density flow, tidal forcing, sea-level rise, or coupled surface and subsurface dynamics.

Specified head = 1 masl
$C/C_o = 0$

Specified flux = 100 mm/yr
$C/C_o = 0$

Surface domain

Dyke

Specified head = time-varying
$C/C_o = 1$

Subsurface domain

Clay

Sand

Bedrock
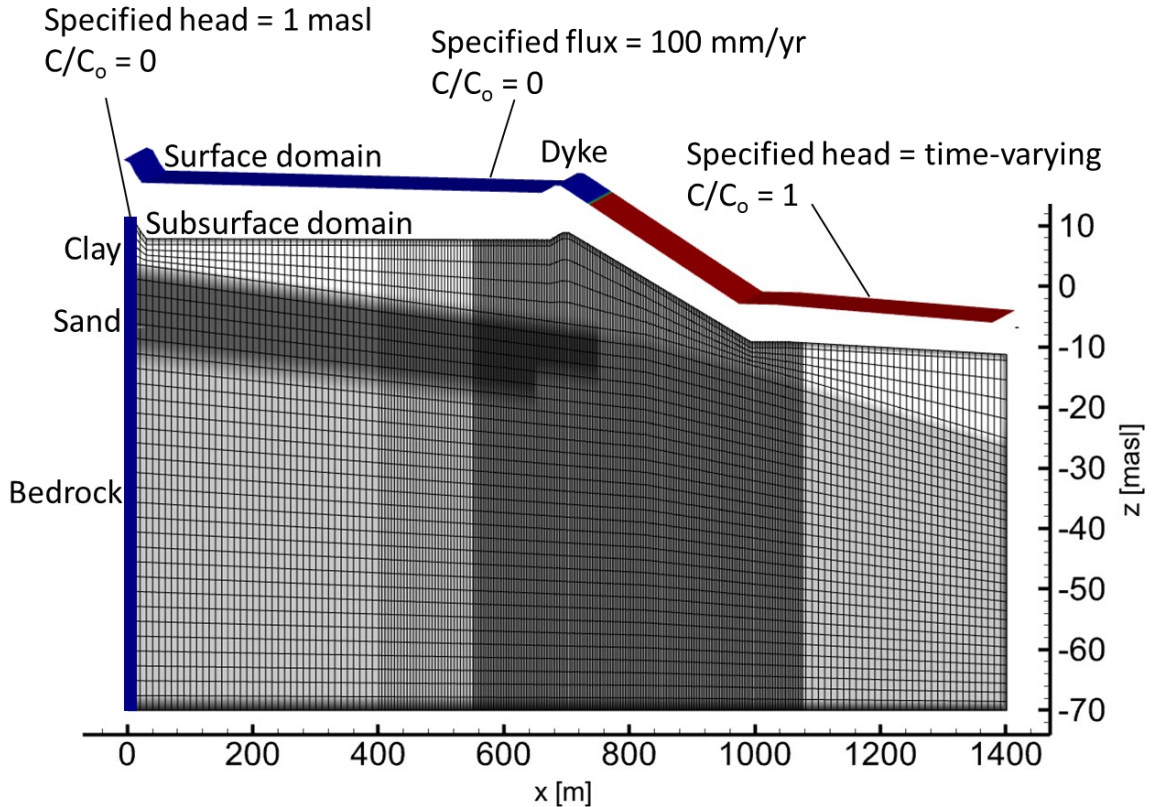
Figure 10. Conceptual model of the domain stratigraphy with geological layers and boundary conditions. The mesh density is superimposed on the conceptual model to illustrate the final discretization.

A simple, rectangular element mesh (with a unit thickness into the page) was chosen for this model. The domain extends 70 meters deep below mean sea level, and this depth was selected due to the depth of a key observation well, which served as a calibration point. Based on an iterative mesh density investigation process, the horizontal and vertical element dimensions vary within the domain, with the areas of most interest having the smallest element sizes. Increasing the mesh density near the Minas Basin and the dyke allows for more nodal and elemental data to be generated in the areas that are most heavily

influenced by the tides. Element sizes range from 1.0 to 2.5 meters in height and 2.5 to 10 meters in width. While these are large elements for the unsaturated zone dynamics (described later), the focus was on the impacts of sea-level rise, overtopping, and tidal forcing on saltwater intrusion dynamics. Larger elements were used on the landward side of the domain where there is less tidal influence on the groundwater dynamics. The total number of elements and nodes were 10,955 and 22,608, respectively.

3.3.3 Modeling process and calibration

The HGS modeling and data processing steps used in this study are shown in Figure 11. An initial, steady-state simulation was conducted to achieve a stable groundwater flow and salt transport solution, which was then further used as an initial condition for quasi-steady transient simulations (*i.e.*, tidal boundary turned on but repeating) to calibrate hydraulic heads. The hydraulic conductivity and storage values (Table 2) were adjusted to achieve a satisfactory wedge location and head amplitude that were in general agreement with our field observations. The groundwater flow and salt transport simulation (constant density) was also used as an initial condition for a transient simulation (*i.e.*, mega-tidal boundary) with variable density effects turned on to calibrate the saltwater-freshwater interface location and upper saline plume. This simulation was run until a dynamic equilibrium was achieved to ensure the transition zone and upper saline plume due to tidal forcing was established. Two different tidal boundary conditions (no-tide and mega-tidal) were later used in separate simulations to assess the influences of tides in the groundwater-ocean exchange and flushing rates following overtopping.

There are inherent difficulties associated with running density-dependant flow simulations in numerical models with complex systems (Brovelli et al., 2007) such as mega-tidal scenarios with variable saturation, thus a mean tidal head boundary (*i.e.*, no tidal signal, but with the mean tide level increasing gradually due to sea-level rise) was used for climate change scenarios to decrease simulation run times. The tidal boundary was only turned on upon completion of the climate change projection simulations (*i.e.*, for the final sea level condition). Upon achieving a satisfactory calibration with field data for present groundwater flow conditions, climate change projections were imposed to assess the impacts of saltwater intrusion via sea-level rise (mode 1) and more intense coastal storms (mode 2). Due to the complexity of these simulations, all model runs were completed using Siku through ACENET, which is a high-performance computer cluster located at Memorial University in St. John's, Newfoundland (https://wiki.ace-net.ca/wiki/Siku). This generally decreased simulation time by over an order of magnitude compared to the lab's high-performance computers. However, simulation times remained high. For example, for the SLR scenarios, simulations took approximately 20 days to run out for 2 years of model time with tides turned on.
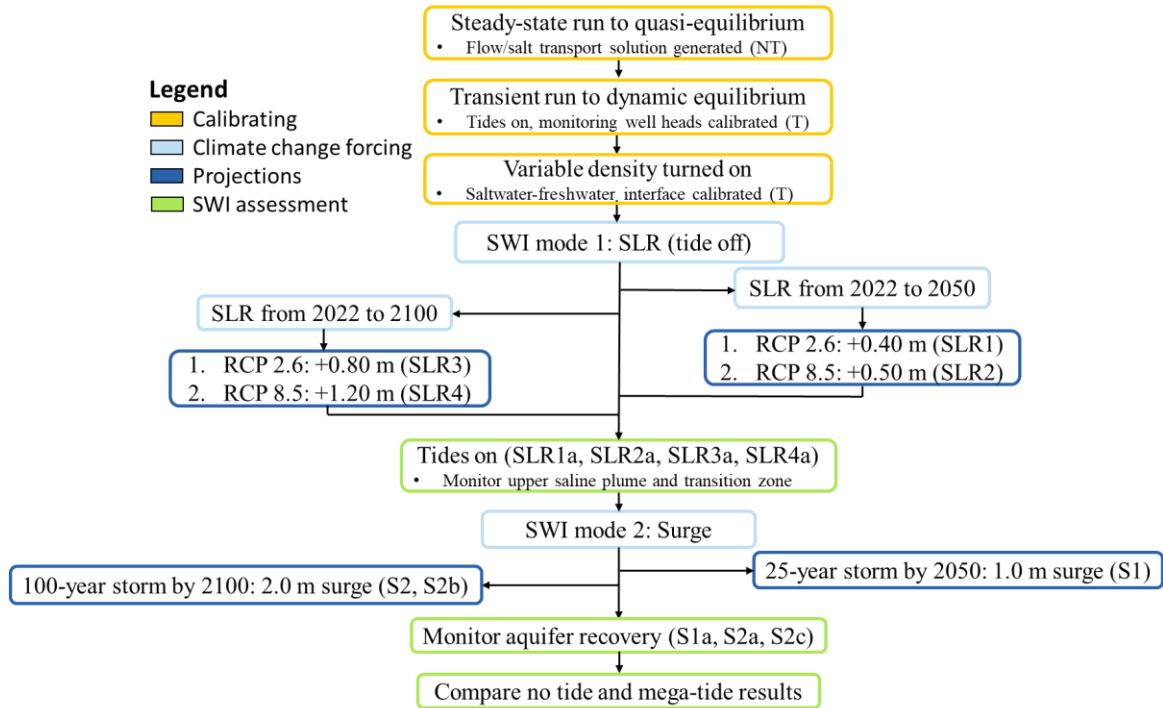
Figure 11. Flow chart showing the path and steps used to assess how tides and climate change influence saltwater intrusion (SWI). Results from climate models forced with two representative concentration pathways (RCP) were used for sea-level rise (SLR) projections. See Table 1 for model run identifications provided in parentheses.

To assess the first mode of saltwater intrusion, sea-level rise projections for 2050 and 2100 were imposed based on two representative concentration pathway (RCP) emission scenarios (both in the upper 95th percentile), RCP 2.6 and RCP 8.5, respectively (Figure 11). The sea-level rise rates for these scenarios were based on projections summarized in James et al. (2021). These are relative to the average conditions between 1986 and 2005 (James et al., 2021). However, given the limited knowledge about historic sea-level rise in Nova Scotia, this study assumes that the local sea-level rise between 2005 and 2020 was only a few centimeters as it was regionally (Lombardi, 2014), and therefore the sea-level rise projections are superimposed on present-day water levels. These simulations were used to monitor how the saltwater wedge location is influenced by sea-level rise as well as the impacts on the tidally influenced groundwater flow dynamics. The sea-level rise

projections for each year (2050 and 2100) and RCP scenario (2.6 and 8.5) were gradually applied at a constant rate over the 28 (*i.e.*, 2022 to 2050) and 78 (*i.e.*, 2022 to 2100) years with a mean tidal head boundary condition (*i.e.*, no amplitude) applied on the seaside boundary. Once the new final sea level was reached for each time and RCP scenario, the transient tidal boundary was turned back on to achieve dynamic equilibrium for each tidal condition (Figure 11). This approach was applied as a tractable way to simulate these complex, superimposed forcings.

To assess the second mode of saltwater intrusion, storm surge projections for 2050 and 2100 (Webster et al., 2012) were imposed on the 2050 and 2100 sea-level rise model results for the worst-case RCP 8.5 scenario during typical high tide conditions (Figure 11). These model simulations were used to temporarily increase regular high tide water levels and cause dyke overtopping and investigate how long it would take any infiltrated saltwater to flush out of the system and return the groundwater salinity to its original state. To assess how dyke breaching would influence saltwater intrusion and groundwater flow patterns, the worst case (RCP 8.5, 2100) sea-level rise and surge (2-meters on top of high tide) simulations were repeated with the dyke removed (Figure 11). The model results for both saltwater intrusion modes were compared for no-tide and mega-tidal conditions to assess the influence of tidal forcing on saltwater intrusion and groundwater flow dynamics (Figure 11). Table 1 lists the model simulations conducted with a short description of how these runs are different from each other.

Table 1. HydroGeoSphere (HGS) model simulations. Steady-state (SS) runs are used as initial conditions (IC) for transient simulations with density driven flow (DDF). Sea-level rise (SLR) and storm surge projections are imposed on the calibrated model. See Figure 11 for more details.

Model run ID	Description
NT	No tide - tidal boundary turned off, DDF off, saltwater-freshwater interface calibrated based on where it was NOT detected (*i.e.*, near the deep well or beneath the dyke based on geophysical surveys)
T	Tidal boundary and DDF turned on until dynamic equilibrium achieved
SLR1	SLR projection for 2050 RCP2.6: +0.40 m (~ +1.43 cm/yr applied to boundary) with no tide
SLR1a	Using SLR1 as IC, turning on the mega-tidal boundary
SLR2	SLR projection for 2050 RCP8.5: +0.50 m (~ +1.8 cm/yr applied to boundary) with no tide
SLR2a	Using SLR2 as IC, turning on the mega-tidal boundary
SLR3	SLR projection for 2100 RCP 2.6: +0.80 m (~ +1 cm/yr applied to boundary) with no tide
SLR3a	Using SLR3 as IC, turning on the mega-tidal boundary
SLR4	SLR projection for 2100 RCP 8.5: +1.20 m (~ +1.5 cm/yr applied to boundary) with no tide
SLR4a	Using SLR4 as IC, turning on the mega-tidal boundary
S1	Surge projection superimposed on SLR projection for a 25-yr return period storm by 2050: +1.0 m for 2 hours (using simulation SLR2a as IC) during high tide
S1a	Using results from S1 as IC, the boundary applied from SLR2a is used to run the simulation to assess flushing times
S2	Surge projection superimposed on SLR projection for a 100-yr return period storm by 2100: +2.0 m for 2 hours (using simulation SLR4a as IC) during high tide
S2a	Using results from S2, the boundary applied from SLR4a is used to run the simulation to assess flushing times
S2b	Surge projection superimposed on SLR projection for a 100-yr return period storm by 2100: +2.0 m for 2 hours (using simulation SLR4a as IC) during high tide with the dyke removed
S2c	Using results from S2b, the boundary applied from SLR4a is used to run the simulation to assess flushing times and dynamics without the dyke

3.3.4 Model parameterization

The objective of optimizing a numerical model is to replicate or closely resemble observations obtained from field methods so that the parameterized model can be

reasonably applied, at least in this case, to assess the impacts of theoretical future forcing. The parameters (Table 2) were selected based on default or typical values used in the literature, previous reports conducted in the area, and from model calibration as described later.

Table 2. Properties used in HydroGeoSphere (HGS) model simulations.

Parameters	Symbol	Value(s)			Units	Justification
General						
Freshwater density	ρ_f	1000			kg m^{-3}	
Saltwater density	p_s	1025			kg m^{-3}	Hiscock & Bense (2014)
Freshwater concentration	C_f	0			g L^{-1}	
Saltwater concentration	C_s	35			g L^{-1}	
Surface properties						
Surface friction, *x*-direction	n_x	0.02			m$^{-1/3}$ s	
Surface friction, *y*-direction	n_y	0.02			m$^{-1/3}$ s	
Obstruction storage height	H_o	0.0			m	Default HGS values in Therrien et al. (2010)
Rill storage height	h_{ds}	0.001			m	
Coupling length	l_{exch}	0.1			m	
Longitudinal hydraulic dispersivity	α_l	100.0			m	HGS saltwater intrusion modeling study by Guimond & Michael (2020)
Transverse hydraulic dispersivity	α_t	10.0			m	
Coupling dispersivity	α_{ld}	5.0			m	
Subsurface properties						
		Clay	**Sand**	**Bedrock**		
Hydraulic conductivity (*x*)	K_x	1E-05	4E-03	1E-04	ms^{-1}	Model calibration and validation (see section 3.2.2 and 4.2.1)
Hydraulic conductivity (*y*)	K_y	1E-05	4E-03	1E-04	ms^{-1}	
Hydraulic conductivity (*z*)	K_z	1E-06	4E-04	1E-05	ms^{-1}	
Specific storage (storativity)	S_s	(1E-4[1])	3E-3[1]	1E-6[1]	m^{-1} (-)	Model calibration[1]; Hennigar & Kennedy (2006)[2]
Porosity	n	0.5[2]	0.3[2]	0.05[2]	-	
Residual saturation	θ_r	0.053	0.053	0.053	m^3	
Inverse of air entry parameter	α	3.5	3.5	3.5	m^{-1}	Default values from Therrien et al. (2010)
Pore-size distribution index	β	3.2	3.2	3.2	-	
Pore connectivity	l_p	0.5	0.5	0.5	-	
Longitudinal hydraulic dispersivity	α_l	2.0	2.0	2.0	m	Gelhar (1992); Yang et al. (2016)
Transverse hydraulic dispersivity	α_t	0.2	0.2	0.1	m	
Tortuosity	τ	0.1	0.1	0.1	-	Therrien et al. (2010)
Bulk density	ρ_b	1200	1500	2000	kg m^{-3}	Agriculture Canada (1989)

CHAPTER 4: FIELD AND NUMERICAL MODELING RESULTS

4.1 Field method results

4.1.1 Climate data

The measured climate data and calculated potential evapotranspiration are shown in Figure 12. The calculated potential evapotranspiration (*PET*) was subtracted from the measured precipitation (*P*) for the four months for which data were collected to estimate recharge (*e.g.*, Pavlovskii et al., 2022). The daily *P-PET* values (when positive) during those four months were then extrapolated for a full year to estimate annual recharge. This yielded a recharge estimate of 740 mm/yr, which is an overestimation as other estimates for nearby areas are on the order of 100 mm/yr (*e.g.*, Rivard et al., 2012). While this approach has been successfully applied elsewhere (*e.g.*, Pavlovskii et al., 2022), the soil conditions at the site likely do not allow for rapid enough infiltration to assume that a positive *P-PET* value on a given day results in recharge of the same magnitude. Runoff, interception, throughflow, and delayed ET (shallow soil) are not accounted for in this simple method and ignoring them results in an exaggerated recharge at this site. Also, due to the short dataset collected, these data are not representative of a full year, and extrapolating them is likely unreasonable. Potential evapotranspiration rates are most likely smaller during the winter and spring months due to lower mean air temperatures, and less humidity; however, snowmelt would contribute additional water available for recharge. For all of the reasons, a recharge rate for the Wolfville area of 100 mm/yr from Hennigar & Kennedy (2006) was ultimately applied to the model.
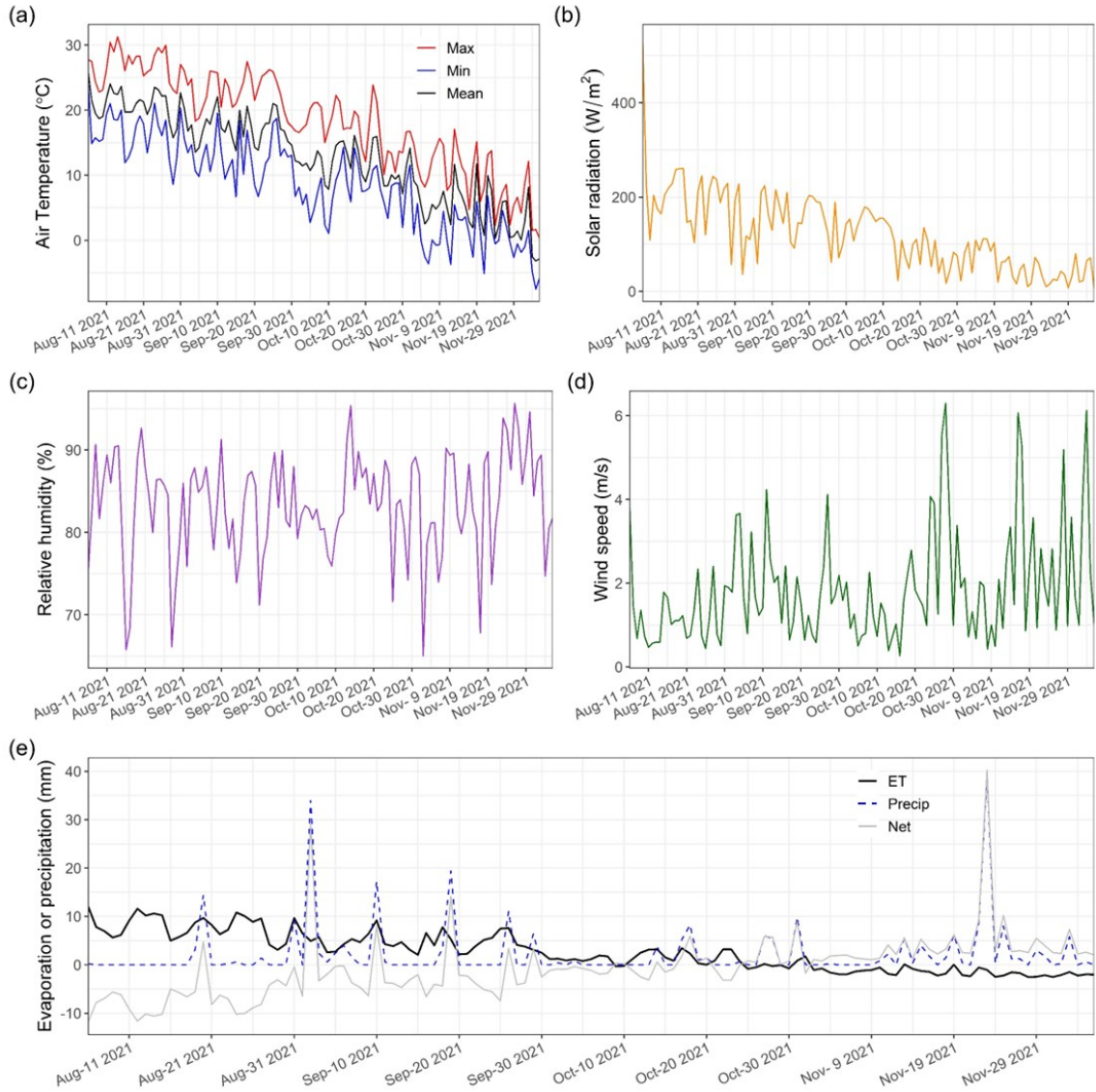
Figure 12. Climate data collected using the HOBO Onset RX3000 weather station set up in Wolfville. These panels show daily averaged or summed values for a) air temperature, b) solar radiation, c) relative humidity, d) wind speed, and e) precipitation/calculated potential evapotranspiration.

4.1.2 Water level and electrical conductivity

Tidal water level data were collected between October 11, 2020, and June 21, 2021, in the

Minas Basin (Figure 13). The tidal cycles are driven by a strong semi-diurnal (12.42 hr,

M2 constituent) tidal period which results in approximately two peaks and two troughs

every day. The peak tidal range is nearly 13.5 m which designates this region as having

mega-tidal conditions (*i.e.*, tidal range > 8 m). The tidal constituents are further described in section 3.1.2. These data represent the dominant forcing on the coastal groundwater dynamics in the Minas Basin. Very low-tide data in the Basin during spring tides may be missed due to the sensor being exposed to the atmosphere (*i.e.*, not submerged), which is why the tidal signals are flatter at the troughs than the crest during spring tides (Figure 13).
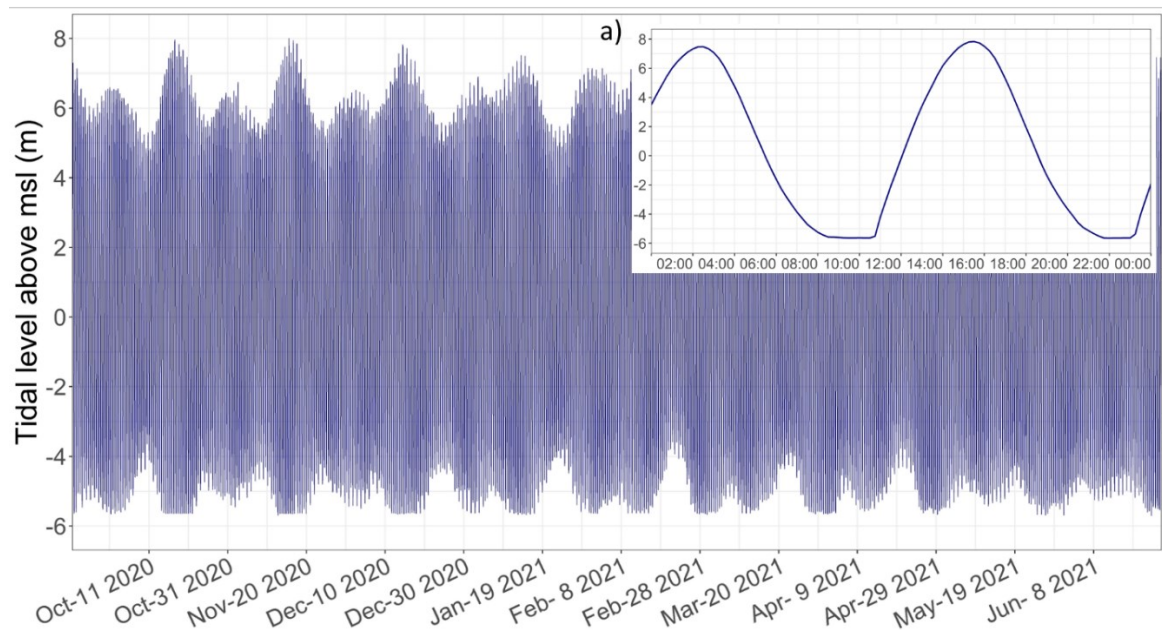
Figure 13. Tidal level data collected in the Minas Basin near Wolfville with inset a) showing a spring-neap cycle (October 18th, 2021). See Figure 8 for location of the tidal station.

Figure 14 shows the water level and conductivity data collected from piezometer/well nests at the edge of the coastline, in front of (salt marsh) and in behind the dykes. The water levels shown in Figure 14a and 14b fluctuate more due to tidal influences than the water level in the shallow piezometer in the sewage treatment plant (Figure 14c), as these piezometers are closer to the coastline (see Figure 8). Similarly, the water levels in nest 1 (Figure 14a) fluctuate more than the levels in nest 2 (Figure 14b), as nest 2 is further from

the coastline (see Eq. 6). Additionally, the tidal level inundates the land and infiltrates where these piezometers in nests 1 and 2 (Figure 14a and b) are drilled during spring high tides which explains why the water levels peak twice each month and slowly declines until the next spring tide. Lastly, the average conductivity reading from the piezometers in nest 1 (Figure 14a) and 2 (Figure 14b) ranges from 20,000 to 35,000 µS/cm which indicates saline water, whereas the average conductivity reading from the shallow piezometer in nest 3 (Figure 14c) is 1150 µS/cm indicating relatively fresh water. This expectedly indicates that the water is more saline at shallower depths when close to the coastline and fresher at approximately the same depth when further from the coastline. The clay glaciomarine overburden layer likely has a low hydraulic conductivity and high storage value, which explains why the tidal pressure and salinity do not propagate very far inland. At approximately 100 m from the coastline, the water level and conductivity in the clay layer are relatively constant as shown by the shallow readings in Figure 14c.

(a)

Legend: — Level (Shallow) — Conductivity (Shallow) — Level (Deep) — Conductivity (Deep)

(b)

(c)
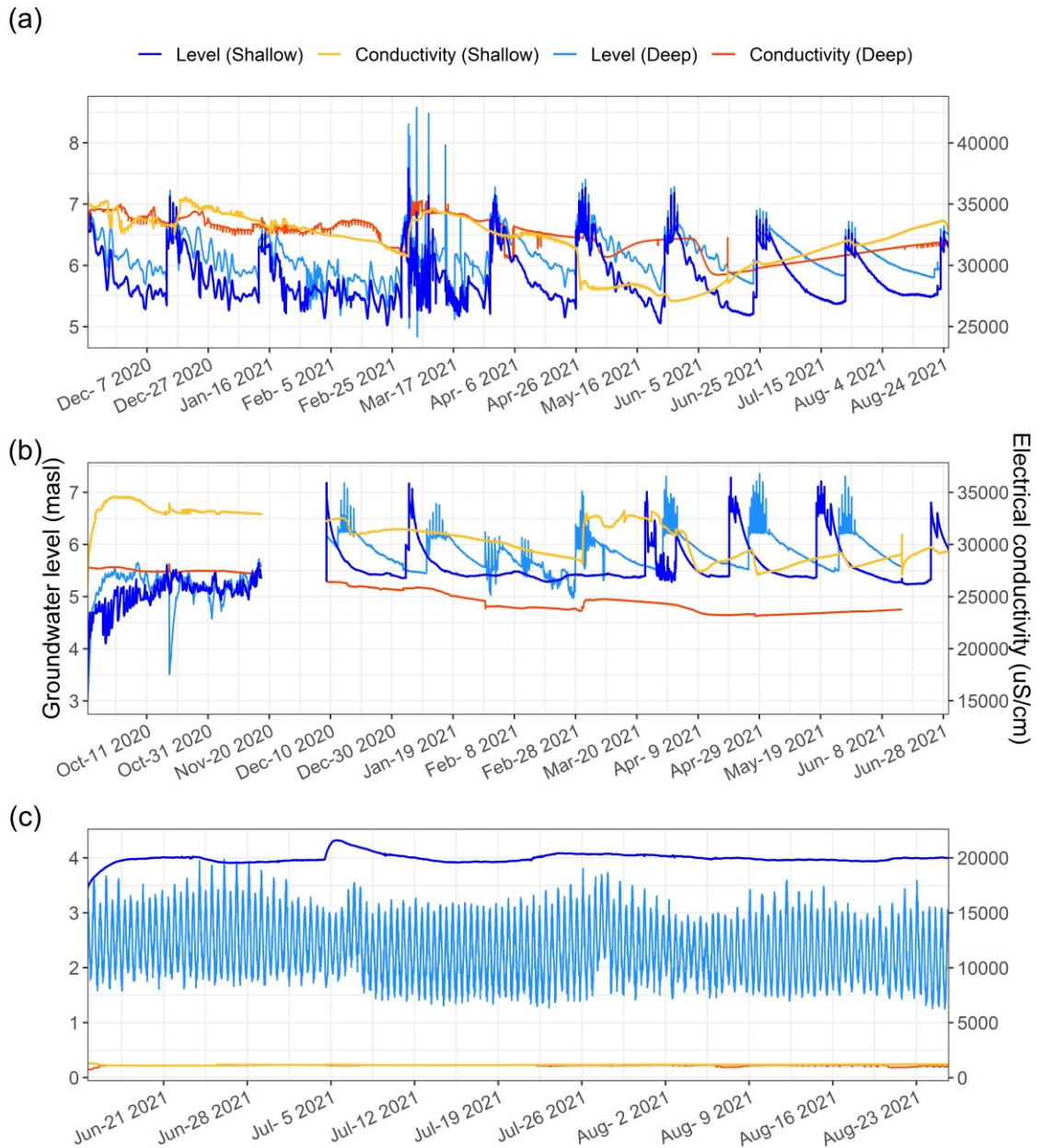
Figure 14. Water level and conductivity data shown for the a) piezometer nests at the coastline, b) in front of the dykes, and c) in behind the dykes (see Figure 9 for piezometer depths and Figure 8 for piezometer locations).

Figure 14c shows the water level and electrical conductivity time series for the shallow

piezometer and the deep groundwater well, both underlying the sewage treatment plant in

Wolfville. The shallow piezometer drilled within the shallow clay confining layer exhibits

no tidal signal propagation in the groundwater level. Conversely, the deeper groundwater well that is part of nest 3 penetrates the fractured sandstone bedrock layer, and the tidal groundwater signal is quite pronounced at this depth (Figure 14c). The upper and lower extremities of the tidal range in the deep groundwater well are approximately 1.0 and 4.0 masl, respectively, with a mean level of 2.5 masl. Also, the average conductivity of the water at this depth (~1150 µS/cm) indicates that the water is relatively fresh (but not potable) at this depth and distance inland. These data are critical as they indicate that the saltwater-freshwater interface does not penetrate in the subsurface as far as this deeper well, and thus provides a key assessment point for the numerical model. The tidal pressure signal penetrates further in the deeper aquifer system than the shallow system because the deeper aquifer is confined, meaning that for the same hydraulic conductivity value, the hydraulic diffusivity is higher because the storage is lower for confined (specific storage) vs. unconfined aquifers (specific yield).

4.1.3 Frequency domain analysis and hydraulic property estimation

Figure 15 shows the frequency domain analysis results and reveals the dominant constituents for the tide in the basin, the shallow groundwater levels, and the deep groundwater level, respectively. The tidal constituents that appear within these series include the lunar fortnightly (*Mf*, period of 327.86 hr), the principal lunar (*O1*, period of 25.82 hr), the luni-solar (*K1*, period of 23.93 hr), the larger lunar elliptic (*N2*, period of 12.66 hr), the principal lunar (*M2*, period of 12.42 hr), and the principal solar (*S2*, period of 12.00 hr). The amplitudes associated with the *M2* harmonic constituent frequency

(0.0817 hr^{-1}) were 5.41, 0.016, and 0.577 m for the basin (Figure 13), deep piezometer

(Figure 14a), and deep well (Figure 14c) series, respectively.
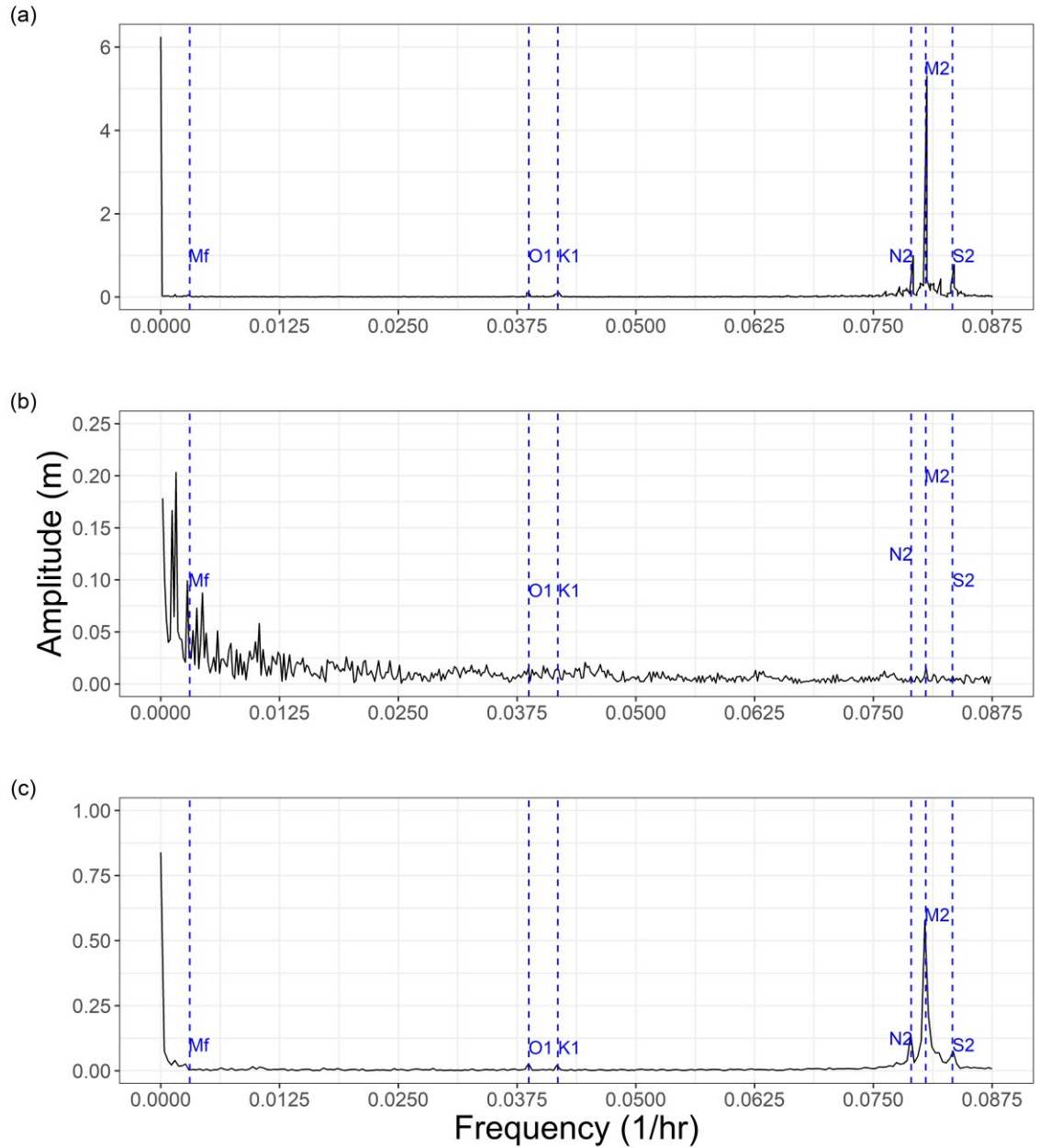
Figure 15. Results of the Fast Fourier Transform analysis. Dominant tidal constituents (i.e., Sa, Mf, O1, K1, N2, M2, and S2) are shown for the a) basin tide, b) deep piezometer (nest 1), and c) deep groundwater well (nest 3) series (see Figure 8 for sensor locations).

The tidal signal (dark blue) and groundwater level (light blue) from the deep town well (nest 3) for a two-day period are shown in Figure 16 for reference as this plot is where the lag time was obtained. The amplitudes used in this analysis were obtained from the FFT output shown in Figure 15. There is evidently damping between these signals; however, the lag time between peaks in the tidal series and groundwater series appears to be relatively short - approximately 15 minutes - which would indicate a high hydraulic conductivity and/or a fractured aquifer. However, it is possible that the lag is 24 hours plus 15 minutes which results in a much lower hydraulic conductivity value. Ultimately the simulated amplitudes (rather than lags) were compared to the observed basin and groundwater amplitudes for forcing and parameterizing the numerical model; lags can be harder to identify precisely in signal processing in hydrology (Irvine et al., 2017). It is important to note that the tidal pressure signal penetrates much further inland than the salinity signature (see low and stable electrical conductivity in Figure 16), as the former is a celerity phenomenon while the latter is driven by advection, dispersion, and density differences.
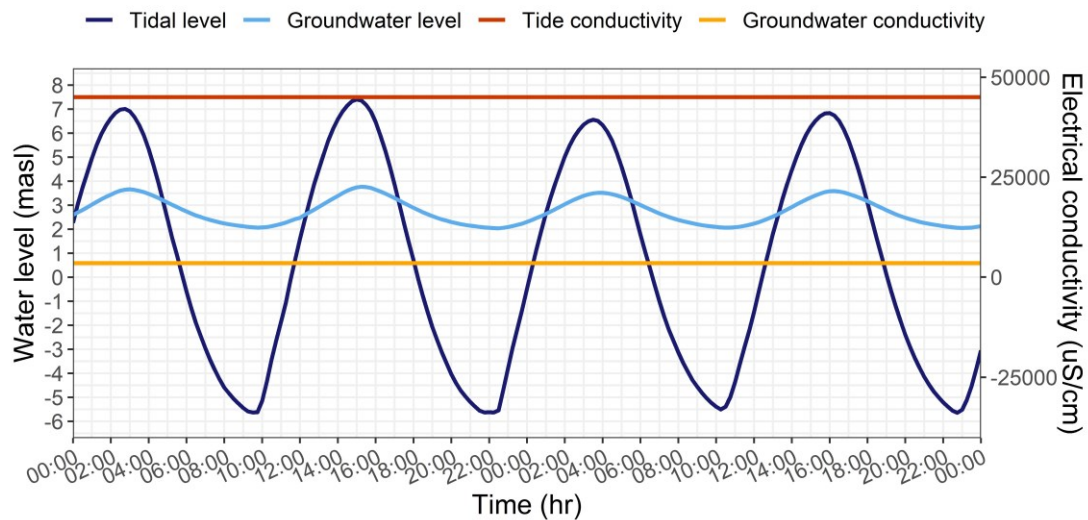
Figure 16. Tidal level (dark blue) and, tidal electrical conductivity (orange) in the Minas Basin and the groundwater level (light blue) and groundwater electrical conductivity (yellow) in the deep well over two days (November 18th and 19th, 2020).

4.1.4 Wave statistics

Data collected from the SoFar Spotter wave buoy are shown in Figure 17. The significant wave heights and associated frequencies (inverse of peak wave periods) are automatically calculated within the Spotter buoy internal software (Figure 17). The average wave height is within the 0 to 0.5 m range. However, the raw data showed larger wave heights (*e.g.*, maximum recorded height of 8 m, see inset) that are not realistic within the basin, especially in the shallow-water conditions of the deployment, and are postulated to be a result of tidal signal interference due to currents which are known to pose issues for Spotter buoys. The tidal currents and the length of the mooring cable required for the significant tidal range likely create noise in the wave observations. Thus, wave heights were filtered to exclude any value with a peak wave period greater than 11.4 s (inset in Figure 17), as long period wave heights with periods greater than 11.4 s were considered an anomaly in the dataset based on discussions with coastal scientists and engineers (*e.g.*, R. Mulligan, Queens University, pers. comm.). The average peak wave period recorded was 2.6 s (after filtering), meaning most waves measured within the basin are smaller, irregular waves. The waves within the basin are therefore primarily classified as ordinary gravity waves driven by wind forces (Munk, 1950). These data indicate that the Minas Basin is characterized by low-energy waves and that tidal dynamics are the dominant forcing. The average significant wave height of the top 1% of wave heights was only 0.13 m. Given these data, for the modeling component of this project, waves were not applied on the marine boundary conditions. Rather the overtopping model scenarios relied on storm surge projections as described previously.
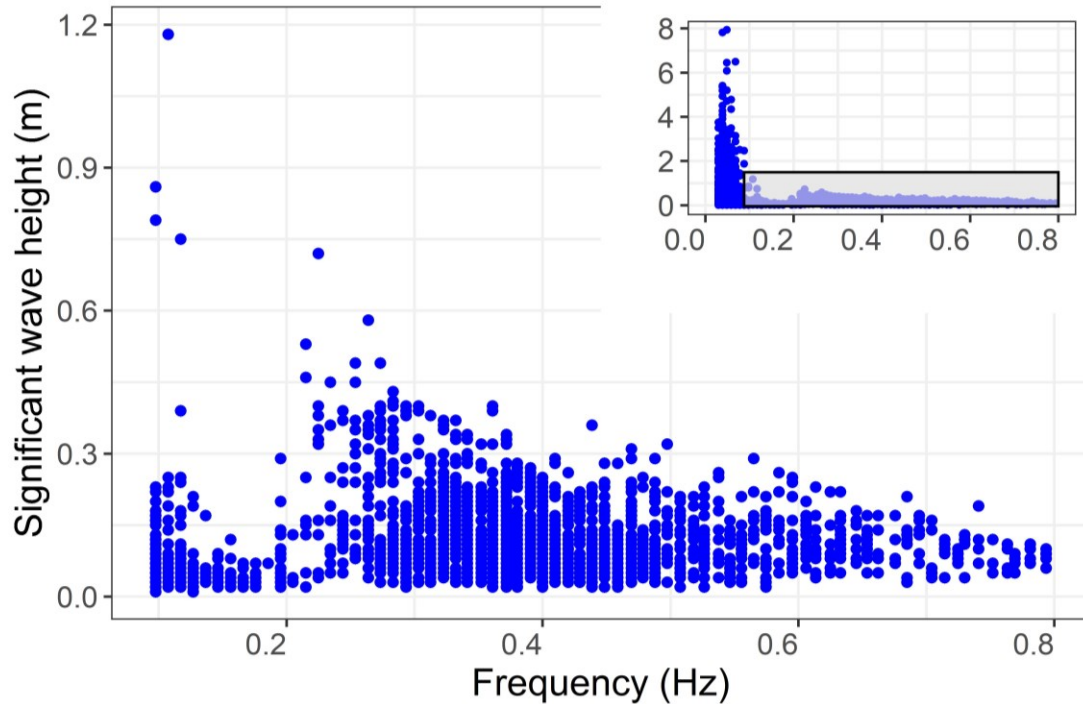
Figure 17. Significant wave heights and associated frequencies (inverse of peak wave periods) collected using a SoFar Spotter wave buoy in the Minas Basin. Inset shows raw significant wave heights before filtering. High waves occurred at low frequencies (high periods).

4.1.5 Geophysical mapping

Time-lapse, single location electrical resistivity data were collected with the WalkTEM on the seaward side of the dyke (Figure 18) from mid to high tide approximately every hour on June 25th, 2021. The first time-step point (t = 9:15 am) shows the highest resistivity profile, as this point was taken at low tide when groundwater flow is primarily seaward and therefore there is less salinity (lower electrical conductivity and higher resistivity) in the aquifer system. As the tide comes up (flood tide), the resistivity decreases with each time step during the flood tide as more saline water infiltrates the subsurface, thereby increasing the electrical conductivity (Figure 18a). These data suggest that there is a high hydraulic diffusivity zone with depth as the resistivity changes by an order of magnitude within just four hours, indicating pronounced saltwater-freshwater mixing in the subsurface.
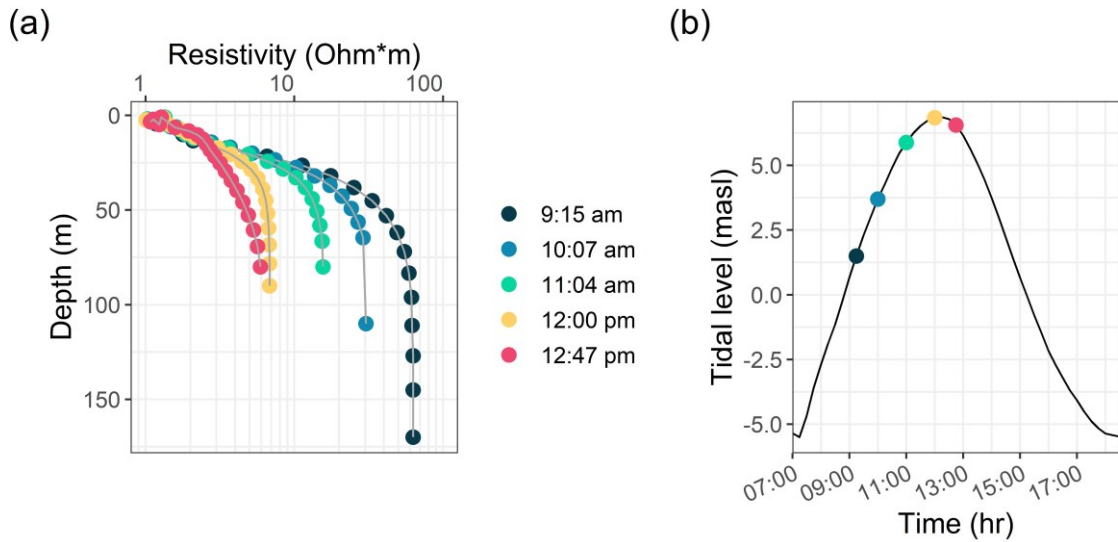
Figure 18. a) Resistivity point data collected approximately every hour during a flood tide and b) corresponding tidal stage (colours correspond in (a) and (b)). Data points were collected in front of the dyke using the ABEM WalkTEM geophysical tool. See Figure 8 for measurement location.

Figure 19 shows a two-dimensional transect of resistivity that was collected using the ABEM WalkTEM between the town of Wolfville and the Minas Basin (transect shown in Figure 8). These data show the porewater resistivities that were based on calculations using Eq. [13] (Archie, 1942). Starting from the top of the transect (*i.e.*, 6 to 10 masl), the higher resistivity values are indicative of freshwater saturated clay, unsaturated surficial materials, and vegetation with resistivity values greater than or equal to 25 Ωm. This layer is primarily where agricultural crops are grown in behind the dyke. Below this freshwater zone appears to be a more saltwater-saturated clay layer (*i.e.*, -4 to 6 masl) with resistivity values ranging from 2 to 4 Ωm. Lastly, at the bottom of the transect, the Wolfville formation looks to be freshwater saturated (*i.e.*, 4 to 25 mbsl) with resistivity values between 5 and 25 Ωm.

This resistivity profile does not align the standard paradigm of unconfined saltwater wedge characteristics (Jiao & Post, 2019), and this is because the aquifer is confined with substantial submarine groundwater discharge and does not follow the classic Ghyben-

Hertzberg principles (section 1.3). Due to the confined conditions, the bedrock aquifer is pressurized, and this pressure prevents saltwater from migrating landward into the subsurface. Additionally, there is likely a large mixing zone below 25 mbsl based on the results presented in Figure 19, where porewaters range between freshwater and saltwater (*i.e.*, brackish water) but are likely constantly changing given the tidal influence. These results suggest that there is an upper saline plume present, beneath the dyke system, which fluctuates with the tidal cycles. The saltwater wedge is not captured in this figure as this transect does not extend deep enough in the subsurface or far enough into the basin. Due to the complexity of the stratigraphy, this interpretation of the porewater salinity distribution is, at best, an educated guess that is not reliable enough to use as a baseline for the development of the numerical model. It is useful however in showing an upper saline plume as well as the general lack of a landward salt wedge at depth, which is also supported by the low electrical conductivity data from the deep well. This was a critical consideration during model calibration described later.
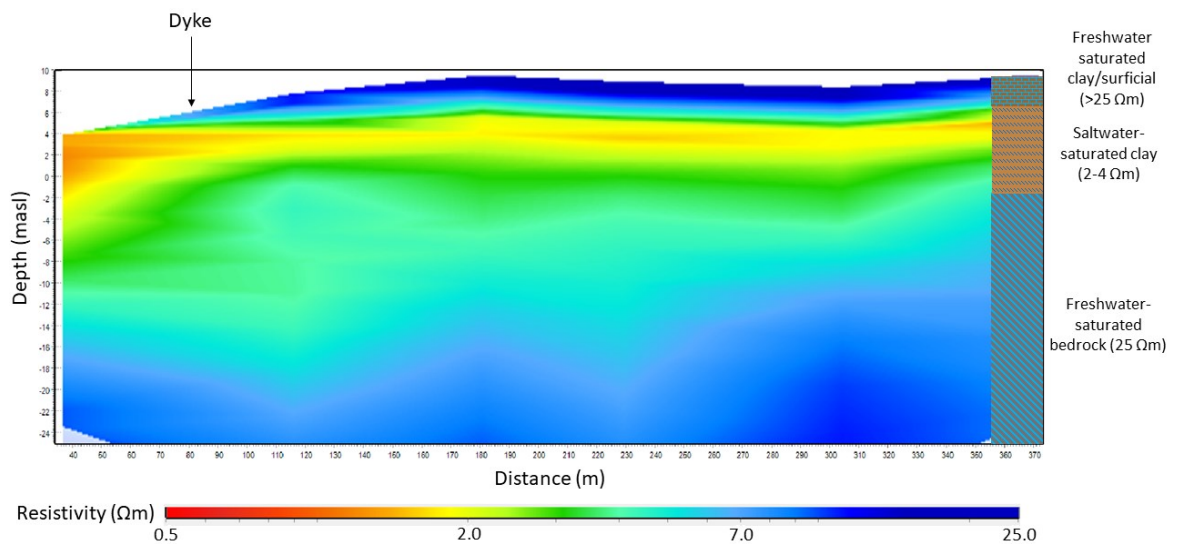
Figure 19. Resistivity profile plotted using data collected from the ABEM WalkTEM. The seaward and landward sides are shown on the right and left, respectively. The relative location of the dyke is shown for reference. Figure 8 indicates the location of the WalkTEM stations.

4.2 Numerical model results

4.2.1 Calibration

The key calibration points used to accurately develop this model included the deep well in nest 3 (Figure 14c), and the time-domain geophysical surveys (Figure 18 and Figure 19). In particular, the low electrical conductivity in the deep well imposed a limit on the landward extent of the saltwater wedge at that depth (70 meters). The simulated and observed dynamic heads (Figure 20) at the location of the deep well (Figure 14c) were used to calibrate the hydraulic conductivity and storage of the confining and water-bearing units in the model (Table 2). Figure 20 shows the HydroGeoSphere calibration results.
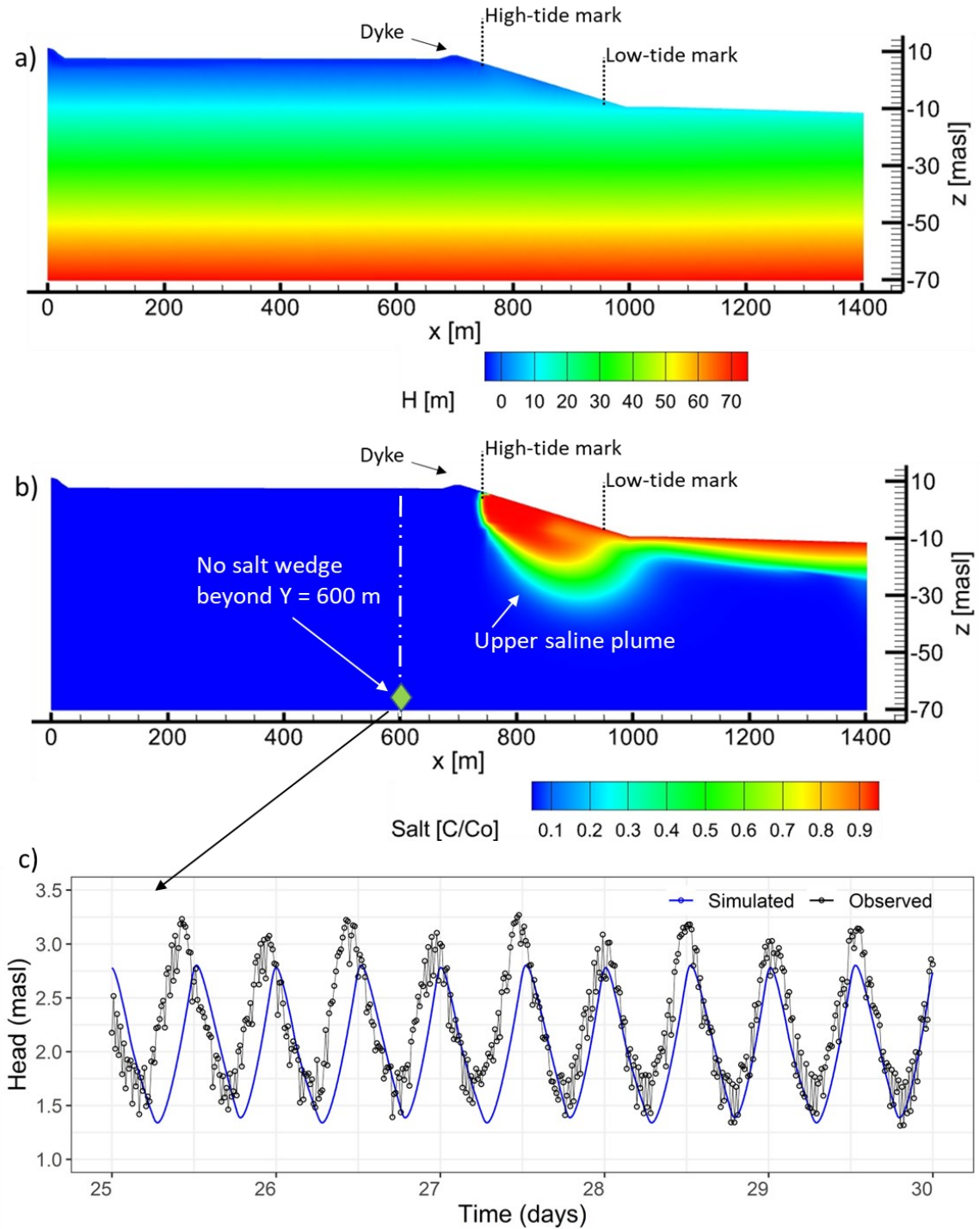
Figure 20. HydroGeoSphere calibration results. a) Pressure head distribution, b) salt concentration (normalized to seawater concentration) distribution and wedge location limit based on electrical conductivity of monitoring well, and c) head comparison between the modeled and measured water levels (nest 3, green diamond from b).

The electrical conductivity from this deep monitoring well (Figure 14c) showed that the type of water at this location is much closer to freshwater and thus the saltwater wedge in the model should not extend inland beyond $x = 600$ meters (Figure 20b).

The deep tidal groundwater levels (Figure 20c) are a key calibration point for head levels in the deeper aquifer which were used to fine tune the hydraulic conductivity value. The simulated head trends at this observation well location generally match the observed heads (Figure 20c). For example, the mean tidal amplitude for the model was 2.1 meters above seal level, while the mean tidal amplitudes in the measured data was 2.4 meters above sea level. However, the fit between the modeled and measured series is not exact (particularly during spring tides) due to the fact that the tidal boundary condition in the model was a simplified repeating periodic (semi-diurnal) version of the true tidal series that had multiple tidal constituents and associated frequencies. As the two series were not expected to overlap perfectly, the comparison focused on the amplitude and mean of the two series.

The shallower piezometer levels from nests 1 and 2 (Figure 14a and b) were not compared to the simulated levels in the model because the saltmarsh zone in front of the dyke (where these piezometers were installed, Figure 8) was not explicitly considered in the model domain since the deeper groundwater flow dynamics and soil salinization behind the dykes were of primary interest for the modeling study.

4.2.2 Mass and water balance errors

The mass and water balance error plots from the model calibration can be found in the Appendix (Figure A1). The errors were low for both mass and water when the model was

run with a steady-state boundary. The errors for the water balance increased when the model was run with a transient boundary, with an average error of 6.2%. These errors are automatically calculated based on each timestep which varies due to the adaptive time stepping mechanism HGS uses, and this can create large errors for very small timesteps, for example, at the peaks or troughs of tides. As a result, there are spikes in the water balance error (Figure A1). However, there is no corresponding error in the mass (solute) balance, suggesting these short spikes in water balance errors did not play a major role in influencing the simulation results.

4.2.3 Hydraulic head and salinity dynamics within a tidal signal

The hydraulic head and relative salt concentrations for the calibrated HydroGeoSphere model which served as initial conditions for climate change simulations are shown for multiple time periods within a tidal cycle (Figure 21). The hydraulic head fluctuates with the tidal cycle; the tide starts at the mean height (Figure 21a, $t = 0$ hr) and decreases down to low tide where the hydraulic head simultaneously lowers (Figure 21a, $t = 4$ hr). As the tide rises to high tide, the hydraulic head increases (Figure 21a, $t = 12$ hr). Changes to the salt distribution over the tidal cycle are less evident, as the total change in freshwater volume between high and low tide is a 0.04% decline (Figure 21b). While salinity changes in the upper saline plume are not observed between tidal cycles, the tides maintain the upper saline plume due to the tidal pumping, circulation, and density effects. It is important to acknowledge that the intra-tidal salinity dynamics in the model appear to be muted in comparison to the resistivity dynamics from the time-lapse WalkTEM measurements

(Figure 18). This is likely due in part to the region in the model not being as confined as it
is in reality and the resultant overestimation of storativity in the model.
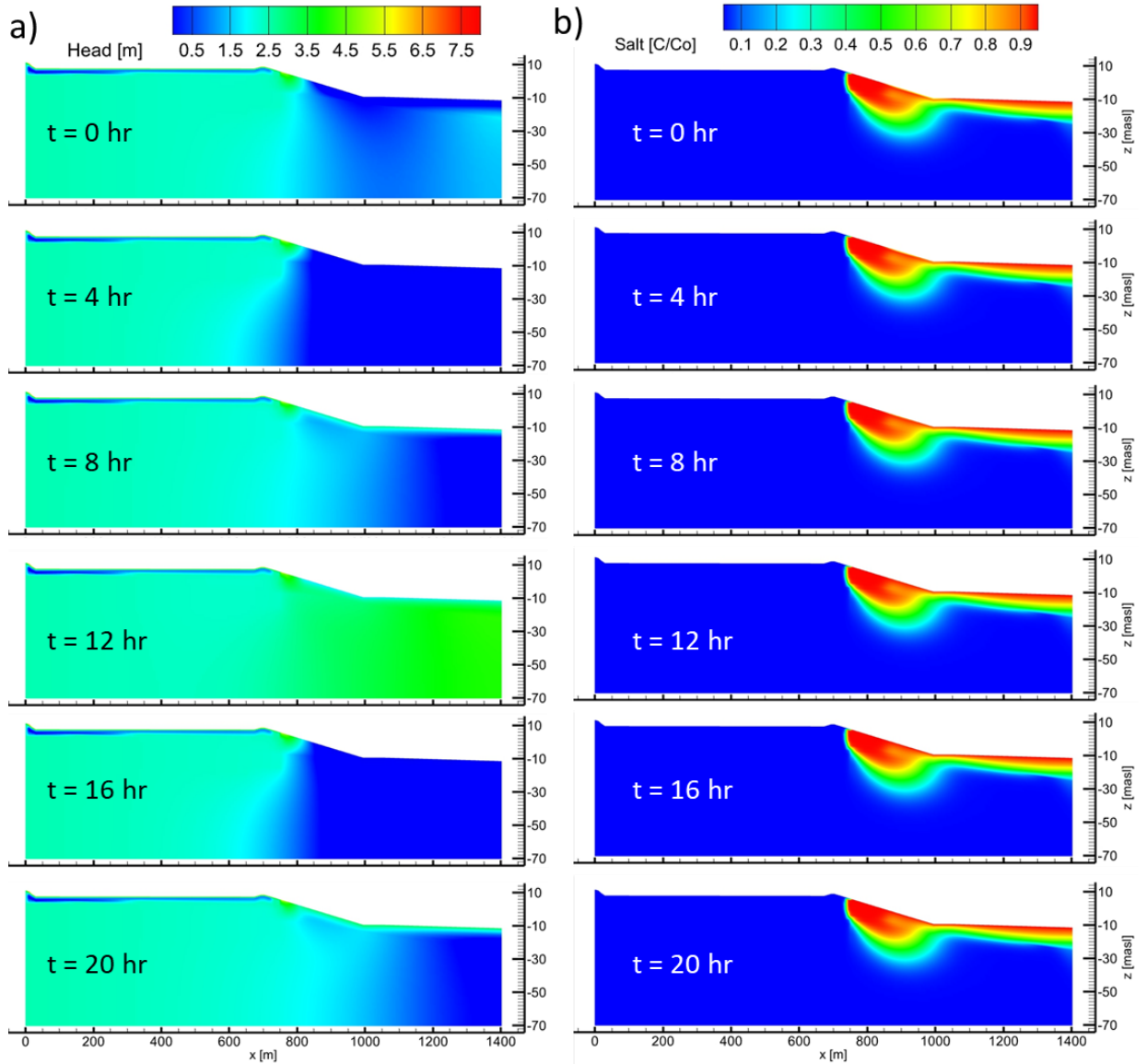
Figure 21. a) Hydraulic head and b) relative salt concentration dynamics over a tidal cycle.

4.2.4 Saltwater intrusion mode 1: SLR

The salt distribution heat maps for the sea-level rise scenarios discussed in Table 1 are shown in Figure 22. These simulations were run using a mean (*i.e.*, no tide) sea level boundary that gradually increased between 2022 and 2050 (Figure 22a and b), and 2022 and 2100 (Figure 22c and d), at a rate in accordance with the SLR projections for the representative concentration pathways (RCP) 2.6 (Figure 22a and c) and 8.5 (Figure 22b and d), respectively (see Table 1). Figure 22e-h shows the salt distribution for the same sea-level rise scenarios in Figure 22a-d, but with the mega-tidal seaside boundary turned on once the SLR was complete. The vertical axis (*z*) is exaggerated to visualize the differences between SLR scenarios and the impacts to the upper saline plume, which creates the appearance of vertical dispersion.
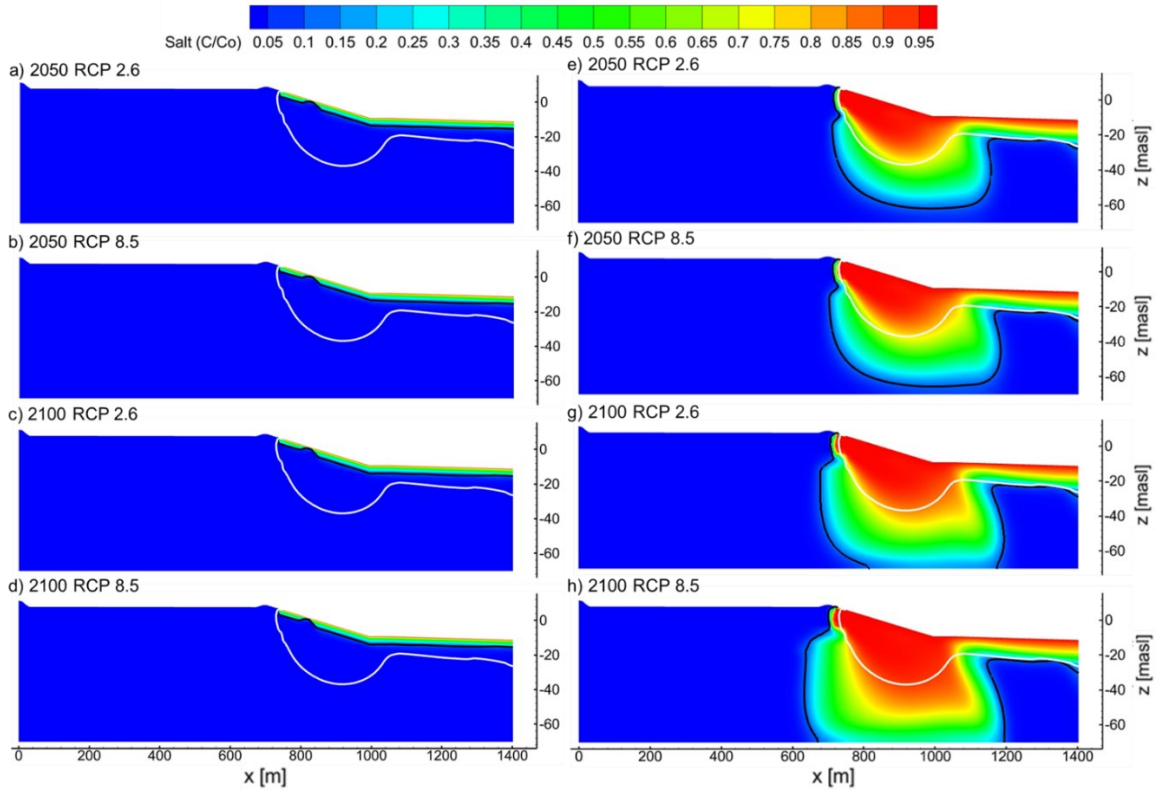
Figure 22. Results (normalized salt concentrations) of sea-level rise (SLR) projections for relative concentration pathways (RCP) 2.6 and 8.5 for the years 2050 and 2100. The left column of results represents the SLR results without tides applied, while the corresponding post-SLR results with tides imposed are presented in the right column (after two years of the tide being re-imposed, shown at mean tide). White isocontour lines represent the initial 1% concentration line with a 2020 sea level and tides applied, while the black isocontour lines represent the new 1% concentration line.

The results shown in Figure 22 indicate that sea-level rise will drive an increase in the vertical and horizontal extent of the upper saline plume. The plume extended downward by 25, 28, >33, and >33 meters, and horizontally (landward and seaward) by 145, 185, 225, and 285 meters, for SLR1a, SLR2a, SLR3a, and SLR4a, respectively, after approximately two years of simulation with tides re-imposed. For SLR3a and SLR4a, the 1% contour line extends downward outside of the domain. Mega-tidal conditions expectedly increase the dispersion of salt in the upper saline plume (Figure 22e to h) compared to the simulations without a tidal oscillation in the seaward boundary (Figure 22a to d). The Appendix contains a heat map distribution showing the Peclet number in the *x* and *z* directions,

suggesting that numerical dispersion is not occurring in the area where the upper saline plume is located, as the Peclect number is less than six in this zone, where six is the upper limit of the threshold for dispersion (Aquanty, 2015b) (Figure A2). However, it is possible some numerical dispersion may be contributing to the plume spreading during tidal peaks and troughs. It is also worth noting that if the sea level were to remain stable (e.g., at an elevated state), the plume may eventually return to a similar morphology (but shifted inland) as before (e.g., Figure 21) as equilibrium was never achieved due to high simulation times. For all SLR scenarios, the upper saline plume shifts from stable to unstable, meaning the original 'U shape' of the plume became irregular, likely due to the higher-pressure signal being applied that has not yet had enough time to equilibrate. As an example, the worst-case SLR4 scenario was run for almost 300 years without the tides and still did not reach equilibrium (Figure A3). During this simulation, the upper saline plume disappeared, and a saltwater wedge formed and continued moving inland after nearly 300 years post-SLR, likely due to the higher mean sea level relative to the inland freshwater head boundary.

The total freshwater in the modeling domain was computed internally in the model at the end of each time step with output to assess model stability as well as saltwater intrusion dynamics. Herein, freshwater is defined as any water with a normalized (to seawater) solute concentration less than or equal to 0.029 (*i.e.*, fraction converted from saline concentration scale, less than 35^{-1} is fresh), and saltwater is defined as any water with a relative solute concentration greater than 0.5, where 1.0 is saline water and 0.0 is fresh water. The SLR simulations did not stabilize within three years once the mega-tidal boundary was turned on (Figure 22e to h). The freshwater volume for each scenario continued to decrease over

time (Figure 23) as the salt plume dispersed due to tidal pumping. SLR resulted in a 25.4, 26.7, 29.1, and 32.0% decline in freshwater volume, for SLR1a, SLR2a, SLR3a, and SLR4a, respectively, after just ~ 2 years post-SLR (with the tides re-imposed). The salt plumes that developed because of the SLR3a and SLR4a scenarios could eventually result in salinization of the pumping well located at $x = 600$ meters, $z = -70$ meters, as the well is only 215 and 140 meters (horizontally) away from the 1% isocontour lines, respectively, after only 2 years of the mega-tidal conditions imposed after sea-level rise was simulated. If the well were pumped, it would draw the water level down, potentially triggering active or passive saltwater intrusion towards the well.
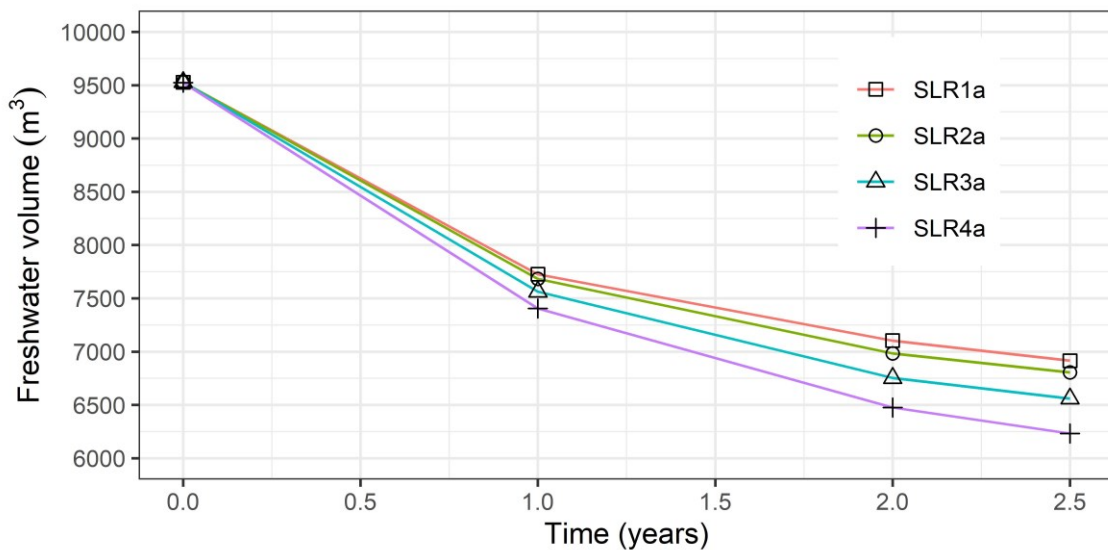
Figure 23. Freshwater volume in the model over time after sea-level rise (SLR) for each scenario with mega-tides re-imposed. Linear interpolation assumed between points.

4.2.5 Saltwater intrusion mode 2: surge

The salt distribution heat maps for the surge scenarios discussed in Table 1 are shown in Figure 24. These simulations were run using a high tide + surge boundary (+1 m for 2050,

+2 m for 2100) that lasted for 2 hours, and then returned to the regular mega-tidal oscillation. Immediately after the 1-meter surge in the S1a scenario (Figure 24a, $t = 24$ hours), there is almost no difference between the initial and new 1% isocontour lines around the upper saline plume. However, the upper saline plume begins to change within months of the surge occurring due to the new higher water level mark (Figure 24a, $t = 6$ months). After two years post-surge, the upper saline plume is unstable and still dispersing (Figure 24a, $t = 2$ years), as the water level rose faster than it could equilibrate. The 2-meter surge in the S2a scenario resulted in dyke overtopping (Figure 24b, $t = 24$ hours) and shallow salinization of the agricultural land behind the dyke. By six months, the flooded saline water behind the dyke infiltrated approximately 5 meters below the ground surface (measured to the 1% isocontour), with salt fingers developing on the landward side of the domain (*e.g.*, between $x = 0$ and 200 m) after two years (Figure 24b, $t = 2$ years). The 2-meter surge for the S2c scenario resulted in a higher concentration of saline water infiltrating behind the dyke (Figure 24c, $t = 24$ hours). By two years, the upper saline plume extended to the bottom of the domain and became unstable. However, even with this worst-case scenario simulation, the plume only migrates seaward, not landward as the freshwater discharge from the confined aquifer continues to resist the intrusion of this saline plume. As for the sea-level rise scenarios, this plume growth due to short hydraulic perturbation (surge) may be due to numerical issues, although the Peclet number is reasonable (Figure A5).

To investigate the influence of tidal pumping on aquifer flushing rates, the same three simulations (S1, S2, S2b, Table 1) were also run post-surge without the tidal boundary imposed, but rather just the mean tide level (Figure 25) and compared to the scenarios with

the tides imposed. In all three scenarios (without tides), the upper saline plume size expectedly decreased over time given the lack of tidal mixing (*e.g.*, Figure 25a, from $t = 24$ hours to $t = 4$ years). Ponding of saline water on the agricultural land occurred after the S2 and S2b surges (Figure 25b and c). Unlike the results with tides, salt fingers did not develop post-surge for the S2 scenario without tides (Figure 24b vs. Figure 25b). This may be because during low tides, the head difference between the inland boundary and the tidal boundary is higher, allowing for more seaward discharge to occur (Figure 24b, $t = 4$ years).

The salt fingers started to develop six months post-surge for the S2a scenario (Figure 26a) and 4 years post-surge for the S2c scenario (Figure 26b). The concentration of saltwater on the landward side of the dyke is 190% greater for the S2c scenario (without the dyke) compared to the S2a scenario (with the dyke) six months post-surge (Figure 26a and b, $t = 6$ months). By three years, the salt fingers have reached upwards of 15 meters below the ground surface for the S2a scenario (Figure 26a, $t = 3$ years, and have not yet developed for the S2c scenario (Figure 26b, $t = 3$ years). In the S2c results, the saline water has infiltrated up to 3 meters below ground on the landside of the domain ($x = 30$ m), and up to 3.3 meters on the dyke side ($x = 620$ m) after 6 months, and respectively 4 meters and 4.3 meters after 3 years (Figure 26b, $t = 6$ months, $t = 3$ years). By 4 years, salt fingers have started to develop behind the dyke for the S2c scenario (Figure 26b, $t = 4$ years). The dyke forces water to pool behind the dyke, and this ponded water infiltrates more quickly due to the greater vertical hydraulic gradient (Figure 26a, $t = 4$ years). In contrast, the scenario without the dyke does not have that coastal barrier retaining water on the landward side (Figure 26b, $t = 4$ years).

When removing the tidal influence post-surge (Figure 27), salt fingers did not develop within the same amount of time as the post-surge simulations with tides (Figure 26). However, a higher saltwater concentration infiltrated in the 'no tide' post-surge simulation with the dyke compared to the same simulation but with tides (~0.2 relative salt concentration, Figure 26a vs. ~0.5 relative salt concentration, Figure 27a,). This is because, without the tides, the simulated shallow saline plume sourced from inundated seawater migrates uniformly down (similar to a uniform 'wetting front'), whereas, with the tides, the plume is more dispersed via salt fingers.
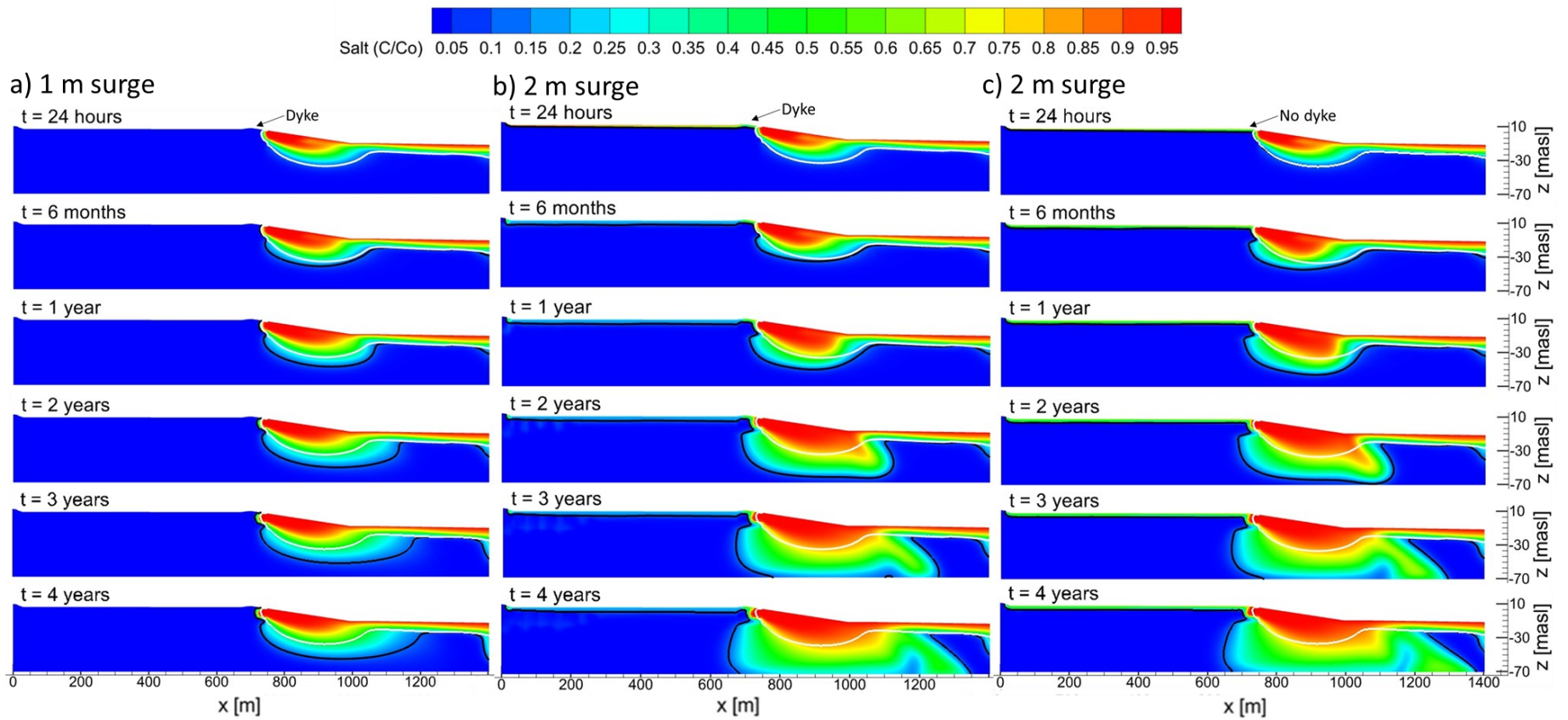
Figure 24. Salt distribution results from storm surge projections with tides for the a) 1 m surge, b) 2 m surge, and c) 2 m surge with the dyke removed. Each panel (top to bottom) represents a point in time after the surge has occurred. White line indicates the initial 1% contour location based on present-day conditions. Black line indicates the new 1% contour. These simulations were run using a mega-tidal seaside boundary post-surge. Results outputted at mid-tide stage.
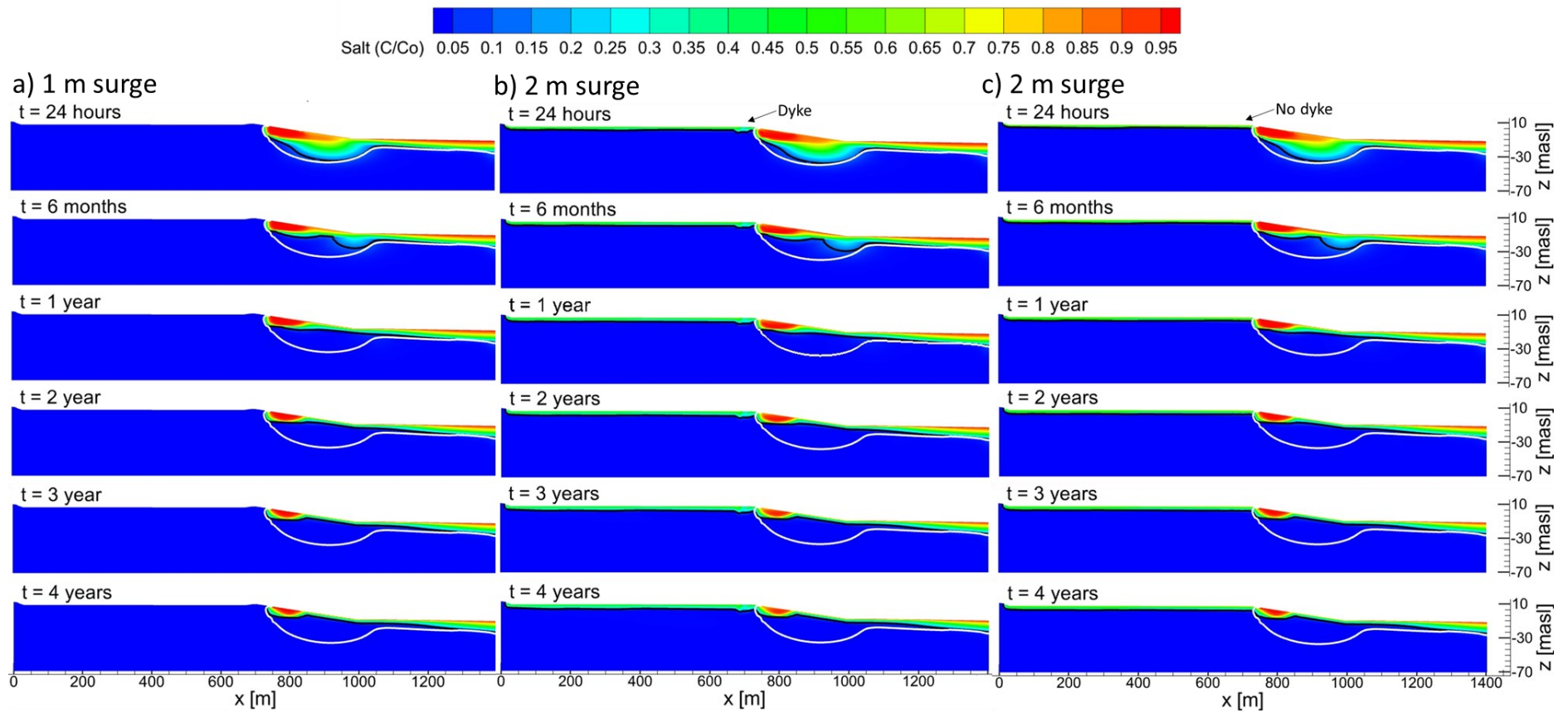
Figure 25. Salt distribution results from storm surge projections without tides for the a) 1 m surge, b) 2 m surge, and c) 2 m surge with the dyke removed, and without tides imposed. Each panel (top to bottom) represents a point in time after the surge has occurred. White line indicates the initial 1% contour location based on present-day conditions. Black line indicates the new 1% contour. These simulations were run using a mega-tidal seaside boundary post-surge. Results outputted at mid-tide stage.
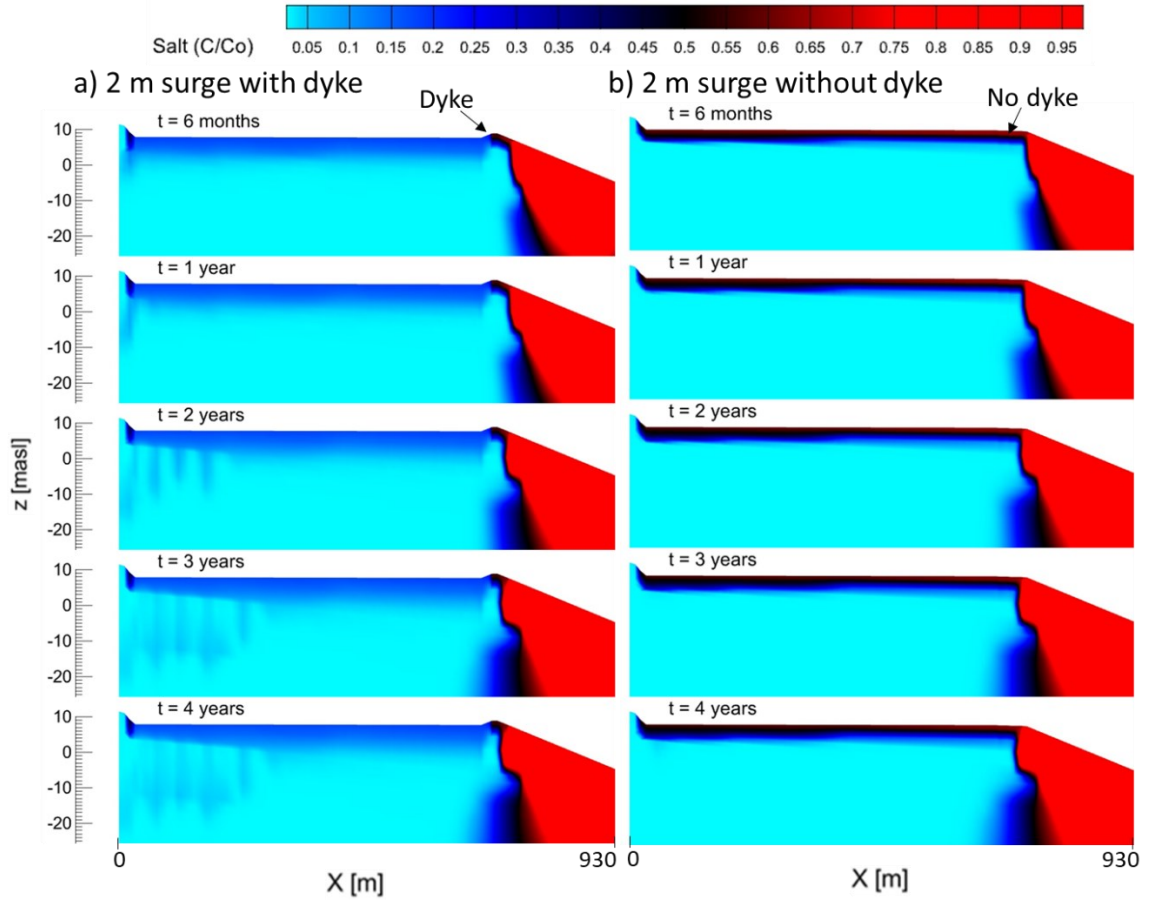
Figure 26. Zoomed in salt distribution results from storm surge projections with tides for a) 2 m surge (S2a), and b) 2 m surge with the dyke removed (S2c). Each panel (top to bottom) represents the indicated point in time after the surge has occurred. Panels are zoomed in behind the dyke, and the salinity colour distribution is altered from previous figures to help visualize salt finger development over time. Results outputted at mid-tide stage.
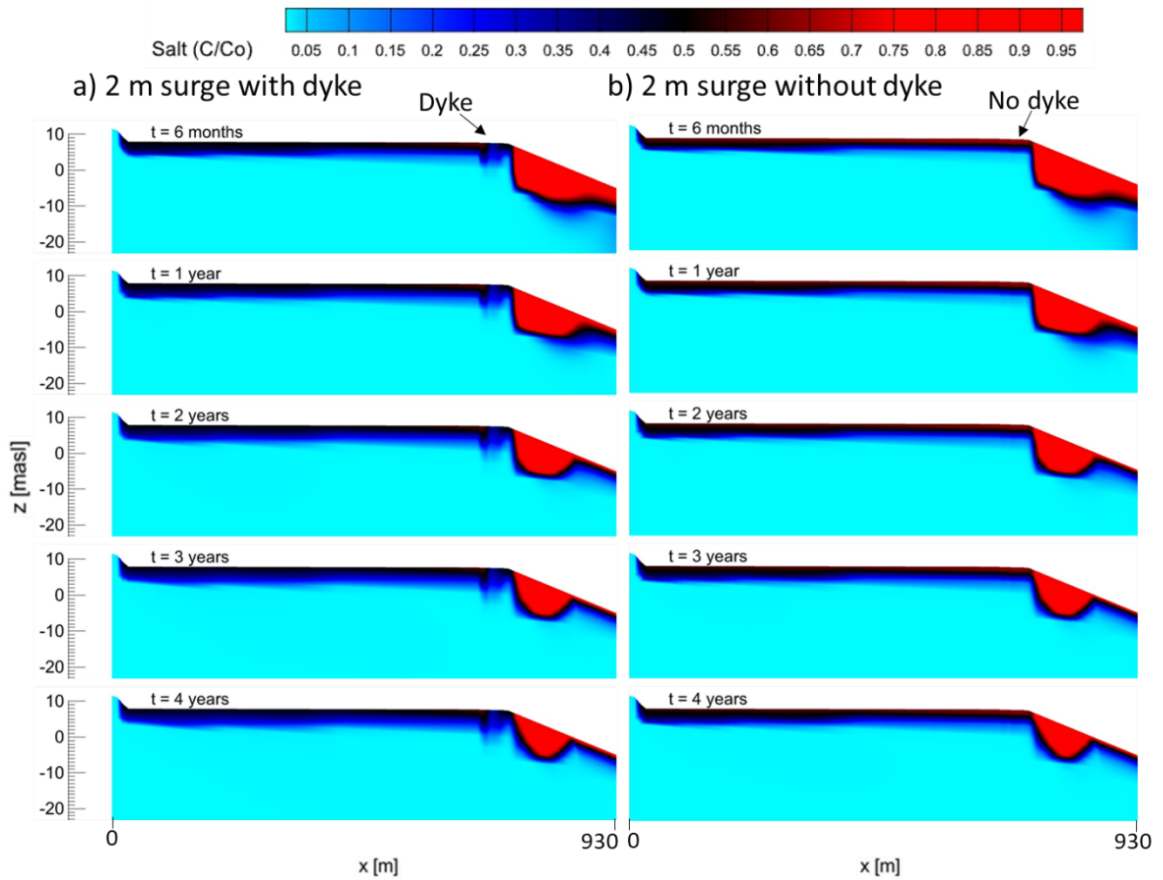
Figure 27. Zoomed in salt distribution results from storm surge projections without tides for a) 2 m surge (S2a), and b) 2 m surge with the dyke removed (S2c). Each panel (top to bottom) represents the indicated point in time after the surge has occurred. Panels are zoomed in behind the dyke and the salinity colour distribution is altered from previous figures to help visualize salt finger development over time. Results outputted at mid-tide stage.
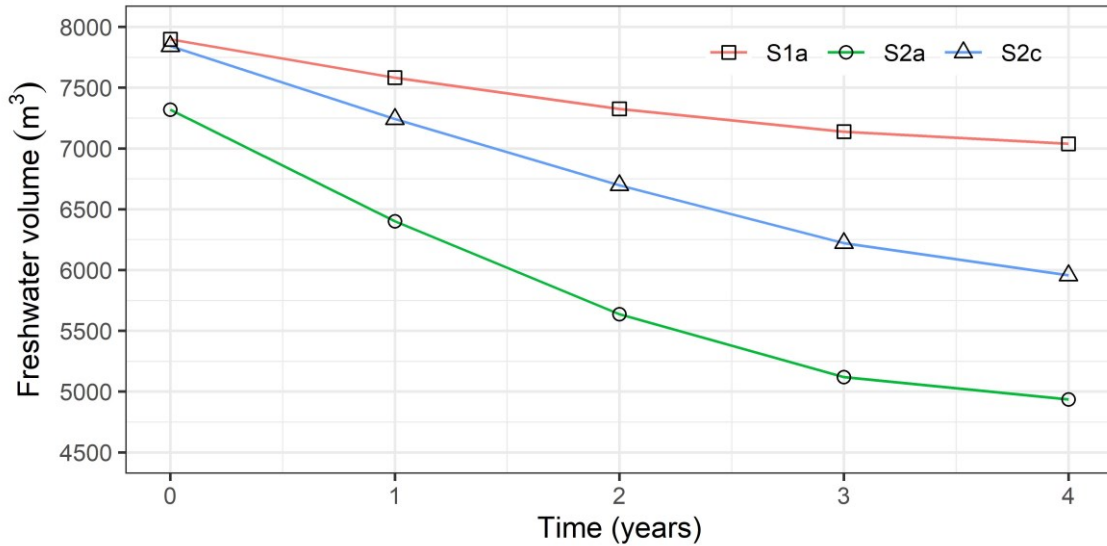
Figure 28. Freshwater volume over time post-surge for each scenario with mega-tides. Linear interpolation assumed between points.

4.2.6 Freshwater, brackish water, and saltwater volumes

Freshwater and saltwater volumes were calculated for the end of each modeling simulation

(Figure 29). The relative concentration thresholds for fresh and salt water are less than or

equal to 0.029 (*i.e.*, fraction converted from saline concentration scale where 35 g/L is salt

water) and greater than 0.5, respectively. The relative concentration threshold for brackish

water is greater than 0.029 and less than 0.5 (i.e., between fresh and saltwater thresholds).

The present day steady-state simulation (mean tidal level) contained the most amount of

freshwater and the least amount of saltwater (Figure 29, No tide). The saltwater volume

increased for each SLR scenario both with and without the tides, but the saltwater volume

increased more drastically for each SLR scenario when the tide was turned on (Figure 29,

SLR1a, SLR2a, SLR3a, SLR4a). The worst case SLR scenario resulted in the highest

volume of saltwater of all simulations (Figure 29, SLR4a).

The highest volume of saltwater post-surge was calculated for the S2c scenario compared to S1a and S2a (Figure 29, S2c). However, the largest volume of brackish water was found after the S2a surge and not the S2c surge (Figure 29, S2a) as the overtopped saltwater infiltrated in a more uniform and concentrated way without the dyke (Figure 24, right panels). Turning the tides on increased the volume of saltwater compared to the no-tide scenarios for all surge simulations (e.g., Figure 29, S1 vs. S1a, S2 vs. S2a, S2b vs. S2c). The total volume of saltwater for each surge and SLR simulation was on the same order of magnitude (Figure 29).
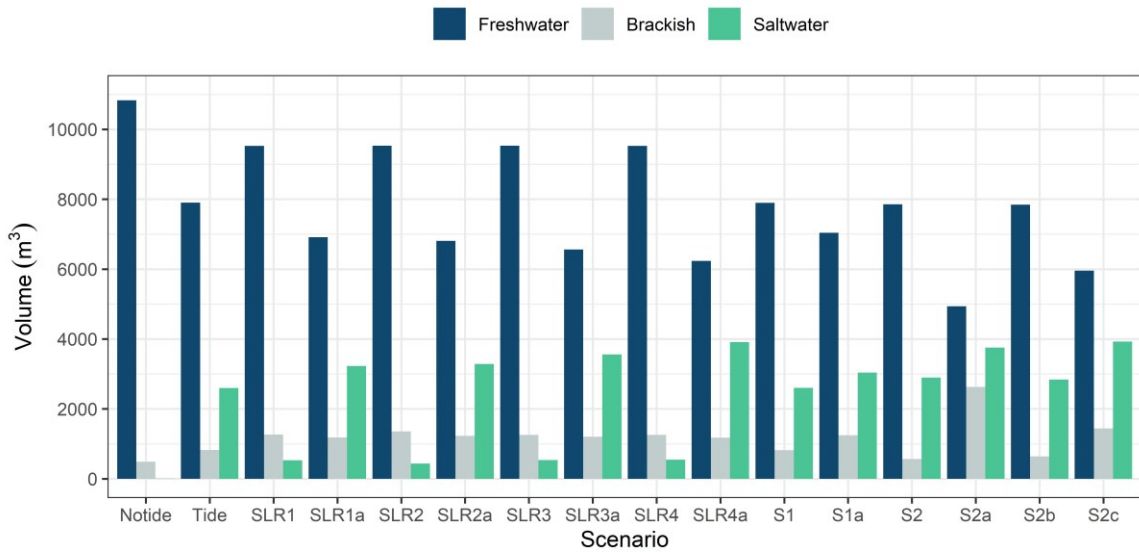
Figure 29. Freshwater, saltwater, and brackish water volumes in the modeling domain for each modeling scenario. Values presented are from the last timestep of each respective scenario simulation (mid-tide).

CHAPTER 5: CONCLUSION

5.1 Discussion of field investigations and implications

5.1.1 Aquifer properties and ocean-aquifer interactions

Data from the field instrumentation have yielded useful insights for understanding the local aquifer characteristics and properties, groundwater flow dynamics and conditions, ocean forcing, how the aquifer and ocean interact, and most importantly, how each of these processes or conditions can impact or exacerbate saltwater intrusion. Based on the literature review of previous geological mapping and the WalkTEM geophysical survey (Figure 18), the stratigraphy at the study site results in a confined aquifer system, with lower hydraulic conductivity material overlying a sand/gravel aquifer and a deeper bedrock aquifer layer (Freeze & Cherry, 1979; Hennigar & Kennedy, 2006; Rivard et al., 2012). With these confined conditions for the lower aquifer, the tidal pressure signal can penetrate far inland in the subsurface and therefore exerts key controls on the coastal groundwater flow elevations, hydraulic gradients, and resultant flow dynamics in this coastal area. With such high connectivity between domains, a perturbation from either side (*e.g.*, climate induced sea-level rise, storm surge, changes to groundwater recharge, or increase in pumping close to the coast) could have profound consequences from a groundwater resources perspective.

The field investigations confirmed that mega-tidal conditions strongly influenced the groundwater conditions near the coastline. While other studies have demonstrated tidal-controlled groundwater dynamics (Fang et al., 2021; Levanon et al., 2017; Li & Jiao, 2001; Robinson & Li, 2004; Stark & Hay, 2014), mega-tidal forcing on groundwater systems has been largely overlooked. Observing such a large tidal amplitude in the groundwater level

at such a distance inland from the coast (Figure 14c) was unexpected as other studies have shown signals that are much more damped at shorter distances inland from the coast (Inouchi et al., 1990; Li & Jiao, 2001; Slooten et al., 2010). The tidal oscillations in the deep groundwater data near the coast reveal the hydrogeological influence of the mega-tidal forcing along the Bay of Fundy and the degree of aquifer connectivity with the bedrock aquifer, presumably due to highly fractured conditions. Additionally, the geophysical survey conducted over half a tidal oscillation (Figure 18) indicates that the porewater salinity distribution underneath the area of the dyke is strongly influenced by tides (Ataie-Ashtiani et al., 1999). As the wave buoy confirmed that this area is a low-energy wave environment, the main forcing of concern for saltwater intrusion susceptibility is the mega-tidal conditions and any storm surges coincident with high tide. Such conditions are known as a storm tide. The strongest Fundy tides occur when the three-monthly cycles peak simultaneously, which only occurs every 18.03 years; this is known as the Saros (Desplanque & Mossman, 1999). Historically, a strong Saros has simultaneously occurred with major historical storm tides, with a famous example being the 1869 Saxby Tide, where the tide was at least 1.5 meters higher than typical high tide (Desplanque & Mossman, 1999). The modeling in in this thesis only considered typical semi-diurnal tidal levels in the Minas Basin within the Bay of Fundy. For such tidal conditions, only the 2-meter surge overtopped the dykes. However, a lower surge would be required for dyke overtopping if the surge was coincident with spring high tides, which can be up to a meter higher than mean high tide at the study site (Figure 6). The combination of surge dynamics at different tidal levels in the Bay of Fundy was recently considered by McLaughlin et al. (2022), and future groundwater modeling investigations could consider these paired marine forcings.

5.1.2 Implications for saltwater intrusion

The main results from the field investigations suggest that changes to the mean sea level or episodically elevated water levels during storm surges in the Minas Basin will drive saltwater intrusion in the aquifers underlying the town of Wolfville as these domains are highly interconnected. The impacts of saltwater intrusion could be devastating for the local drinking water and irrigation systems that rely on groundwater as the primary water resource (Hennigar & Kennedy, 2006). Increases in any water demand (and concomitant increases in pumping and decreases in groundwater levels) will only exacerbate the risk of saltwater intrusion (Michael et al., 2017). Water supplies extracted from the deep groundwater system could be at more risk of saltwater intrusion than the sand and gravel aquifer, but this requires further analyses. Finally, any reductions in recharge availability due to atmospheric climate change could result in further superimposed water stresses. Based on these findings there is a great need to better assess how climate change will impact the current dynamic system with the use of a numerical model informed by more hydrogeological field data. Given the model complexity and number of simulations required, this study focused on marine climatic changes as opposed to atmospheric changes (*e.g.*, recharge reductions).

5.2 Discussion of numerical modeling results

5.2.1 Model parameterization and opportunities for improvements

Several model limitations and opportunities for improvement should be considered when interpreting the results from this study, including parameter estimation, data collection, and numerical modeling improvements. The highly dynamic groundwater heads in the deep

observation well provided a unique opportunity for model calibration and parameterization, and the calibrated model reasonably matched the heads and electrical conductivity data from this well (Figure 8, nest 3). However, the tidal oscillations in salinity within the region of the upper saline plume as measured by the WalkTEM (Figure 18) appear to be higher than those in the model (Figure 21), suggesting that further model refinement could be achieved (*e.g.*, Hennigar & Kennedy, 2006).

The van Genuchten (1980) parameters that were initially used were based on values obtained specifically for the materials of interest in the model domain (Carsel & Parrish, 1988; van Genuchten, 1980). When examining the pressure-saturation and relative conductivity-saturation curves (Figure A4, a and b), the values used created sharp pressure-saturation curves that made it difficult for the model to desaturate and thus drastically impacted infiltration, which affected how much water could pass through the underlying geologic units. To allow the model to desaturate more easily, default van Genuchten parameters assigned in HydroGeoSphere were used, which drastically decreased model convergence times (Figure A4, c and d).

Geophysical data showing fresh and saline groundwater distributions can sometimes be more appropriate to calibrate a numerical model than hydraulic head data due to transient marine processes contributing to high temporal variability in hydraulic heads or density variations causing errors in hydraulic head measurements (Pavlovskii et al., 2022). In particular, saltwater-freshwater interface calibration based on geophysical data in homogeneous settings is an effective and computationally inexpensive model calibration approach (Pavlovskii et al., 2022). However, in this study, the interface lies offshore, and thus marine geophysics would be required to collect interface data to calibrate the

numerical model. Also, geophysics survey interpretation can be challenging in areas where stratigraphy is heterogenous, thus having a transect of deep, uncased boreholes (or boreholes containing multi-level piezometers) with detailed logs would be helpful for recording vertical resistivity profiles and ensuring resistivity changes due to salinity vs. stratigraphy are clear.

A transect of deep wells to monitor hydraulic head would provide a better understanding of the groundwater flow system. Several wells at different depths could yield improved insights into hydraulic properties (*e.g.*, hydraulic conductivity, storage), through, for example, pumping and recovery tests. Additionally, heterogeneity/anisotropy could be identified to create a representative three-dimensional model. Any tidal oscillations in these wells would serve as further calibration points for this transient model.

To simplify modeling endeavors, the salt marsh zone on the seaward side of the dyke was not considered as a separate 'sub-zone' in the model domain, as the deeper groundwater dynamics in behind the dyke were of primary interest for this project. For this project, the salt marsh area was assumed to be the same as the clay overburden confining layer in behind the dyke to reduce the number of zones and simplify the already rigorous calibration process. However, the hydraulic conductivity zone in the salt marsh area could drastically impact the shallow groundwater zone dynamics, wave attenuation, and tidal signal penetration. For this study, the properties for the clay layer across the top of the domain (including the salt marsh zone) were adjusted until the modeled hydraulic head oscillation in the deeper aquifer matched the hydraulic head measurements (Figure 20c). As a result, the modeled hydraulic head in the clay layer did not match the measured shallow hydraulic head data from the salt marsh zone. More field data and numerical model calibration should

be done to consider this salt marsh zone, and indeed, the salt marsh zone could be studied on its own to yield new insight into salt marsh hydrogeology in cold climates, which is not well studied (Guimond & Tamborski, 2021).

Lastly, to prevent numerical dispersion from occurring, the element sizes in the model grid should be reduced. The smallest element sizes are between $x = 550$ and 1100 meters, where they are at most two meters in width and height, and there is no numerical dispersion occurring in this area. On the landward and seaward sides of the domain between $x = 0$ and 550 meters, and $x = 1100$ and 1400 meters, the maximum element sizes are 10 meters in width and 2.5 meters in height, where limited numerical dispersion does appear to occur (Figure A5). All element sizes throughout the domain should be reduced to no more than 2 meters in width and height to prevent numerical dispersion. This would add several more months of modeling and thus was not completed within this thesis project that already extended over two years.

5.2.2 Impacts of simulated lateral saltwater intrusion

The modeling results from mode 1 (Figure 22), lateral saltwater intrusion, reveal that sea-level rise will drive expansion of the upper saline plume which could threaten the groundwater resources that the town relies on for their drinking water supply. Although movement of the upper saline plume has received far less attention than movement of the deeper saltwater-freshwater interface in the context of saltwater intrusion (Werner et al., 2013), these modeling results indicate that upper saline plume dynamics are important in mega-tidal settings. These simulations indicate that the upper saline plumes formed in the

intertidal zone are due to tide- and density-induced saltwater circulation, as the plume dispersion and mixing did not occur during the gradually increasing SLR simulations (Figure 22a-d). The projected sea-level rise rate for 2050 (both RCP 2.6 and 8.5) does not pose a significant threat to the coastal freshwater resources, as the upper saline plume extent does not move inland, at least without the inclusion of groundwater pumping. Additionally, the salt wedge location does not move inland and does not extend past the location of the freshwater well ($x = 600$ meters, $z = 70$ meters below sea level); it remains seaward and outside of the model domain. However, the projected sea-level rise rates for 2100 (both RCP 2.6 and 8.5) do pose more of a threat to the fresh groundwater resources because the upper saline plume becomes more unstable and spread landward (Figure 22h). In this scenario, the plume is only approximately 60 meters away from the location of the monitoring well, which could be well within the capture zone (*e.g.*, Hennigar & Kennedy, 2006). If the monitoring well ($x = 600$ meters, $z = 70$ meters below sea level) began to pump water from this deep aquifer, it could begin to extract saltwater under the SLR4a scenario. If pumped for longer periods of time at a high pumping rate, this well could be at risk of saltwater intrusion under all of the SLR scenarios (Figure 22). It is important to note that this well is presently only being used for monitoring, and the measured electrical conductivity is already slightly above the drinking water threshold, although it is difficult to say if that may be an artifact of infiltrated Minas Basin water from many centuries ago when the dykes were not in place and that land would have flooded regularly. In general, the SLR scenarios demonstrate that the magnitude of sea-level change is important to consider for near-coast wells in this town.

The results from Figure 22 reveal that the mega-tides increase the width of the transition zone between the saltwater and freshwater (Inouchi et al., 1990; Kuan et al., 2012). However, this increase in the size of the transition zone does not appear to extend laterally landward, but rather downward and seaward. This is likely due to the landside freshwater head boundary forcing seaward flow that inhibits the landward plume migration (Ataie-Ashtiani et al., 1999; Lu et al., 2015; Park & Aral, 2008). The upper saline plume extends downward (from original 1% isocontour to new 1% isocontour) by over 33 meters for the worst-case SLR scenario (*i.e.*, 2100 RCP 8.5) and reaches the bottom of the domain. If the domain were extended vertically, the maximum dispersion of the plume could be identified. Also, for all SLR scenarios, the upper saline plume was still changing after just over two years post-SLR with the tides re-imposed, and likely would continue to change for several decades (Fang et al., 2022; Kuan et al., 2012).

The model simulations did not have enough time to re-equilibrate within the two years of post-SLR with the tides re-imposed. Other studies have shown that the post-SLR equilibration can take several decades (Chang et al., 2011; Morgan et al., 2015; Watson et al., 2010). To fully investigate these dynamics, the simulations should likely be run out for several decades to establish a new equilibrium.

5.2.3 Impacts of simulated vertical saltwater intrusion

Storm surge simulations for both 2050 and 2100 (RCP 8.5) with and without the dyke all had significant impacts on the salinity distribution along the transect. Even without overtopping, the 1-meter surge resulted in almost an 11% decrease in the volume of freshwater after nearly four years, a trend that is expected to continue based on the

freshwater volume over time relationship (Figure 28). While this particular surge did not overtop the dyke or cause shallow salinization, the heightened water level did cause a larger upper saline plume to develop which could cause saltwater intrusion for deep pumping wells along the coast, depending on the depth, pumping rate, and well proximity to the coastline.

During the 2-meter surges (Figure 24, Figure 25), the sea level was high enough to overtop the dyke and inundate the agricultural land in behind the dyke for a storm duration of 2 hours. After the 2-meter surge (S2a, Figure 24b), the salt plume migrated both landward and seaward, with a decrease of nearly 33% in the freshwater volume after almost four years. The saltwater flooding in behind the dyke resulted in shallow salinization that persisted within the four years of the simulation. When tides were incorporated, salt fingers developed within four years post-surge (Figure 26a, $t = 4$ years), but did not develop within the same time frame when tides were removed (Figure 27a, $t = 4$ years). These results suggest that the mega tides increase flushing times of the aquifer post-surge, but longer post-surge simulations are required to confirm this finding. Based on the relationship in Figure 28, the saltwater will likely take years to decades to completely exfiltrate and return to the pre-surge state, which is in line with previous studies (Cardenas et al., 2015; Vithanage et al., 2012; Xiao et al., 2019).

When the dyke was removed, the 2-meter surge infiltrated the land behind the dyke (S2c, Figure 24c) and resulted in more seawater volume available for infiltration. The salt plume migrated both landward and seaward, with a decrease of just over 24% in the freshwater volume after four years. While it took two years for the salt fingers to develop in the simulation that contained the dyke, it took four years for the salt fingers to start to develop

in the simulation without the dyke (Figure 24b, t = 4 years). When running the same simulation post-surge without the dyke and without tides, the results look very similar (Figure 24b and Figure 25b). The higher head and salt concentration along the landward side of the dyke are a result of the dyke not being present to prevent this more intense flooding and salinization (*e.g.*, Figure 24b and c). In general, these model runs point to the potential impacts of dyke removal on the subsurface system, and such potential impacts of intentional dyke breaching have generally been overlooked.

While the impacts of the S2c surge were more intense than the S2a surge, the freshwater volume after four years is lower for the latter (Figure 28). This is likely because the S2c surge has not yet had enough time to disperse. The freshwater volume will likely decrease more for the S2c surge compared to the S2a surge if the simulations were run out for several decades (*e.g.*, 20 years), which could require several more months of simulation time, at least with tides turned on. After four years, the salt fingers were only just starting to develop for the S2c surge (Figure 24b) whereas they started developing after six months for the S2a surge (Figure 24a). The salt fingering phenomenon is driven by density influences but can also be highly sensitive to the model grid and cell size (Post & Houben, 2017). To prevent numerical dispersion (Figure A5), a smaller grid size should be used on the landward side of the domain where the salt fingers have developed to ensure all fingers are density-driven phenomenon and not the artifact of a mesh that is too coarse for the forcing.

The freshwater volume in the domain decreases over time after the surge for all three scenarios as the upper saline plume is impacted by both tidal pumping and density-dependent flow influences (Figure 28). Importantly, a decrease in the freshwater volume over time with a constant (or oscillating) boundary condition does not necessarily imply

the salt mass is increasing in the model, but rather that the salt is dispersing and causing a larger volume to be brackish. The S1a, S2a, and S2c surge simulations resulted in a freshwater volume decrease of 10.9%, 32.5%, and 24.1%, respectively over 4 years. During the first 3 years, the S2a surge resulted in a more rapid decrease in the freshwater volume compared to the S2c surge which had a higher saline concentration behind the dyke (Figure 24c). The freshwater volume in the domain will likely continue to decline for several years based on the relationship shown in Figure 28. Due to time constraints, the simulations could not be run to assess the full flushing times of the aquifers post-surges. For example, simulation times for the post-surge simulations even on the ACENET Siku cluster exceeded one month and would have taken over one year on our lab's high-performance computer based on a comparison of shorter runs.

Findings from this study differ from other storm surge studies for several reasons. The surge height used in this study was relatively small compared to other storm surge and overtopping studies as prior studies were often based on tsunamis or tropical cyclones (Cardenas et al., 2015; Illangasekare et al., 2006). Yang et al. (2013) used a 6.6 m surge that lasted for 2.8 hours and overtopped a dyke, and they found that after 20 years of simulation, the aquifer did not return to its pre-surge state. Additionally, this former study used similar parameters with the same numerical model (HydroGeoSphere), but with a much lower tidal range (3.8 m) on the seaside boundary and a much larger surge height (*i.e.*, three times larger, Yang et al., 2013). Lastly, other studies have simulated several recurring storm surges, some of increasing magnitude and frequency (Goldenberg et al., 2001; Paldor & Michael, 2021; Tebaldi et al., 2012). This study only simulated a single, short-term overtopping event based on projected values for the Minas Basin area (Webster

et al., 2012). Assessing the impact of multiple magnitudes and frequencies of storms should be considered in future studies to more fully investigate how climate-driven increases to the intensity and frequency of storm surges could influence critical groundwater resources.

5.2.4 Agricultural impacts

Many agricultural fields worldwide are located within kilometers of the coastline, and thus are highly vulnerable to a loss of arable conditions and poor drainage due to climate change induced coastal flooding or sea-level rise (Nicholls et al., 2021; Pitman & Läuchli, 2002; Schieder et al., 2018). Due to crop intolerance to salt, many farmlands will become abandoned over time, with drastic differences in the types of plants that are able to grow in these coastally impacted areas (Butcher et al., 2018; Fagherazzi et al., 2019; Gedan & Fernández-Pascual, 2019). For the case of the Bay of Fundy dykelands, this could result in a devastating loss of valuable agricultural land, as the surge simulations revealed that the shallow salinization after overtopping remained in the top few meters below the surface (*i.e.*, within critical agricultural soils) for the entire duration of simulations (*i.e.*, four years). While these simulations did not capture the full extent of salinization post-surge, they do highlight that the shallow soil remains salinized beyond just the 2-hour surge, and likely for several decades (Guimond & Michael, 2020).

A 2-meter surge has the potential to drastically impact the crop yield, depending on the crop being grown and its tolerance to salinity. Another important consideration is the saturation level that crops can tolerate. With sea-level rise and more frequent or intense overtopping, the agricultural land may be characterized by higher moisture contents in the vadose zone (post-surge) and/or a shallower water table (Bjerklie et al., 2012; Ferguson &

Gleeson, 2012; Rotzoll & Fletcher, 2013). Altering salinity and saturation in these fields will favour growth of different species, such as marsh plants, but will not be favorable for agricultural crops, such as corn or soybeans (Butcher et al., 2018; Fagherazzi et al., 2019; Pitman & Läuchli, 2002). A long-term balance of salinity can only be achieved if there is adequate drainage, as some species of crops can handle a certain threshold of salt that is not sustained (Skaggs & van Schilfgaarde, 1999).

5.2.5 Dykeland management recommendations

This study has highlighted new considerations necessary for quantifying risks and informing sustainable groundwater management in dyked areas. Coastal agricultural regions are vulnerable to crop salinization as a result of climate change which could have global implications for food security and other coastal ecosystem services (Chen et al., 2020; IPCC, 2019; Michael et al., 2017; Sherren et al., 2021; Tully et al., 2019). Results from this modeling study point to the need to manage dykes in a way that considers both surface and subsurface ecosystem services, as resources from both domains are critical for a sustainable future.

Recommendations for dyke management along the Bay of Fundy based on this study include primarily two suggestions. First, if the present dykelands are to be maintained, it is recommended to top the dykes up to increase the critical elevation to prevent overtopping, as the numerical model results using the 2-meter surge projection for 2100 showed sustained shallow salinization (Figure 24c) and saturation which could have profound implications for agricultural crops. Also, the overtopping events show how the shallow

aquifer system is impacted for years, and likely decades, which could have sustained and deleterious impacts on coastal freshwater drinking supplies. The deep aquifer system is likely also impacted by the overtopping events, but model simulations will need to be run out for decades to assess how infiltrated saltwater mixes and dilutes over time. The mega tides will likely decrease the travel time of saline water flowing towards the ocean as the low tide pressure signal allows for more significant seaward flow compared to the same post-surge simulation without the tide. Increasing the height of the dykes would reduce the amount of agricultural land but it would prevent most overtopping events (Bowron et al., 2012; van Proosdij et al., 2010). Analyses of the required increase in dyke height should consider sea-level rise, storm surges, and multi-constituent tide dynamics (e.g., McLaughlin et al., 2022). Additionally, restoring the salt marsh in front of the dyke would help prevent erosion of the structure and promote wave attenuation to reduce wave energy and thus erosion of the coastal barrier (Guimond & Tamborski, 2021; Sherren et al., 2019; van Proosdij et al., 2010).

5.3 Recommendations for future work

To better assess how dykelands and coastal groundwater systems respond to anthropogenic and climate change perturbations, several recommendations are suggested to improve understanding and ultimately model calibration. First, more extensive geological investigations (*e.g.*, deep boreholes) from the coast to the town would be helpful to confirm the stratigraphy profile and salinity distribution, as only nearby well logs were available, and the area to known to be heterogeneous and anisotropic. In addition to more boreholes, a longer transect of both shallow and deep piezometers would be useful for aquifer

characterization through, for example, pumping and recovery tests. The piezometers drilled in this study were clustered around the coast due to a limitation of available data loggers and challenges in drilling on private land. Extending this transect further inland would reduce potential errors in the landside freshwater head boundary condition. Next, additional geophysics surveys with the WalkTEM and a larger loop (40 m by 40 m) would be useful for potentially mapping the saltwater-freshwater interface location with more confidence, as this loop size can penetrate deeper with higher accuracy. This transect should also extend further inland to compare with hydraulic head measurements (e.g., Pavlovskii et al., 2022). Marine-based geophysical surveys would also be helpful for delineating the shallower interface location. Also, several time-lapse WalkTEM surveys (Figure 18) during different tidal cycles (*e.g.*, spring, neap) that capture both the flood and the ebb tide would help to identify and parse out different tidal impacts on the groundwater flow and tidal mixing dynamics. Lastly, a three-dimensional model would be beneficial to be able to incorporate aboiteaux and tile drainage throughout the domain. A drainage system is difficult to incorporate in a two-dimensional model and was beyond the scope of this study. However, incorporating a drainage system could drastically impact the drainage of saltwater after an overtopping event, depending on the flow routing system and location of the drains. Also, the vulnerability of the aquifer to salinization after surge events may be much more probable along certain parts of the dyked coastline, as there are certain areas that already experience overtopping during spring-high tides. Surge impacts in these areas could be much more devastating and should be considered in future studies. A three-dimensional model would be useful for providing larger scale dykeland management recommendations, as there may be some management techniques that are better suited to certain areas, but not to all. Additionally, incorporating pumping in a three-dimensional model should be

considered to assess how the climate change scenarios could impact fresh groundwater resources. The inclusion of groundwater pumping could be paired with the application of irrigated water as another source of recharge within the agricultural land.

5.4 Conclusions

This study investigated the potential for saltwater intrusion along the Bay of Fundy dykelands in response to sea-level rise, storm surge overtopping, and dyke removal. Particular emphasis was placed on the dynamics of the tide-driven upper saline plume. Results from the field investigations elucidate ocean-aquifer interactions and reveal that the coastal aquifer is strongly impacted by pumping and saltwater circulation from the mega-tidal conditions. Results from the climate change simulations show that the coastal aquifer was vulnerable to increased salinization from both rising seas and intensifying coastal storms. The results revealed that surge induced overtopping posed the largest threat to the aquifer, as this climate stressor resulted in the largest reduction in freshwater volume and sustained salinization of the shallow agricultural soils.

The SLR results showed that the increased water level also increased the width and height of the upper saline plume. While there is no active pumping well nearby, there could be consequences if the monitoring well at $x = 600$ meters began extracting water, as under the worst-case SLR scenario, the plume is only 60 meters away, which could easily lie within the well's capture zone.

The surge results showed that even without dyke overtopping, an increased higher water level causes the upper saline plume to expand horizontally and vertically. When the dyke

was overtopped, salt fingers developed after six months and were still migrating downwards after four years, when the tidal forcing was in play. For the same scenario without the tides, salt fingers did not develop within the four years post-surge, which suggests that the mega tides increase the aquifer flushing times. When the dyke was removed and a surge event occurred, the volume of saltwater behind where the dyke used to be was higher than the volume behind the dyke when the dyke was not removed; however more ponding occurred immediately landward of the dyke when the dyke was left intact within the model. The agricultural land behind the dyke (for both the dyke and no dyke simulations, both with and without the tides) remained salinized after four years of simulation, and the infiltrated saltwater will likely require decades to dilute and exfiltrate based on extrapolating the freshwater volume decline versus time relationship.

The impacts of mega tides have generally received less attention in the saltwater intrusion literature and were a primary focus in this study. Mega tides generated a pronounced upper saline plume that was also responsive to change in sea level and temporary surge overtopping; these dynamics would be overlooked if tides were excluded or were considered at typical micro- or macro-tidal conditions. Given the confined aquifer conditions and fresh submarine groundwater discharge forcing the freshwater-saltwater interface seaward, there was remarkably little saltwater in the model domain for all SLR simulations until the tides were turned on. The tides in these simulations decreased the freshwater volume by 27% for the best-case and 35% for the worst-case, and these values will likely increase for a certain period as the post-SLR equilibrium was not reached. The tides also played key roles in the aquifer response to surges. When the tides were on, the upper saline plume expanded post-surge for all scenarios. Additionally, when the tides were

imposed, the salt fingers started to develop within six months post-surge for the scenario with the dyke and did not develop within four years for the scenario without the dyke. When the tides were turned off, the salt fingers did not develop within four years post-surge for the scenarios with and without the dyke. These results suggest that mega tides increase the aquifer dynamics, facilitate density-driven flow phenomenon, and generally decrease the aquifer flushing times.

To better assess the impacts of SLR and surge-induced overtopping events along the Bay of Fundy dykelands, more spatiotemporally varying hydraulic head and geophysical data would help to improve model calibration and assessment. The hydraulic head data would allow for a better understanding of the spatial distribution of head and could be used for validation of the model outputs. More resistivity profiles and time-lapse surveys would help to capture the freshwater-saltwater interface and extent of tidal impacts. Also, deep borehole logs would be helpful for investigating the stratigraphic profile and resultant changes in hydraulic conductivity. Lastly, all these recommendations would better support the development of a three-dimensional numerical model which could be used for more realistic and reliable simulations to better inform dykeland management strategies for a larger area and with groundwater pumping and irrigation scenarios considered.

The climate change assessment conducted in this study highlights new risks that should be considered in provincial dykeland management and climate change adaptation plans. Considering how different dykeland management strategies impact coastal-aquifer interactions and fresh groundwater drinking supplies has generally been overlooked in dykeland decision making processes that focus on surface conditions. Human decision making is often emotive, and we tend to focus on what we can *see and experience*. Further

research and associated communication on the *unseen* subsurface influence of tides, dykes,

sea-level rise, and storm surges is needed to increase stakeholders' and decisionmakers'

awareness and to develop climate-resilient coastlines in Nova Scotia and worldwide.

REFERENCES

Abd-Elhamid, H. F., & Javadi, A. A. (2011). A density-dependant finite element model for analysis of saltwater intrusion in coastal aquifers. *Journal of Hydrology*, *401*(3–4), 259–271. https://doi.org/10.1016/j.jhydrol.2011.02.028

Anderson, M. P., Woessner, W. W., & Hunt, R. J. (2015). Modeling Fundamentals. In M. P. Anderson, W. W. Woessner, & R. J. Hunt (Eds.), *Applied Groundwater Modeling (Second Edition)* (Second Edi, p. 1). Academic Press. https://doi.org/https://doi.org/10.1016/B978-0-08-091638-5.00013-4

Aquanty. (2015a). *HGS Reference Manual*. Aquanty Inc. https://www.aquanty.com/hydrogeosphere

Aquanty. (2015b). *HGS Theory Manual*. Aquanty Inc. https://www.aquanty.com/hydrogeosphere

Archie, G. E. (1942). The electrical resistivity log as an aid in determining some reservoir characteristics. *Petroleum Techonology*, *55*, 9–16. https://doi.org/10.2118/942054-g

Ataie-Ashtiani, B., Volker, R. E., & Lockington, D. A. (1999). Tidal effects on sea water intrusion in unconfined aquifers. *Journal of Hydrology*, *216*(1–2), 17–31. https://doi.org/10.1016/S0022-1694(98)00275-3

Badaruddin, S., Werner, A. D., & Morgan, L. K. (2015). Water table salinization due to seawater intrusion. *Water Resources Research*, *51*, 8397–8408. https://doi.org/10.1111/j.1752-1688.1969.tb04897.x

Bayabil, H. K., Li, Y., Tong, Z., & Gao, B. (2020). Potential management practices of saltwater intrusion impacts on soil health and water quality: a review. *Journal of Water and Climate Change*, 1–17. https://doi.org/10.2166/wcc.2020.013

Beebe, C. (2011). *Investigation of occurrence and assessment of risk of saltwater intrusion in Nova Scotia, Canada* [MSc thesis, Saint Francis Xavier University]. https://www.collectionscanada.gc.ca/obj/thesescanada/vol2/002/MR83796.PDF?is_thesis=1&oclc_number=853308786

Befus, K. M., Barnard, P. L., Hoover, D. J., Hart, J. A. F., & Voss, C. I. (2020). Increasing threat of coastal groundwater hazards from sea-level rise in California. *Nature Climate Change*, *10*(October). https://doi.org/10.1038/s41558-020-0874-1

Bennett, E. M., Baird, J., Baulch, H., Chaplin-Kramer, R., Fraser, E., Loring, P., Morrison, P., Parrott, L., Sherren, K., Winkler, K. J., Cimon-Morin, J., Fortin, M. J., Kurylyk, B. L., Lundholm, J., Poulin, M., Rieb, J. T., Gonzalez, A., Hickey, G. M., Humphries, M., … Lapen, D. (2021). Ecosystem services and the resilience of agricultural landscapes. *Advances in Ecological Research*, *64*, 1–43. https://doi.org/10.1016/BS.AECR.2021.01.001

Bennett, E. M., Peterson, G. D., & Gordon, L. J. (2009). Understanding relationships among multiple ecosystem services. *Ecology Letters*, *12*(12), 1394–1404. https://doi.org/10.1111/j.1461-0248.2009.01387.x

Bhattachan, A., Emanuel, R. E., Ardón, M., Bernhardt, E. S., Anderson, S. M., Stillwagon, M. G., Ury, E. A., BenDor, T. K., & Wright, J. P. (2018). Evaluating the effects of land-use change and future climate change on vulnerability of coastal landscapes to saltwater intrusion. *Elementa*, *6*. https://doi.org/10.1525/elementa.316

Bjerklie, D., Mullaney, J., Stone, J., Skinner, B., & Ramlow, M. (2012). Simulations of the effects of sea-level rise on groundwater levels, New Haven, Connecticut. In *USGS Open File Report* (Vol. 44, Issue 2).

Boateng, I. (2012). GIS assessment of coastal vulnerability to climate change and coastal adaption planning in Vietnam. *Journal of Coastal Conservation*, *16*(1), 25–36. https://doi.org/10.1007/s11852-011-0165-0

Bobba, A. G. (2002). Numerical modelling of salt-water intrusion due to human activities and sea-level change in the Godavari Delta, India. *Hydrological Sciences Journal*, *47*, S67–S80. https://doi.org/10.1080/02626660209493023

Bowron, T., Neatt, N., van Proosdij, D., & Lundholm, J. (2012). Salt marsh tidal restoration in Canada's maritime provinces. In C. T. Roman & D. M. Burdick (Eds.), *Tidal Marsh Restoration: A Synthesis of Science and Management* (1st ed., pp. 191–209). Island Press, Washington, DC. https://doi.org/10.5822/978-1-61091-229-7

Briggs, M. A., Cantelon, J. A., Kurylyk, B. L., Kulongoski, J. T., Mills, A., & Lane, J. W. (2021). Small atoll fresh groundwater lenses respond to a combination of natural climatic cycles and human modified geology. *Science of The Total Environment*, *756*, 143838. https://doi.org/10.1016/J.SCITOTENV.2020.143838

Brovelli, A., Mao, X., & Barry, D. A. (2007). Numerical modeling of tidal influence on density-dependent contaminant transport. *Water Resources Research*, *43*(10), 1–15. https://doi.org/10.1029/2006WR005173

Butcher, K., Wick, A. F., Desutter, T., Chatterjee, A., & Harmon, J. (2018). Corn and soybean yield response to salinity influenced by soil texture. *Agronomy Journal*, *110*(4), 1243–1253. https://doi.org/10.2134/agronj2017.10.0619

Byers, S. E., & Chmura, G. L. (2007). Salt marsh vegetation recovery on the Bay of Fundy. *Estuaries and Coasts*, *30*(5), 869–877. https://doi.org/10.1007/BF02841340

Byers, S. E., & Chmura, G. L. (2014). Observations on shallow subsurface hydrology at Bay of Fundy macrotidal salt marshes. *Journal of Coastal Research*, *30*(5), 1006–1016. https://doi.org/10.2112/JCOASTRES-D-12-00167.1

Cantelon, J. A., Guimond, J. A., Robinson, C. E., Michael, H. A., Kurylyk, B. L., Engineering, R., Studies, W. R., Scotia, N., Engineering, E., & Sciences, E. (2022). Vertical saltwater intrusion in coastal aquifers driven by episodic flooding: A review. *Water Resources Research, 58*(11). https://doi.org/10.1029/2022WR032614

Cardenas, M. B., Bennett, P. C., Zamora, P. B., Befus, K. M., Rodolfo, R. S., Cabria, H. B., & Lapus, M. R. (2015). Devastation of aquifers from tsunami-like storm surge by Supertyphoon Haiyan. *Geophysical Research Letters*, *42*(8), 2844–2851. https://doi.org/https://doi.org/10.1002/2015GL063418

Carr, P. A. (1971). Use of harmonic analysis to study tidal fluctuations in aquifers near the sea. *Water Resources Research*, *7*(3), 632–643. https://doi.org/10.1029/WR007i003p00632

Carrión-Mero, P., Montalván, F. J., Morante-Carballo, F., Loor-Flores de Valgas, C., Apolo-Masache, B., & Heredia, J. (2021). Flow and transport numerical model of a coastal aquifer based on the hydraulic importance of a dyke and its impact on water quality. Manglaralto—Ecuador. *Water*, *13*(4), 443. https://doi.org/10.3390/w13040443

Carsel, R., & Parrish, R. (1988). Developing joint probability distributions of soil water retention characteristics. *Water*, *24*(5), 755–769.

Cartwright, N., Nielsen, P., & Li, L. (2004). Experimental observations of watertable waves in an unconfined aquifer with a sloping boundary. *Advances in Water Resources*, *27*(10), 991–1004. https://doi.org/10.1016/j.advwatres.2004.08.006

CBCL, & WATER. (2009). *Groundwater Use Database - Methodology and Data Summary. Annapolis Valley, Nova Scotia.* CBCL Limited and Nova Scotia Department of Natural Resources, project no. 081242.

Chang, S. W., & Clement, T. P. (2012). Experimental and numerical investigation of saltwater intrusion dynamics in flux-controlled groundwater systems. *Water Resources Research*, *48*(9), 1–10. https://doi.org/10.1029/2012WR012134

Chang, S. W., Clement, T. P., Simpson, M. J., & Lee, K. K. (2011). Does sea-level rise have an impact on saltwater intrusion? *Advances in Water Resources*, *34*(10), 1283–1291. https://doi.org/10.1016/J.ADVWATRES.2011.06.006

Chen, Y., Caesemaecker, C., Rahman, H. T., & Sherren, K. (2020). Comparing cultural ecosystem service delivery in dykelands and marshes using Instagram: A case of the Cornwallis (Jijuktu'kwejk) River, Nova Scotia, Canada. *Ocean and Coastal Management*, *193*, 1–30. https://doi.org/10.1016/j.ocecoaman.2020.105254

Cimon-Morin, J., Goyette, J.-O., Mendes, P., Pellerin, S., & Poulin, M. (2021). A systematic conservation planning approach to maintaining ecosystem service provision in working landscapes. *Facets*, *6*, 1570–1600. https://doi.org/10.1139/facets-2020-0100

Cooper, H. H. (1964). *Sea water in coastal aquifer (No. 1613)*. *U. S. Geological Survey Water-Supply paper* 1613-C. US Government Printing Office.

Davis, D., & Browne, S. editors. (1997). *The natural history of Nova Scotia* (Vol. 2). Nova Scotia Museum, the Department of Education and Culture. https://ojs.library.dal.ca/NSM/article/view/3775

Desplanque, C., & Mossman, D. J. (1999). Storm tides of the Fundy. *Geographical Review*, *89*(1), 23–33. https://doi.org/10.2307/216138

Elsayed, S. M., & Oumeraci, H. (2018a). Modelling and management of storm-driven saltwater intrusion in freshwater aquifers: The case of near Bremerhaven, Germany. *Integrating Ecosystems in Coastal Engineering Practice (INECEP)*, *September*, 150–168. https://cuvillier.de/de/shop/publications/7662

Elsayed, S. M., & Oumeraci, H. (2018b). Modelling and mitigation of storm-induced saltwater intrusion: Improvement of the resilience of coastal aquifers against marine floods by subsurface drainage. *Environmental Modelling and Software*, *100*, 252–277. https://doi.org/10.1016/j.envsoft.2017.11.030

Elsayed, S. M., Oumeraci, H., & Goseberg, N. (2018). Erosion and breaching of coastal barriers in a changing climate: Associated processes and implication for contamination of coastal aquifers. *Proceedings of the Coastal Engineering Conference*, *36*(2018), 1–22. https://doi.org/10.9753/icce.v36.papers.107

Epanchin-Niell, R. S., Boyd, J. W., Macauley, M. K., Scarlett, L., Shapiro, C. D., & Williams, B. K. (2018). Integrating adaptive management and ecosystem services concepts to improve natural resource management— Challenges and opportunities. In *U.S. Geological Survey Circular 1439*. https://doi.org/https://doi.org/10.3133/cir1439

Erwin, K. L. (2009). Wetlands and global climate change: The role of wetland restoration in a changing world. *Wetlands Ecology and Management*, *17*(1), 71–84. https://doi.org/10.1007/s11273-008-9119-1

Fagherazzi, S., Anisfeld, S. C., Blum, L. K., Long, E. v., Feagin, R. A., Fernandes, A., Kearney, W. S., & Williams, K. (2019). Sea level rise and the dynamics of the marsh-upland boundary. *Frontiers in Environmental Science*, *7*(FEB), 1–18. https://doi.org/10.3389/fenvs.2019.00025

Fang, Y., Zheng, T., Guo, B., Zhan, H., Wang, H., Zheng, X., & Walther, M. (2022). Transformation in the stability of tide-induced upper saline plume driven by transient external forcing. *Water Resources Research*, *58*(6). https://doi.org/10.1029/2021WR031331

Fang, Y., Zheng, T., Zheng, X., Yang, H., Wang, H., & Walther, M. (2021). Influence of tide-induced unstable flow on seawater intrusion and submarine groundwater discharge. *Water Resources Research*, *Figure 1*, 1–17. https://doi.org/10.1029/2020wr029038

Ferguson, G., & Gleeson, T. (2012). Vulnerability of coastal aquifers to groundwater use and climate change. *Nature Climate Change*, *2*(5), 342–345. https://doi.org/10.1038/nclimate1413

Feseker, T. (2007). Numerical studies on saltwater intrusion in a coastal aquifer in northwestern Germany. *Hydrogeology Journal*, *15*(2), 267–279. https://doi.org/10.1007/s10040-006-0151-z

Forbes, D. L., Manson, G. K., Charles, J., Thompson, K. R., & Taylor, R. B. (2009). *Halifax Harbour extreme water levels in the context of climate change: scenarios for a 100-year planning horizon, Geological Survey of Canada, Open File 6346.*

Freeze, R. A., & Cherry, J. A. (1979). *Groundwater*. Prentice-Hall, Inc., Englewood Cliffs, N.J.

Frigo, M., & Johnson, S. G. (1998). FFTW: an adaptive software architecture for the FFT. *Proceedings of the 1998 IEEE International Conference on Acoustics, Speech and Signal Processing, ICASSP '98 (Cat. No.98CH36181)*, *3*, 1381–1384 vol.3. https://doi.org/10.1109/ICASSP.1998.681704

Gedan, K. B., & Fernández-Pascual, E. (2019). Salt marsh migration into salinized agricultural fields: A novel assembly of plant communities. *Journal of Vegetation Science*, *30*(5), 1007–1016. https://doi.org/10.1111/jvs.12774

Ghyben, W. B. (1988). Nota in verband met de voorgenomen putboring nabij Amsterdam. *Tijdschrift van Let Knoinklijk Inst.*

Goldenberg, S. B., Landsea, C. W., Mestas-Nuñez, A. M., & Gray, W. M. (2001). The recent increase in Atlantic hurricane activity: causes and implications. *Science*, *293*(5529), 474–479. https://doi.org/10.1126/science.1060040

Gómez-Baggethun, E., Tudor, M., Doroftei, M., Covaliov, S., Năstase, A., Onără, D. F., Mierlă, M., Marinov, M., Doroșencu, A. C., Lupu, G., Teodorof, L., Tudor, I. M., Köhler, B., Museth, J., Aronsen, E., Ivar Johnsen, S., Ibram, O., Marin, E., Crăciun, A., & Cioacă, E. (2019). Changes in ecosystem services from wetland loss and restoration: An ecosystem assessment of the Danube Delta (1960–2010). *Ecosystem Services*, *39*, 100965. https://doi.org/10.1016/J.ECOSER.2019.100965

Gonneea, M. E., Mulligan, A. E., & Charette, M. A. (2013). Climate-driven sea level anomalies modulate coastal groundwater dynamics and discharge. *Res. Lett*, *40*, 2701–2706. https://doi.org/10.1002/grl.50192

Green, N. R., & MacQuarrie, K. T. B. (2014). An evaluation of the relative importance of the effects of climate change and groundwater extraction on seawater intrusion in coastal aquifers in Atlantic Canada. *Hydrogeology Journal*, *22*(3), 609–623. https://doi.org/10.1007/s10040-013-1092-y

Greenberg, D. A., Blanchard, W., Smith, B., & Barrow, E. (2012). Climate change, mean sea level and high tides in the bay of fundy. *Atmosphere - Ocean*, *50*(3), 261–276. https://doi.org/10.1080/07055900.2012.668670

Guimond, J. A., & Michael, H. A. (2020). Effects of marsh migration on flooding, saltwater intrusion, and crop yield in coastal agricultural land subject to storm surge inundation. *Water Resources Research*. https://doi.org/10.1029/2020wr028326

Guimond, J., & Tamborski, J. (2021). Salt marsh hydrogeology: a review. *Water*, *13*(543). https://doi.org/https://doi.org/10.3390/w13040543

Heiss, J., & Michael, H. (2014). Saltwater-freshwater mixing dynamics in a sandy beach aquifer over tidal, spring-neap, and seasonal cycles. *Water Resources Research*, *50*, 6747–6766. https://doi.org/10.1002/2013WR014979.Reply

Hennigar, T. W. (1972). Hydrogeology of the Truro area. *Nova Scotia Department of Mines, Groundwater Section Report 72-1*. 141. https://novascotia.ca/nse/groundwater/docs/GroundwaterResourcesReport_TruroArea.pdf

Hennigar, T. W., & Kennedy, G. W. (2006). Final report on the Wolfville aquifer model prepared for the town of Wolfville, *Water Consulting and CBCL Limited*. 55 pp.

Henry, H. (1960). Saltwater intrusion into coastal aquifers. *U. S. Geological Survey Open-File Report*, 42 pp. https://doi.org/10.3133/ofr6065

Herzberg, A. (1901). Die Wasserversorgung einiger Nordseebader. *J. Gasbeleucht*.

Hiscock, K. M., & Bense, V. F. (2014). *Hydrogeology: principles and practice*. John Wiley & Sons, Ltd.

Huizer, S., Karaoulis, M. C., Oude Essink, G. H. P., & Bierkens, M. F. P. (2017). Monitoring and simulation of salinity changes in response to tide and storm surges in a sandy coastal aquifer system. *Water Resources Research*, *53*(8), 6487–6509. https://doi.org/10.1002/2016WR020339

Illangasekare, T., Tyler, S. W., Clement, T. P., Villholth, K. G., Perera, A. P. G. R. L., Obeysekera, J., Gunatilaka, A., Panabokke, C. R., Hyndman, D. W., Cunningham, K. J., Kaluarachchi, J. J., Yeh, W. W.-G., van Genuchten, M. T., & Jensen, K. (2006). Impacts of the 2004 tsunami on groundwater resources in Sri Lanka. *Water Resources Research*, *42*(5). https://doi.org/https://doi.org/10.1029/2006WR004876

Inouchi, K., Kishi, Y., & Kakinuma, T. (1990). The motion of coastal groundwater in response to the tide. *Journal of Hydrology*, *115*(1–4), 165–191. https://doi.org/10.1016/0022-1694(90)90203-A

IPCC. (2019). *Climate Change and Land: an IPCC special report on climate change, desertification, land degradation, sustainable land management, food security, and greenhouse gas fluxes in terrestrial ecosystems* (P. R. Shukla, J. Skea, C. Buendia, V. Masson-Delmotte, H.-O. Portner, D. C. Roberts, P. Zhai, R. Slade, S. Connors, R. van Diemen, M. Ferrat, E. Haughey, S. Luz, S. Neogi, M. Pathak, J. Petzold, J. Portugal Pereira, P. Vyas, E. Huntley, … J. Malley, Eds.).

Irvine, D. J., Briggs, M. A., Lautz, L. K., Gordon, R. P., McKenzie, J. M., & Cartwright, I. (2017). Using diurnal temperature signals to infer vertical groundwater-surface water exchange. *Groundwater*, *55*(1), 10–26. https://doi.org/10.1111/gwat.12459

Jacob, C. E. (1950). Flow of groundwater. *Engineering Hydraulics*, 321–386. https://doi.org/https://cir.nii.ac.jp/crid/1570572699755691264

James, T. S., Robin, C., Henton, J. A., & Craymer, M. (2021). *Relative sea-level projections for Canada based on the IPCC Fifth Assessment Report and the NAD83v70VG national crustal velocity model.* https://geoscan.nrcan.gc.ca/starweb/geoscan/servlet.starweb?path=geoscan/fulle.web&search1=R=327878

Jiao, J., & Post, V. (2019). *Coastal Hydrogeology*. Cambridge University Press. https://doi.org/10.1017/9781139344142

Kabat, P., van Vierssen, W., Veraart, J., Vellinga, P., & Aerts, J. (2005). Climate proofing the Netherlands. *Nature*, *438*, 283–284.

Kamphuis, J. W. (2010). Introduction to Coastal Engineering and Management. In *Advanced Series on Ocean Engineering: Vol. Volume 30*. WORLD SCIENTIFIC. https://doi.org/doi:10.1142/7021

Kang, L., Ma, L., & Liu, Y. (2016). Evaluation of farmland losses from sea level rise and storm surges in the Pearl River Delta region under global climate change. *Journal of Geographical Sciences*, *26*(4), 439–456. https://doi.org/10.1007/s11442-016-1278-z

Kennedy, G. W., & Drage., J. (2008). Groundwater regions of Nova Scotia, *Department of Natural Resources and Renewables, open file map ME 2008-3.* https://novascotia.ca/natr/meb/download/dp428.asp

Ketabchi, H., Mahmoodzadeh, D., Ataie-Ashtiani, B., & Simmons, C. T. (2016). Sea-level rise impacts on seawater intrusion in coastal aquifers: Review and integration. *Journal of Hydrology*, *535*, 235–255. https://doi.org/10.1016/j.jhydrol.2016.01.083

Kuan, W. K., Jin, G., Xin, P., Robinson, C., Gibbes, B., & Li, L. (2012). Tidal influence on seawater intrusion in unconfined coastal aquifers. *Water Resources Research*, *48*(2), 1–11. https://doi.org/10.1029/2011WR010678

Kurylyk, B. L., & MacQuarrie, K. T. B. (2013). The uncertainty associated with estimating future groundwater recharge: A summary of recent research and an example from a small unconfined aquifer in a northern humid-continental climate. *Journal of Hydrology*, *492*, 244–253. https://doi.org/https://doi.org/10.1016/j.jhydrol.2013.03.043

Lemmen, D. S., Warren, F. J., James, T. S., & Mercer Clarke, C. S. L. editors. (2016). *Canada's Marine Coasts in a Changing Climate*. https://www.nrcan.gc.ca/sites/www.nrcan.gc.ca/files/earthsciences/files/pdf/NRCAN _fullBook accessible.pdf

LeRoux, N. K., Kurylyk, B. L., Briggs, M. A., Irvine, D. J., Tamborski, J. J., & Bense, V. F. (2021). Using heat to trace vertical water fluxes in sediment experiencing concurrent tidal pumping and groundwater discharge. *Water Resources Research*, *57*(2), 1–13. https://doi.org/10.1029/2020WR027904

Levanon, E., Yechieli, Y., Gvirtzman, H., & Shalev, E. (2017). Tide-induced fluctuations of salinity and groundwater level in unconfined aquifers – Field measurements and numerical model. *Journal of Hydrology*, *551*, 665–675. https://doi.org/10.1016/j.jhydrol.2016.12.045

Li, H., & Jiao, J. (2001). Tide-induced groundwater fluctuation in a coastal leaky confined aquifer system extending under the sea. *Water Resources Research*, *37*(5), 1165–1171. https://doi.org/https://doi.org/10.1029/2000WR900296

Llopis-albert, C., & Pulido-velazquez, D. (2014). Discussion about the validity of sharp-interface models to deal with seawater intrusion in coastal aquifers. *Hydrological Processes*, *28*, 3642–3654. https://doi.org/10.1002/hyp.9908

Lombardi, P. (2014). *Sea level rise in Halifax Harbour: A statistical analysis. Undergraduate student research report.* 20–25.

Lopez-Martinez, M. (2022). *Data shows Fiona's impact across Atlantic Canada as all-time records broken*. CTV News. https://www.ctvnews.ca/climate-and-environment/data-shows-fiona-s-impact-across-atlantic-canada-as-all-time-records-broken-1.6084819

Lu, C., Xin, P., Li, L., & Luo, J. (2015). Seawater intrusion in response to sea-level rise in a coastal aquifer with a general-head inland boundary. *Journal of Hydrology*, *522*, 135–140. https://doi.org/10.1016/j.jhydrol.2014.12.053

Luisetti, T., Turner, R. K., Bateman, I. J., Morse-Jones, S., Adams, C., & Fonseca, L. (2011). Coastal and marine ecosystem services valuation for policy and management: Managed realignment case studies in England. *Ocean and Coastal Management*, *54*(3), 212–224. https://doi.org/10.1016/j.ocecoaman.2010.11.003

Manson, G. K., Couture, N. J., & James, T. S. (2019). CanCoast 2.0: data and indices to describe the sensitivity of Canada's marine coasts to changing climate. *Geological Survey of Canada, Open File*, *8551*(1).

McLaughlin, C., Law, B., & Mulligan, R. (2022). Modeling surface waves and tide–surge interactions leading to enhanced total water levels in a macrotidal bay. *Coastal Engineering Journal*, *64*(1), 24–41. https://doi.org/10.1080/21664250.2021.1965417

Mercer, J., Kurvits, T., Kelman, I., & Mavrogenis, S. (2014). Ecosystem-based adaptation for food security in the AIMS SIDS: Integrating external and local knowledge. *Sustainability (Switzerland)*, *6*(9), 5566–5597. https://doi.org/10.3390/su6095566

Michael, H. A., Post, V. E. A., Wilson, A., & Werner, A. D. (2017). Science, society, and the coastal groundwater squeeze. *Water Resources Research*, *53*(April), 2610–2617. https://doi.org/10.1016/j.jhydrol.2021.126281

Morgan, L. K., Bakker, M., & Werner, A. D. (2015). Occurrence of seawater intrusion overshoot. *Water Resources Research*, *51*(4), 1989–1999. https://doi.org/https://doi.org/10.1002/2014WR016329

Munk, W. H. (1950). Origin and generation of waves. *Coastal Engineering Proceedings*, *1*(1), 1. https://doi.org/10.9753/icce.v1.1

Neubauer, S. C. (2013). Ecosystem responses of a tidal freshwater marsh experiencing saltwater intrusion and altered hydrology. *Estuaries and Coasts*, *36*(3), 491–507. https://doi.org/10.1007/s12237-011-9455-x

Nicholls, R. J., Lincke, D., Hinkel, J., Brown, S., Vafeidis, A. T., Meyssignac, B., Hanson, S. E., Merkens, J. L., & Fang, J. (2021). A global analysis of subsidence, relative sea-level change and coastal flood exposure. *Nature Climate Change*. https://doi.org/10.1038/s41558-021-00993-z

Nielsen, P. (1990). Tidal dynamics of the water table in beaches. *Water Resources Research*, *26*(9), 2127–2134. https://doi.org/10.1029/WR026i009p02127

NRCAN. (2017). *Constructions and land use in Canada - CanVec Series - Manmade Features*. Natural Resources Canada. https://open.canada.ca/data/en/dataset/fd4369a4-21fe-4070-914a-067474da0fd6

ONSET. (2021). *HOBO RX3000 Remote monitoring station data logger manual*. https://www.onsetcomp.com/products/data-loggers/rx3000/

Paldor, A., & Michael, H. A. (2021). Storm surges cause simultaneous salinization and freshening of coastal aquifers, exacerbated by climate change. *Water Resources Research*. https://doi.org/10.1029/2020WR029213

Park, C.-H., & Aral, M. M. (2008). Saltwater intrusion hydrodynamics in a tidal aquifer. *Journal of Hydrologic Engineering*, *13*(9), 863–872. https://doi.org/10.1061/(asce)1084-0699(2008)13:9(863)

Pavlovskii, I., Cantelon, J. A., & Kurylyk, B. L. (2022). Coastal groundwater model calibration using filtered and amplified hydraulic information retained in the freshwater–saltwater interface. *Hydrogeology Journal*, *30*(5), 1551–1567. https://doi.org/10.1007/s10040-022-02510-8

Pawlowicz, R., Beardsley, B., & Lentz, S. (2002). Classical tidal harmonic analysis including error estimates in MATLAB using TDE. *Computers and Geosciences*, *28*(8), 929–937. https://doi.org/10.1016/S0098-3004(02)00013-4

Penman, H. L. (1948). Natural evaporation from open water, bare soil and grass. *Proceedings of the Royal Society of London. Series A. Mathematical and Physical Sciences*, *193*(1032), 120–145. https://doi.org/https://doi.org/10.1098/rspa.1948.0037

Percy, J. A. (1996). Dykes, dams, and dynamos: the impacts of coastal structures. Fundy Issues 9. Bay of Fundy Ecosystem Partnership. *Fundy Issues*.

Pitman, M. G., & Läuchli, A. (2002). Global impact of salinity and agricultural ecosystems. In A. Läuchli & U. Lüttge (Eds.), *Salinity: Environment - Plants - Molecules* (pp. 3–20). Springer Netherlands. https://doi.org/10.1007/0-306-48155-3_1

Pool, M., Post, V. E. A., & Simmons, C. T. (2014). Effects of tidal fluctuations on mixing and spreading in coastal aquifers: homogeneous case. *Water Resources Research*, 6910–6926. https://doi.org/10.1002/2014WR015534.Received

Post, V. E. A., & Houben, G. J. (2017). Density-driven vertical transport of saltwater through the freshwater lens on the island of Baltrum (Germany) following the 1962 storm flood. *Journal of Hydrology*, *551*, 689–702. https://doi.org/10.1016/J.JHYDROL.2017.02.007

Preston, M. S., & Raudsepp-Hearne, C. (2017). *Completing and Using Ecosystem Service Assessment for Decision-Making: An Interdisciplinary Toolkit for Managers and Analysts*. Ottawa, ON: Federal, Provincial, and Territorial Governments of Canada.

Raghukumar, K., Chang, G., Spada, F., Jones, C., Janssen, T., & Gans, A. (2019). Performance characteristics of "spotter,"' a newly developed real-time wave measurement buoy. *Journal of Atmospheric and Oceanic Technology*, *36*(6), 1127–1141. https://doi.org/10.1175/JTECH-D-18-0151.1

Ramkumar, M., Menier, D., & Kumaraswamy, K. (2019). Coastal zone management during changing climate and rising sea level: transcendence of institutional, geographic, and subject field barriers is the key. *Coastal Zone Management: Global Perspectives, Regional Processes, Local Issues*, 1–12. https://doi.org/10.1016/B978-0-12-814350-6.00001-X

Reilly, T. E., & Goodman, A. S. (1987). Analysis of saltwater upconing beneath a pumping well. *Journal of Hydrology*, *89*(3–4), 169–204. https://doi.org/10.1016/0022-1694(87)90179-X

Reilly, T. E., & Harbaugh, A. W. (2004). Guidelines for Evaluating Ground-Water Flow Models: Scientific Investigations Report 2004-5038. In *USGS: Scientific Investigations Report 2004-5038*.

Rivard., C., Deblonde., C., Boivin., R., Paradis., S. J., Paradis., D., Liao., S., Gauthier., M.-J., Blackmore., A., Drage., J., & Michaud., Y. (2006). *Canadian groundwater inventory: Hydrogeological atlas of the Annapolis Valley, Nova Scotia*. Geological Survey of Canada Open File Report 5541.

Rivard, C., Paradis, D., Paradis, S. J., Bolduc, A., Morin, R. H., Liao, S., Pullan, S., Gauthier, M., Trépanier, S., Blackmore, A., Spooner, I., Deblonde, C., Boivin, R., Fernandes, R. A., Castonguay, S., Hamblin, T., Michaud, Y., Drage, J., & Paniconi, C. (2012). *Geological Survey of Canada Canadian Groundwater Inventory: regional hydrogeological characterization of the Annapolis Valley aquifer*. Geological Survey of Canada Bulletin 598. http://publications.gc.ca/collections/collection_2012/rncan-nrcan/M42-598-eng.pdf

Robinson, C. E., Xin, P., Santos, I. R., Charette, M. A., Li, L., & Barry, D. A. (2018). Groundwater dynamics in subterranean estuaries of coastal unconfined aquifers: Controls on submarine groundwater discharge and chemical inputs to the ocean. *Advances in Water Resources*. https://doi.org/10.1016/j.advwatres.2017.10.041

Robinson, C., & Li, L. (2004). Effect of tidal oscillations on water exchange and mixing in a coastal aquifer. In *Developments in Water Science* (Vol. 55, Issue PART 2, pp. 1583–1594). Elsevier. https://doi.org/10.1016/S0167-5648(04)80168-0

Robinson, C., Li, L., & Barry, D. A. (2007). Effect of tidal forcing on a subterranean estuary. *Advances in Water Resources*, *30*(4), 851–865. https://doi.org/10.1016/J.ADVWATRES.2006.07.006

Rotzoll, K., & Fletcher, C. H. (2013). Assessment of groundwater inundation as a consequence of sea-level rise. *Nature Climate Change*, *3*(5), 477–481. https://doi.org/10.1038/nclimate1725

Santos, I. R., Eyre, B. D., & Huettel, M. (2012). The driving forces of porewater and groundwater flow in permeable coastal sediments: A review. *Estuarine, Coastal and Shelf Science*, *98*, 1–15. https://doi.org/10.1016/J.ECSS.2011.10.024

Sawyer, A. H., Michael, H. A., & Schroth, A. W. (2016). From soil to sea: the role of groundwater in coastal critical zone processes. *Wiley Interdisciplinary Reviews: Water*, *3*(5), 706–726. https://doi.org/10.1002/wat2.1157

Schieder, N. W., Walters, D. C., & Kirwan, M. L. (2018). Massive upland to wetland conversion compensated for historical marsh loss in Chesapeake Bay, USA. *Estuaries and Coasts*, *41*(4), 940–951. https://doi.org/10.1007/s12237-017-0336-9

Schmork, S., & Mercado, A. (1969). Upconing of fresh water - sea water interface below pumping wells, field study. *Water Resources Research*, *5*(6), 1290–1311. https://doi.org/https://doi.org/10.1029/WR005i006p01290

Shaw. (2011). *Shaw Backpack drill*. https://backpackdrill.com/

Sherren, K., Bowron, T., Graham, J., Rahman, H. M. T., & van Proosdij, D. (2019). Coastal infrastructure realignment and salt marsh restoration in Nova Scotia, Canada. *Responding to Rising Seas: OECD Country Approaches to Tackling Coastal Risks*, 111–135. https://www.researchgate.net/profile/Kate-Sherren/publication/331558602_Coastal_infrastructure_realignment_and_salt_marsh_restoration_in_Nova_Scotia_Canada/links/5c801be692851c69505c613e/Coastal-infrastructure-realignment-and-salt-marsh-restoration-in-Nov

Sherren, K., Ellis, K., Guimond, J., Kurylyk, B., LeRoux, N., Lundholm, J., Mallory, M., van Proosdij, D., Walker, A., Bowron, T., Brazner, T., Kellman, L., Turner, B., & Wells, E. (2021). Understanding multifunctional Bay of Fundy dykelands and tidal wetlands using ecosystem services - a baseline. *FACETS*, *6*(1), 1446–1473. https://doi.org/https://doi.org/10.1139/facets-2020-0073

Sherren, K., Loik, L., & Debner, J. A. (2016). Climate adaptation in "new world" cultural landscapes: The case of Bay of Fundy agricultural dykelands (Nova Scotia, Canada). *Land Use Policy*, *51*, 267–280. https://doi.org/10.1016/j.landusepol.2015.11.018

Singh, K., Walters, B. B., & Ollerhead, J. (2007). Climate change, sea-level rise and the case for salt marsh restoration in the Bay of Fundy, Canada. *Environments*, *35*(2), 71–84.

Singha, K., Johnson, T., Day-Lewis, F., & Slater, L. (2022). *Electrical Imaging for Hydrogeology*. Pacific Northwest National Lab.

Skaggs, R. W., & van Schilfgaarde, J. (1999). Agricultural drainage. In R. W. Skaggs & J. van Schilfgaarde (Eds.), *Agronomy Monograph 38*. American Society of Agronomy Madison, Wisconsin, USA. https://doi.org/10.2134/agronmonogr38

Slooten, L. J., Carrera, J., Castro, E., & Fernandez-Garcia, D. (2010). A sensitivity analysis of tide-induced head fluctuations in coastal aquifers. *Journal of Hydrology*, *393*(3–4), 370–380. https://doi.org/10.1016/J.JHYDROL.2010.08.032

Solinst. (2020). *Levelogger 5 LTC: Level: Temperature: Conductivity Datalogger*. https://www.solinst.com/products/dataloggers-and-telemetry/3001-levelogger-series/levelogger/datasheet/

Stark, J., Van Oyen, T., Meire, P., & Temmerman, S. (2015). Observations of tidal and storm surge attenuation in a large tidal marsh. *Limnology and Oceanography*, *60*(4), 1371–1381. https://doi.org/10.1002/lno.10104

Stark, N., & Hay, A. E. (2014). Pore water infiltration and drainage on a megatidal beach in relation to tide- and wave-forcing. *Sediment Transport and Morphology*, *1*(34). https://doi.org/https://doi.org/10.9753/icce.v34.sediment.25

Stea, R., Conley, H., & Brown, Y. (1992). *Surficial geology map of the province of Nova Scotia*. https://novascotia.ca/natr/meb/download/dp036.asp

Stockdon, H. F., Holman, R. A., Howd, P. A., & Sallenger, A. H. (2006). Empirical parameterization of setup, swash, and runup. *Coastal Engineering*, *53*(7), 573–588. https://doi.org/10.1016/j.coastaleng.2005.12.005

Storlazzi, C. D., Gingerich, S. B., van Dongeren, A., Cheriton, O. M., Swarzenski, P. W., Quataert, E., Voss, C. I., Field, D. W., Annamalai, H., Piniak, G. A., & McCall, R. (2018). Most atolls will be uninhabitable by the mid-21st century because of sea-level rise exacerbating wave-driven flooding. *Science Advances*, *4*(4), 1–10. https://doi.org/10.1126/sciadv.aap9741

Tebaldi, C., Strauss, B. H., & Zervas, C. E. (2012). Modelling sea level rise impacts on storm surges along US coasts. *Environmental Research Letters*, *7*(1). https://doi.org/10.1088/1748-9326/7/1/014032

Temmerman, S., Meire, P., Bouma, T. J., Herman, P. M. J., Ysebaert, T., & De Vriend, H. J. (2013). Ecosystem-based coastal defence in the face of global change. *Nature*, *504*(7478), 79–83. https://doi.org/10.1038/nature12859

Teo, H. T., Jeng, D. S., Seymour, B. R., Barry, D. A., & Li, L. (2003). A new analytical solution for water table fluctuations in coastal aquifers with sloping beaches. *Advances in Water Resources*, *26*(12), 1239–1247. https://doi.org/10.1016/j.advwatres.2003.08.004

Therrien, R., & Sudicky, E. A. (1996). Three-dimensional analysis of variably-saturated flow and solute transport in discretely-fractured porous media. *Journal of Contaminant Hydrology*, *23*(1–2), 1–44. https://doi.org/10.1016/0169-7722(95)00088-7

Threndyle, R. E., Kurylyk, B. L., Huang, Y., Johnston, L. H., & Jamieson, R. C. (2022). CrAssphage as an indicator of groundwater-borne pollution in coastal ecosystems. *Environmental Research Communications*, *4*(5). https://doi.org/10.1088/2515-7620/ac693a

Trescott, P. (1968). *Groundwater Resources and Hydrogeology of the Annapolis-Cornwallis Valley, Nova Scotia.* Nova Scotia Department of Mines, Groundwater Section Memoir 6.
https://novascotia.ca/nse/groundwater/docs/GroundwaterResourceReport_Annapolis-CornwallisValley.pdf

Trescott, P. (1969a). *Groundwater Resources and Hydrogeology of the Western Annapolis Valley,* Nova Scotia. Nova Scotia Department of Mines, Groundwater Section Report 69-1.
https://novascotia.ca/nse/groundwater/docs/GroundwaterResourceReport_WesternAnnapolisValley.pdf

Trescott, P. (1969b). *Hydrogeology of Sharpe Brook IHD Watershed, Kings County, Nova Scotia*. Nova Scotia Department of Mines, Groundwater Section Report.
https://novascotia.ca/nse/groundwater/docs/GroundwaterResourceReport_Kings3.pdf

Tully, K., Gedan, K., Epanchin-Niell, R., Strong, A., Bernhardt, E. S., Bendor, T., Mitchell, M., Kominoski, J., Jordan, T. E., Neubauer, S. C., & Weston, N. B. (2019). The invisible flood: The chemistry, ecology, and social implications of coastal saltwater intrusion. *BioScience*, *69*(5), 368–378.
https://doi.org/10.1093/biosci/biz027

van der Kamp, G. (1972). Tidal fluctuations in a confined aquifer extending under the sea. *International Geological Congress*, *24*(11), 101–106. https://pascal-francis.inist.fr/vibad/index.php?action=getRecordDetail&idt=PASCALGEODEBRGM732261661

van Genuchten, M. Th. (1980). A Closed-form Equation for Predicting the Hydraulic Conductivity of Unsaturated Soils. *Soil Science Society of America Journal*, *44*(5), 892–898. https://doi.org/10.2136/sssaj1980.03615995004400050002x

van Proosdij, D., Bowron, T., & Neatt, N. (2014). Development and application of guidelines for managed realignment to maximize adaptive capacity and ecosystem services. *Maritime Provinces Spatial Analysis Research Centre, Saint Mary's University*.

van Proosdij, D., Lundholm, J., Neatt, N., Bowron, T., & Graham, J. (2010). Ecological re-engineering of a freshwater impoundment for salt marsh restoration in a hypertidal system. *Ecological Engineering*, *36*(10), 1314–1332.
https://doi.org/10.1016/j.ecoleng.2010.06.008

van Proosdij, D., & Page, S. (2015). *Best management practices for climate change adaptation in dykelands: recommendations for Fundy ACAS sites*. Atlantic Climate Adaptation Solutions Association. https://doi.org/10.13140/2.1.3113.0405

Vandenbohede, A., & Lebbe, L. (2007). Effects of tides on a sloping shore: Groundwater dynamics and propagation of the tidal wave. *Hydrogeology Journal*, *15*(4), 645–658. https://doi.org/10.1007/s10040-006-0128-y

Vithanage, M., Engesgaard, P., Jensen, K. H., Illangasekare, T. H., & Obeysekera, J. (2012). Laboratory investigations of the effects of geologic heterogeneity on groundwater salinization and flush-out times from a tsunami-like event. *Journal of Contaminant Hydrology*, *136–137*, 10–24. https://doi.org/https://doi.org/10.1016/j.jconhyd.2012.05.001

Watson, T. A., Werner, A. D., & Simmons, C. T. (2010). Transience of seawater intrusion in response to sea level rise. *WRR*, *46*(September), 1–10. https://doi.org/10.1029/2010WR009564

Webster, T., McGuigan, K., & MacDonald, C. (2012). *Map of coastal flood risk from sea-level rise and storm surge of the Wolfville area, Kings County, Nova Scotia; Nova Scotia Department of Natural Resources, Mineral Resources Branch, Open File Map ME 2012-051, scale 1:10 000*.

Werner, A. D., Bakker, M., Post, V. E. A., Vandenbohede, A., Lu, C., Ataie-Ashtiani, B., Simmons, C. T., & Barry, D. A. (2013). Seawater intrusion processes, investigation and management: Recent advances and future challenges. *Advances in Water Resources*, *51*, 3–26. https://doi.org/10.1016/j.advwatres.2012.03.004

Werner, A. D., & Simmons, C. T. (2009). Impact of sea-level rise on sea water intrusion in coastal aquifers. *Groundwater*, *47*(2), 197–204. https://doi.org/10.1111/j.1745-6584.2008.00535.x

Werner, A. D., Ward, J. D., Morgan, L. K., Simmons, C. T., Robinson, N. I., & Teubner, M. D. (2012). Vulnerability indicators of sea water intrusion. *Groundwater*, *50*(1), 48–58. https://doi.org/10.1111/j.1745-6584.2011.00817.x

White, E., & Kaplan, D. (2017). Restore or retreat? Saltwater intrusion and water management in coastal wetlands. *Ecosystem Health and Sustainability*, *3*(1), 1–18. https://doi.org/10.1002/ehs2.1258

Wilson, E. (2016). *An assessment of coastal erosion in the Minas Basin, Nova Scotia* [Dalhousie University]. https://dalspace.library.dal.ca/bitstream/handle/10222/72036/Wilson-Erin-MSc-OCEA-July-2016.pdf?sequence=3

Xiao, H., Wang, D., Medeiros, S. C., Bilskie, M. v, Hagen, S. C., & Hall, C. R. (2019). Exploration of the effects of storm surge on the extent of saltwater intrusion into the surficial aquifer in coastal east-central Florida (USA). *Science of The Total Environment*, *648*, 1002–1017. https://doi.org/https://doi.org/10.1016/j.scitotenv.2018.08.199

Xu, C. Y., & Singh, V. P. (2002). Cross comparison of empirical equations for calculating potential evapotranspiration with data from Switzerland. *Water Resources Management*, *16*(3), 197–219. https://doi.org/10.1023/A:1020282515975

Yang, J., Graf, T., Herold, M., & Ptak, T. (2013). Modelling the effects of tides and storm surges on coastal aquifers using a coupled surface-subsurface approach. *Journal of Contaminant Hydrology*, *149*, 61–75. https://doi.org/10.1016/j.jconhyd.2013.03.002

Yang, J., Graf, T., & Ptak, T. (2015). Impact of climate change on freshwater resources in a heterogeneous coastal aquifer of Bremerhaven, Germany: A three-dimensional modeling study. *Journal of Contaminant Hydrology*, *177–178*, 107–121. https://doi.org/10.1016/j.jconhyd.2015.03.014

Yang, J., Zhang, H., Yu, X., Graf, T., & Michael, H. A. (2018). Impact of hydrogeological factors on groundwater salinization due to ocean-surge inundation. *Advances in Water Resources*, *111*(November 2017), 423–434. https://doi.org/10.1016/j.advwatres.2017.11.017

Yang, Z., Khangaonkar, T., Calvi, M., & Nelson, K. (2010). Simulation of cumulative effects of nearshore restoration projects on estuarine hydrodynamics. *Ecological Modelling*, *221*(7), 969–977. https://doi.org/10.1016/j.ecolmodel.2008.12.006
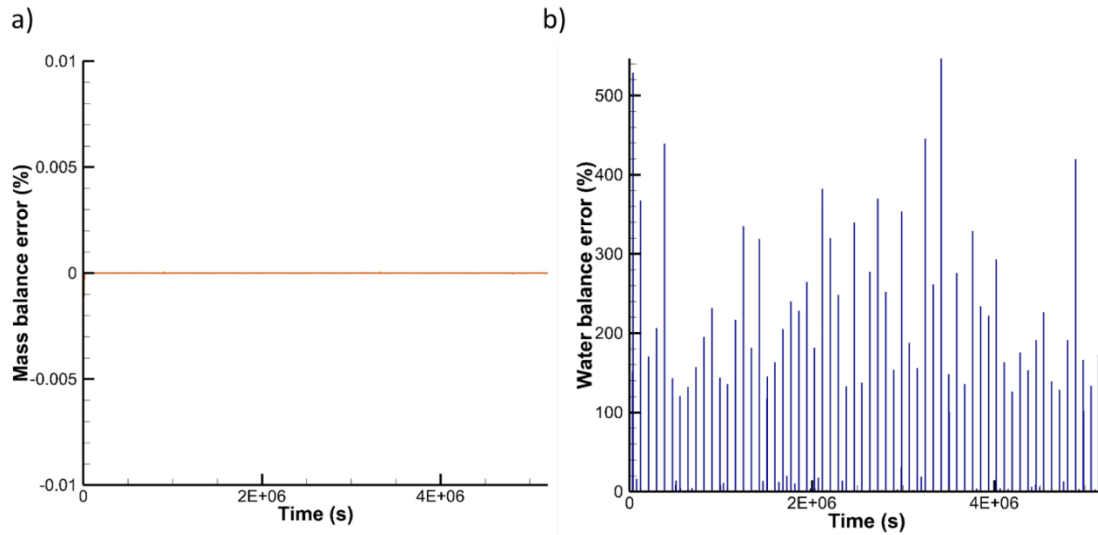
APPENDIX

Figure A1. HGS model outputs for a) mass balance errors and b) water balance errors. As advection (which would be impacted by water balance errors) leads to solute transport, the absence of errors for the mass (solute) balance and the concurrent pronounced errors in the water balance are likely indicative of an issue in water balance error calculations in the HydroGeoSphere code when density-driven flow is activated. Similar issues have been noted by other coastal hydrogeology researchers in email communications.
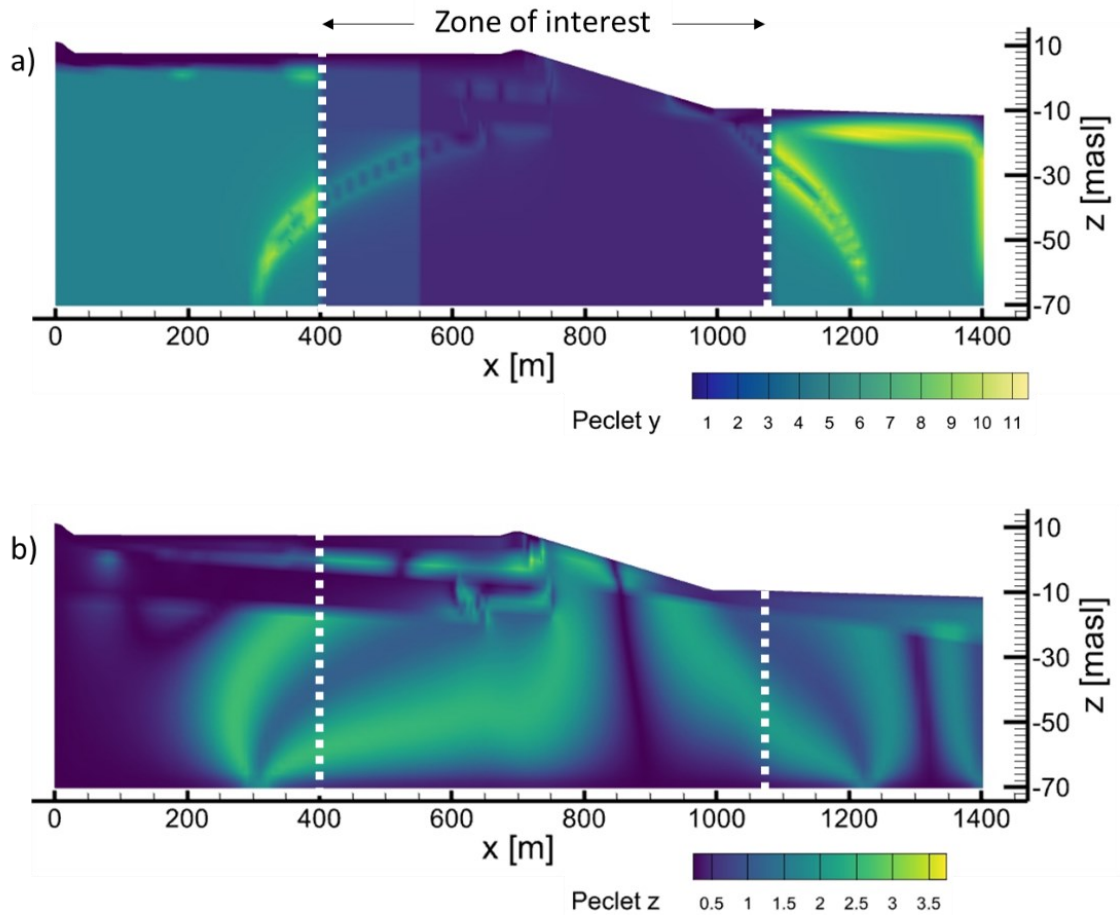
Figure A2. HGS model output for a) Peclet number in the x direction and b) Peclet number in the z direction. Results are from the 2100 RCP 8.5 SLR scenario (see Figure 22).
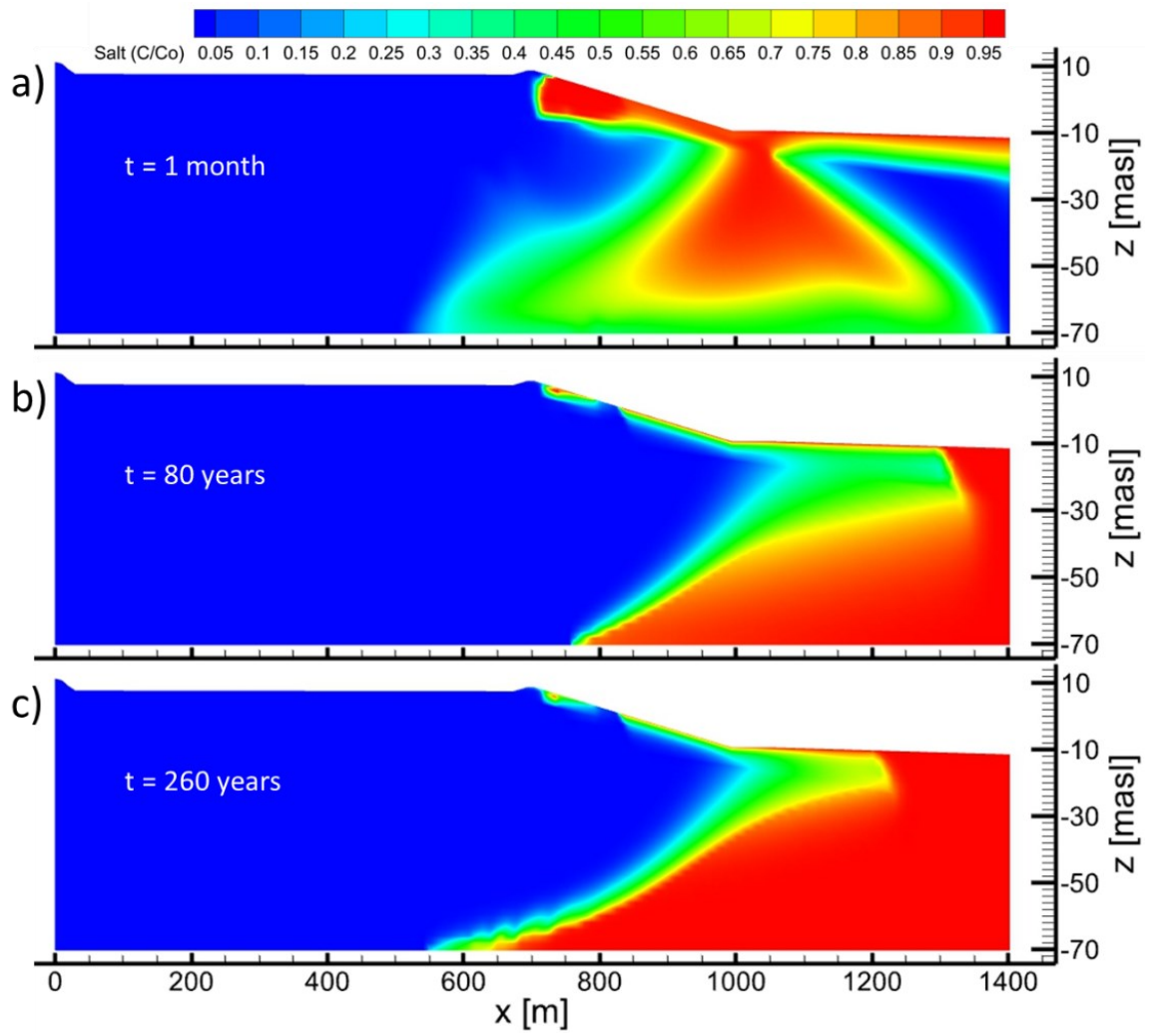
Figure A3. Post-SLR4 results without tides. a) 1-month post-SLR, b) 80 years post-SLR, and c) 260 years post-SLR. See link for video: SLR4_scenario_260yr.
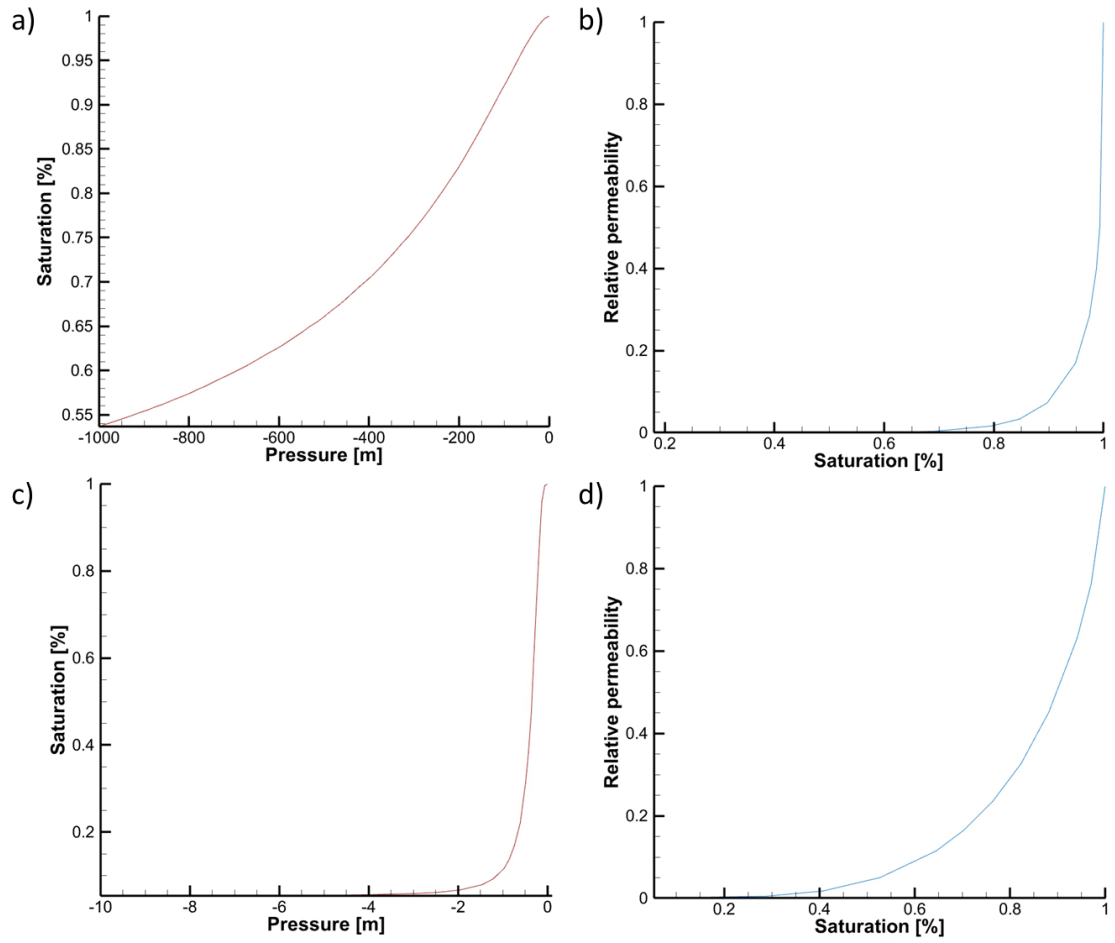
Figure A4. HGS model outputs for pressure-saturation curves (a and c) and relative permeability-saturation curves (b and d). Panels a) and b) are from the original van Genuchten (1980) parameter selection, and panels c) and d) are from the default HGS van Genuchten (1980) parameter selection.
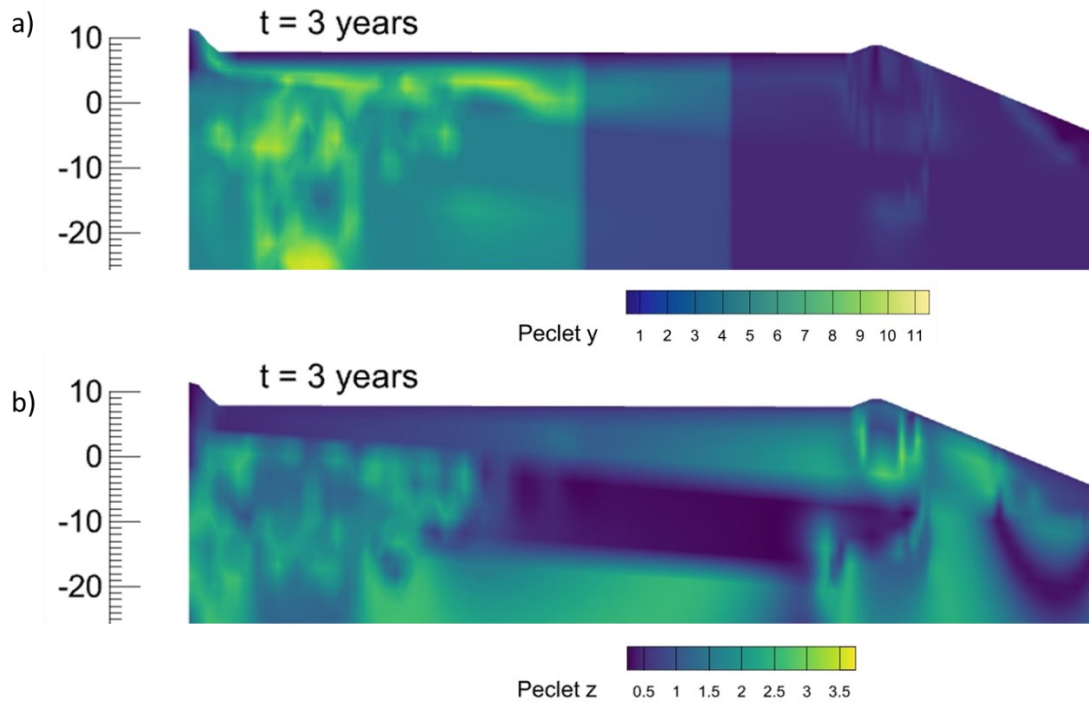
Figure A5. HGS model output for a) Peclet number in the x direction and b) Peclet number in the z direction. Results are from the 2100 surge simulation (three-years post-surge, see Figure 24).